INFORMATION TO USERS

This manuscript has been reproduced from the microfilm master. UMI films the text directly from the original or copy submitted. Thus, some thesis and dissertation copies are in typewriter face, while others may be from any type of computer printer.

The quality of this reproduction is dependent upon the quality of the copy submitted. Broken or indistinct print, colored or poor quality illustrations and photographs, print bleedthrough, substandard margins, and improper alignment can adversely affect reproduction.

In the unlikely event that the author did not send UMI a complete manuscript and there are missing pages, these will be noted. Also, if unauthorized copyright material had to be removed, a note will indicate the deletion.

Oversize materials (e.g., maps, drawings, charts) are reproduced by sectioning the original, beginning at the upper left-hand corner and continuing from left to right in equal sections with small overlaps. Each original is also photographed in one exposure and is included in reduced form at the back of the book.

Photographs included in the original manuscript have been reproduced xerographically in this copy. Higher quality 6" x 9" black and white photographic prints are available for any photographs or illustrations appearing in this copy for an additional charge. Contact UMI directly to order.

UMI

A Bell & Howell Information Company
300 North Zeeb Road, Ann Arbor MI 48106-1346 USA
313/761-4700 800/521-0600

AXISYMMETRIC MICROFRACTURE ANALYSIS OF FIBER-REINFORCED BRITTLE COMPOSITES

by

Hanqing Zhang

A dissertation submitted to the Graduate Faculty in Engineering
in partial fulfillment of the requirements for the degree of
Doctor of Philosophy, The City University of New York

1997

This manuscript has been read and accepted for the Graduate Faculty in Engineering in satisfaction of the dissertation requirement for the degree of Doctor of Philosophy.

8/7/97
Date

Dr. Benjamin B. M. Liaw
Chair of Examining Committee

8/11/97
Date

Dr. Gerard G. Lowen
Executive Officer

Prof. Benjamin B. M. Liaw (Mentor)

Prof. Feridun Delale (Co-Mentor)

Prof. Ali M. Sadegh

Prof. Mumtaz K. Kassir

Dr. Erwin Liang, GE Corporate R & D
Supervisory Committee

THE CITY UNIVERSITY OF NEW YORK

Abstract

Axisymmetric Microfracture Analysis of Fiber-Reinforced Brittle Composites

by

Hanqing Zhang

Adviser: Professor Benjamin B. M. Liaw

The mechanical behavior of ceramic-matrix composites (CMCs) depends mainly on the initiation and development of microdamage within the composites. In this study a three-cylinder model was developed to analyze the initiation of microdamage and its progression in CMCs. To verify the usefulness of this model, it was then used to simulate the damage progression in a ceramic matrix composite and to predict its tensile behavior. In the model, combination of the inner fiber and matrix cylinders represents a typical unit of the composite, while the outer composite medium models the rest of the material. The damage modes considered were multiple-matrix cracking, fiber-matrix interfacial debonding, and frictional interfacial sliding. The singular integral equation technique was used to formulate the problem. Effective numerical procedures were developed to solve the singular integral equations for accurate determination of the displacement and stress fields as well as the stress singularities. Complemented with the concepts of fracture mechanics and energy balance principle, the damage progression in a CMC, Nicalon/CAS II, under uniaxial tension was simulated. The predicted stress-strain curves

are in good agreement with available experiment data. The effects of three important micromechanical parameters: the matrix fracture energy, the interfacial debonding energy and the interfacial friction stress on the damage progression within the composite and its macromechanical behavior were also thoroughly investigated. The model has been proven to be successful in capturing the damage mechanisms in CMCs and simulating their development with minimum reliance on experimental data.

Acknowledgments

I would like to express my sincere gratitude and appreciation to my adviser, Professor Benjamin B. M. Liaw, for introducing me to the area of composite materials, skillfully directing me in all phases of this work, patiently correcting my manuscript, and friendly providing me with many personal helps. I would never have been able to accomplish this work without his continuous assistance, encouragement and trust.

I am very grateful to Professor Feridun Delale, my co-mentor, for his expert guidance and assistance during the course of this study. His advice and help on the singular integral equation technique are especially appreciated.

I would also like to thank Dean Gerard G. Lowen for many helps and all arrangements; and the members of my Doctoral Committee, Professor Mumtaz K. Kassir, Professor Ali M. Sadegh and Dr. Erwin Liang, for their interest, time, constructive comments and suggestions. Many enlightening discussions with Professor Mumtaz K. Kassir are especially helpful to this research and are gratefully acknowledged.

I am deeply grateful to Professor Peter Ganatos for his helps on numerical analysis, computer applications and my teaching in the department. I want to thank Dr. Andy S. Zhang for allowing me to use his SEM micrographs.

The Graduate Assistance Fellowship-B from the Department of Mechanical Engineering at CCNY and the fellowships from Graduate School and University Center of The City University of New York are gratefully acknowledged.

Contents

List of Tables and Figures

1 Introduction

1.1 Background

In recent years there has been an increasing demand for high temperature structural materials for use in aerospace and heat engine industries. Owing to their very appealing properties such as light-weight, corrosion resistance, superior performance at high temperature, brittle materials, such as ceramics, have drawn great attention for research. Their applications, however, are restricted due to their brittle nature (i.e. low fracture toughness), which makes them notch-sensitive and prone to catastrophic failure. Techniques to alleviate the problem of low fracture toughness while retaining the best properties of these materials have been the subject of intensive research. One of the most successful approaches to achieve this goal is by adding fibers to form composites. Composites made of glass-ceramic matrices reinforced with carbon fibers were some early examples [1-3]. More recently, with the availability of continuous SiC fibers, considerable attention has been focused on the development of ceramic-fiber-reinforced ceramic matrix composites (CMCs) [4-6], which offer great potential to achieve high performance at high temperatures.

Experimental tensile tests have shown that CMCs usually have higher strength and substantially lower notch sensitivity than their monolithic counterparts, and that after the initiation of matrix cracking they even exhibit certain quasi-ductile behavior [7-10]. Figure 1.1 shows a typical tensile stress-strain curve of a SiC-fiber/glass-ceramic-matrix composite Nicalon/CAS II. The significant non-linear behavior of the CMC implies

existence of certain energy-dissipation mechanisms. *In situ* microscopic examinations of the specimen surface during tests have revealed that such non-linear behavior of a CMC is closely related to the microdamage and its progression in the composite. The damage is in turn governed by the micromechanical properties of the composite, especially those associated with the fiber-matrix interface. Figures 1.2 to 1.4 are some of the *in situ* SEM micrographs of a Nicalon/CAS II specimen showing the initiation and progression of microdamage in the composite. In general, failure of a composite starts from matrix cracking as shown in Fig. 1.3(a), which is followed by several stages: progressive multiple matrix cracking as shown in Figs 1.3(b) to (d), interfacial debonding, fiber breaking, and fiber pullout as shown in Fig. 1.4, and finally the complete separation of the specimen into two or more pieces.

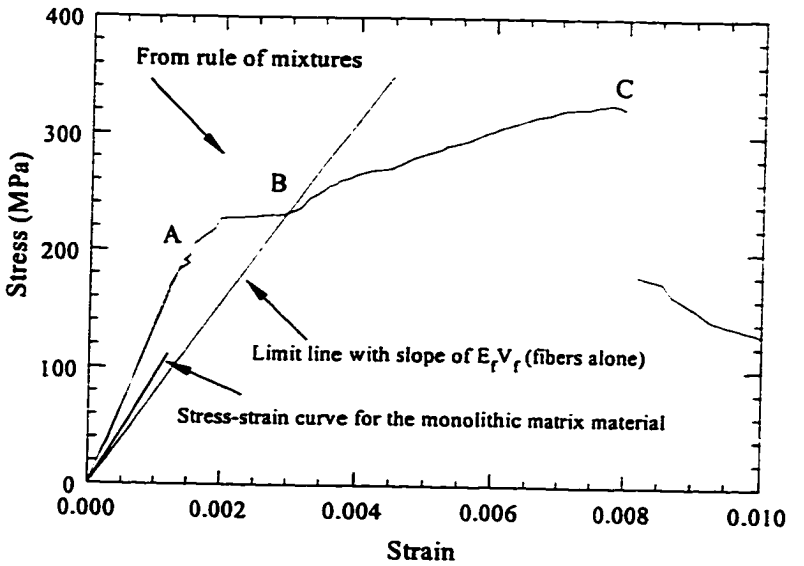

Fig. 1.1 A typical tensile stress-strain curve for a Nicalon/CAS II tested at room temperature ($V_f = 0.4$, $E_f = 195$ GPa, $E_m = 95$ GPa).

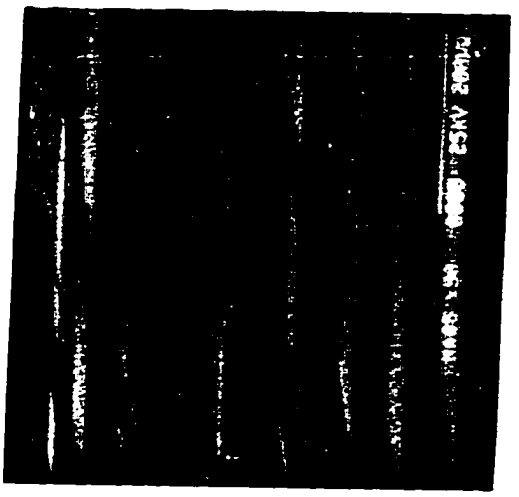

Figure 1.2 SEM micrograph of an undamaged unidirectional Nicalon/CAS II.

Unlike a monolithic ceramic, which is sensitive to cracks and usually fails catastrophically once a crack starts to propagate, a CMC not only has much higher matrix crack initiation strain (as indicated by Point A in Fig. 1.1), but can also undergo further loading after the formation of the first matrix crack. As shown in Fig. 1.1, the stress increases almost continuously from point A to point C. This favorable characteristic arises because (i) the reinforcement with stronger fibers may delay or even suppress minute matrix defects from becoming macrocracks; and (ii) the fiber-matrix interface, if strong enough for stress transfer yet sufficiently weak for interface debonding, may deflect or even arrest the propagation of matrix cracks. Depending upon the interfacial properties, a matrix crack propagating in a cross section perpendicular to fibers may either break the fibers or leave them intact. If the interface bonding is too strong, the matrix crack will extend into and cut through the fibers without inducing interfacial

debonding, thus resulting in a catastrophic failure similar to the failure mode of monolithic ceramics. Little, if any, performance enhancement can be expected in this

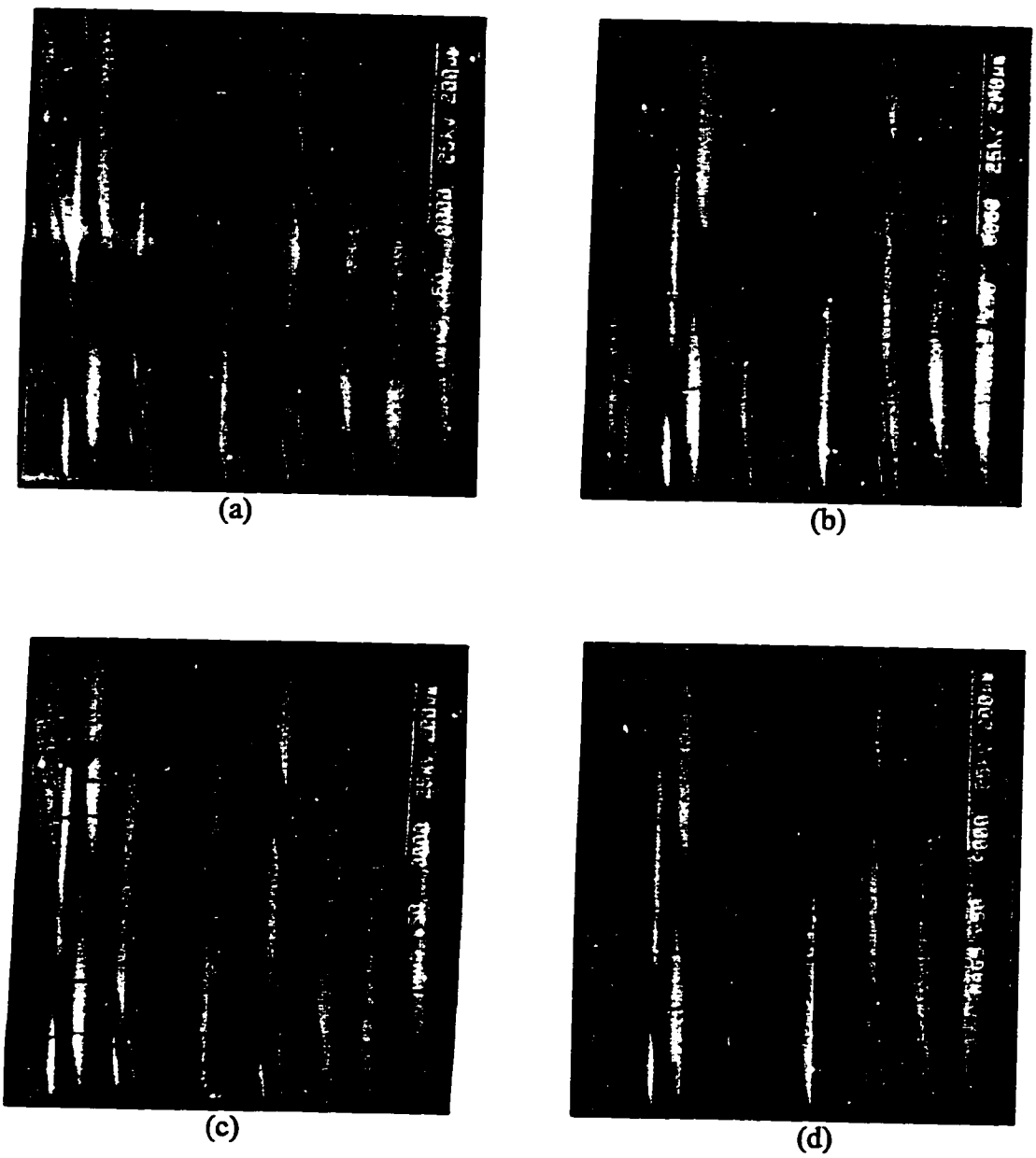

Figure 1.3 SEM micrographs showing progression of multiple matrix cracking.

form of composite failure. On the other hand, if the interfacial strength is weak enough to allow interfacial debonding, the matrix crack may either be arrested or deflected at debonded interfaces, or run around the fibers without fracturing them. Those fibers are therefore left intact to bridge the matrix crack surfaces. This damage mode, widely called *fiber-bridged matrix cracking*, has been deemed desirable for brittle matrix composites since the bridging fibers can supply closure traction at matrix crack surfaces to hold them from complete separation. Catastrophic failure, if not avoided eventually, can thus at least be delayed.

Figure 1.4 SEM micrograph showing fiber break and pull-out.

If fibers are strong enough, with increasing loading the matrix will continue to crack with reduced matrix crack spacing, as shown in Fig. 1.3, until the composite is saturated with matrix cracks which are spaced almost evenly in the fiber direction. This type of failure is termed *multiple matrix cracking*. During this process another type of damage, called *interfacial debonding*, may also develop. The actual damage mode will depend on the properties of the fiber, matrix and fiber-matrix interface. Following the completion of multiple matrix cracking, further *interfacial debonding, fiber breaking* and *fiber pull-out* are the dominant damage modes until the final failure of the specimen. As depicted in Fig. 1.4, these damage modes will increase the matrix crack opening displacement, and thus the tensile strain significantly. Since matrix cracking, interfacial debonding, interfacial frictional sliding, fiber breaking and pullout are all energy dissipating mechanisms, they are thus directly responsible for the quasi-ductile behavior of brittle matrix composites. Because all these mechanisms are governed directly or indirectly by the properties of the fiber-matrix interface, a thorough understanding of the role of fiber-matrix interface in the crack-induced damage process is necessary.

It has been well known that the fiber-matrix interfacial bond strength and the interfacial friction are two of the most important properties influencing the behavior of a composite. Therefore one need characterize these two properties first before making any attempt to correlate them to the tensile-induced damage behavior of the composite. Accurate characterization of these two parameters remains a hot research topic. If one considers the brittleness of both the fiber and the matrix and their similar chemical structures, the interfacial debonding process can be treated as a mode II fracture. On the other hand if one assumes the absence of chemical bond, interfacial failure can then be

viewed as a shear failure process. The interfacial frictional stress at debonded areas has usually been assumed either a constant (presumably due to asperities), or Coulomb friction.

The presence of fibers and randomly distributed microcracks makes rigorous mechanics analysis of the damage process very challenging. A number of analyses, such as those in [11-22], have been proposed for this purpose. Most of them are based on the shear lag model which, due to its inability to capture intense variation in stresses, usually considers the shear failure interface. In addition the shear lag model commonly neglects shear deformation in the fiber and tensile stress in the matrix. This approximation, however, is not reasonable for CMCs since the moduli of fibers and the matrix are of the same order. The main purpose of most early analyses [11-18] was only to predict the strains or stresses for matrix cracking initiation, i.e. Point A in Fig. 1.1. Although some recent analyses [19-22] have attempted to simulate tensile behaviors of CMCs, they still used shear failure to describe the interfacial debonding. The influence of fiber-matrix interfacial bonding on the behavior of CMCs has not been addressed thoroughly in these analyses. Since the interfacial debonding toughness and the frictional stress directly control interfacial debonding, and the interfacial debonding has major effects on matrix cracking and its progression, it is therefore desirable to develop new models which can describe the interface more accurately so that its influence on the behavior of the composite can be fully investigated.

1.2 Objectives

The objectives of this study were to theoretically model the damage modes experimentally observed in unidirectional ceramic matrix composites and to investigate the influence of micromechanical parameters on the damage modes and the macrobehavior of the composite. The study breaks down into three major tasks:

(1) To develop an advanced model to analyze the microdamage and its progression in unidirectional fiber-reinforced brittle matrix composites using the concepts of fracture mechanics.

(2) To simulate the damage progression in the composite and predict the damage-induced tensile behavior of the composite so as to reveal the correlation between the microdamage and macroproperties of the composite.

(3) To investigate in detail the effects of three micromechanical parameters: the matrix fracture energy, interfacial debond energy, and interfacial sliding stress on the behavior of the composite.

A three-cylinder model has been developed in this study. As depicted in Fig. 1.5, the model consists of a fiber cylinder, an annulus of matrix material surrounding the fiber cylinder, and an outer infinite composite medium. Both the fiber and the matrix are isotropic, homogeneous and linearly elastic with different material constants, while the composite medium is transversely isotropic, homogeneous and linearly elastic. As shown in Fig. 1.5, the matrix cylinder is damaged by transverse cracks, which are periodically distributed in the fiber direction with interfacial debonding emanating from their tips.

Although, as in previous studies [18-22], the fiber and matrix cylinders are used to represent a typical composite unit, this model differs from those two-cylinder models [18-

22] in two major ways: the first is that the interfacial debonding is described more accurately in the framework of fracture mechanics; and the second is the introduction of the composite medium to account for the effect of the rest of the composite on the unit, which is represented by the inner two cylinders. The model can be easily reduced to a two-cylinder model by changing the material constants of the third cylinder.

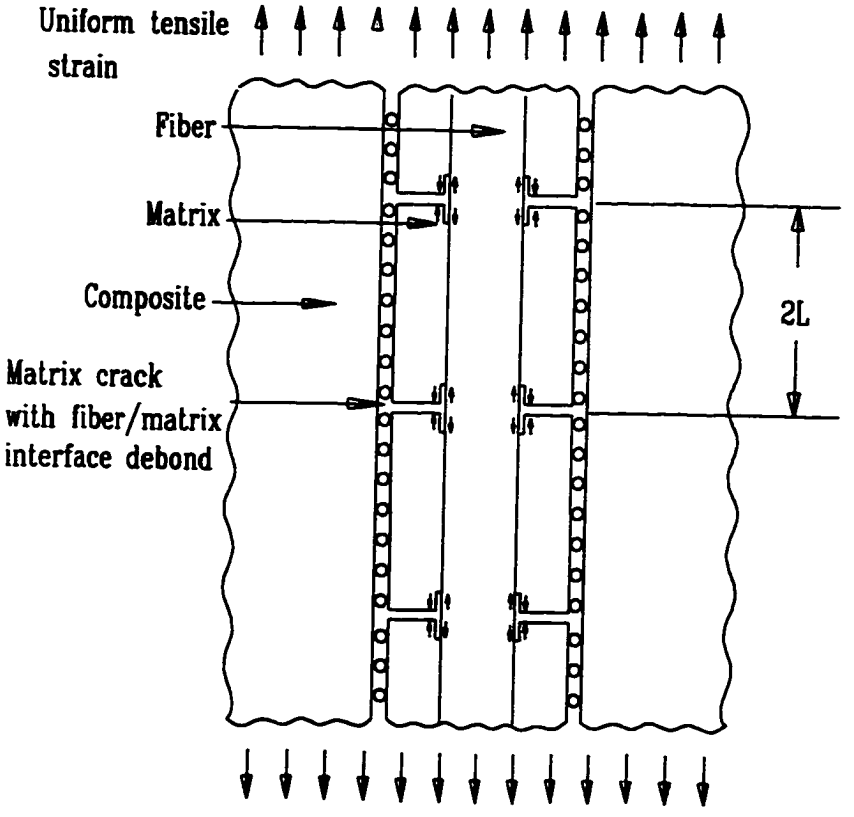

Figure 1.5 Geometry of the three-cylinder model.

The load applied to the composite is modeled by a remote uniform tensile strain in the fiber direction. The variable matrix crack spacing $2L$, as shown in Fig. 1.5, is used to

describe the status of the matrix damage and its progression. The interfacial damage is assumed as axisymmetric interfacial debonding and modeled by interfacial cracks with constant frictional stress exerted on their surfaces. The interfacial crack length is thus the measure of the interfacial damage. The damage progression within the composite, as shown in Figs. 1.2 to 1.3, is therefore simulated by the variations of the matrix crack spacing and the interfacial crack length in the model.

Singular integral equation technique was used to analyze the model. Effective numerical schemes were developed to solve a system of singular integral equations governing the model. The stress and displacement fields as well as the singular behavior at the interfacial crack tip can thus be determined very accurately.

Complemented with the concepts of linear fracture mechanics and energy balance, this model was used to simulate the damage-induced tensile behavior of a brittle-matrix composite. The influences of micromechanical parameters on the tensile stress-strain curve, such as the one in Fig. 1.1, were thoroughly investigated.

2 *Literature Review*

This chapter presents a brief review on theoretical analysis and modeling of the failure process of unidirectional fiber-reinforced brittle-matrix composites. The reviewing topics include theoretical studies on matrix cracking, fiber-matrix interfacial debonding, fiber breaking and fiber pullout. These are the most important damage modes in failure process of composites, and are closely related to this study.

2.1 Matrix cracking and related topics

The matrix cracking initiation in a composite indicates the beginning of failure of the composite, and it is therefore the first concern in composite applications. The pioneering mechanics analysis on matrix cracking in fiber-reinforced brittle matrix composites was conducted by Aveston *et al.*[11], which is commonly called the ACK model. In that model, the microstructure of the composite was taken to include the fibers, the matrix and their interfaces in an averaged sense. Tensile stresses in both fibers and matrix were assumed to be uniform across the transverse sections and the interaction between a fiber and its surrounding matrix was modeled by a constant frictional shear. The damage in the composite was modeled as fiber-bridged multiple matrix cracking, and the failure criteria were based on the concepts of energy balance and critical stress. Based on these assumptions, some fundamental equations were derived, which first revealed the relations between micromechanical parameters and macroproperties of the composite,

such as the matrix crack spacing, the critical strain of matrix crack initiation, and breaking stress of the fibers, etc. Those equations have given a good understanding of the strength and toughness of fiber-reinforced brittle matrix composites.

The ACK model has since been generalized and improved in later studies. Instead of assuming an unbonded interface [11], Aveston and Kelly [12] considered bonded interfaces, and took into account the effect of random distribution of fibers in their following study. Budiansky *et al.*[13] refined the ACK model on the basis of fracture mechanics theory. They considered both unbonded fibers that were initially held in the matrix by thermal or other strain mismatches, susceptible to frictional slip, and fibers that were weakly-bonded initially to the matrix and might be debonded by stresses. Based on the Coulomb friction law they derived the optimal thermal strain mismatches for maximum cracking strength. Furthermore they compared the theoretically predicted results for matrix cracking stress with experimental data, which are in reasonable agreement.

Marshall *et al.* [14] extended the ACK model so that the actual passage of a crack across a specimen could be considered within the framework of linear elastic fracture mechanics. They used stress intensity factors to predict the dependence of matrix cracking stress on material properties, and also proved the equivalence of their stress intensity analysis and the energy balance analysis used by previous authors. In calculating the stress intensity factor for a matrix crack, the composite was treated as a homogeneous medium; the influence of the fibers bridging on the crack was represented by closure tractions at the crack surfaces; and the stress intensity factor for the matrix was obtained from the nominal stress intensity factor for the composite through the rule of mixtures.

Their model was further refined by McCartney [15]. As reviewed in [16-17], Marshall and his associates actually described the cracking process in a quasi-macroscopic manner (since the crack itself was considered at the composite scale) with the microeffects of bridging fibers being modeled as continuous closure tractions at crack surfaces.

It should be mentioned that for the analyses reviewed above, approximate shear lag models were commonly used in analyzing fiber matrix interactions. The success of a model, therefore, depends greatly on the accuracy of the shear lag analysis used. Because of the importance of the fiber/matrix interface properties, many models (most of which are also shear lag models) have been developed specifically for the investigation of these properties. Such models can be used as a representative cell based on which the behavior of a composite can be predicted, or as the basis for experimental measurements of interfacial mechanical properties.

Early theoretical considerations of fiber-matrix interactions and fiber pull-out were mainly based on shear lag models and such failure criteria as maximum shear stress and energy balance. Here are some typical works. Greszczuk [23], Lawrence [24], Takaku and Arridge [25] calculated the distributions of shear stress along the interface and of the load in the fiber. Using approximate solutions to the compliance of shear lag models and the energy-balance concept of fracture mechanics, Stang and Shah [26] considered the mechanism of fiber pull-out. Wells and Beaumont [27] described in detail the processes of debonding and fiber pull-out in fibrous composites. They used either linear or non-linear model to describe the stress distribution in the fiber and to calculate the debonding length. They introduced the Weibull distribution to the statistical determination of fiber pull-out length. Later Wells and Beaumont [28] analyzed crack-tip energy absorption

processes including debonding, frictional sliding and pull-out, and investigated the effects of constituent material properties on the toughness of composites. Although these early investigations on the fiber/matrix debonding and fiber pull-out were extensive and the major energy-absorbing processes responsible for the improvement of the toughness of composites have been identified, rigorous mechanics analysis still remains to be developed.

Gao *et al.* [29] solved a shear lag model consisting of a fiber rod embedded in a matrix cylinder. The effects of friction at the debonded interface, the Poisson contraction and the fiber/matrix interface debonding were all considered in their study. The energy balance criterion of fracture mechanics including the friction effect was used in predicting the debonding load and the debonding length. Hutchinson and Jensen [30] analyzed a similar problem with more effects being taken into account. They treated the debonding process as a mode II crack, characterized the sliding of debonded interface by constant or Coulomb friction, and accounted for the mismatches of thermal expansion between the fiber and matrix in both radial and axial directions. They derived approximate closed-form solutions to the model, and also assessed the solutions using an accurate numerical analysis. By including thermal expansion mismatches their model is particularly useful in analyzing high-temperature behaviors of composites. Charalambides and Evans [31] also investigated a similar two-cylinder model rigorously using the finite element method. For an open and friction-free debonded crack, they studied steady-state debonding behavior and its sensitivity on thermal expansion mismatch.

McCartney [32] obtained an approximate analytical solution to a two-cylinder model that satisfies most of the field equations and boundary conditions required by an

exact solution. The author used the solution to examine the stress transfer between the fiber and matrix for either a transverse matrix crack or a fiber break situation, with mismatches in both thermal expansion coefficients and Poisson ratios being taken into consideration. Kuo and Chou [18] introduced their modified shear-lag analysis on a two-cylinder model with matrix cracks and interfacial debonds for predicting matrix crack initiation strain. Weitsman and Zhu [19] analyzed a similar two-cylinder model approximately using elasticity methods. Both works considered constant friction caused by relative movement over asperities at the fiber/matrix interface.

Similar analyses have also been widely used in developing experimental techniques for measuring interfacial mechanical properties. In [33-36] shear-lag models and the push-in/pull-out techniques were used to measure interfacial mechanical properties. Cox [37] developed a simple shear lag model to consider interfacial sliding during thermal cycling, and later Cox *et al.* [38] used the model to determine the temperature dependence of interfacial properties in their experiments. Marshall [39] examined in detail the use of the model proposed in [30] to deduce interfacial properties from experimental measurements of fiber sliding. Recently Lu and Mai [40] have developed their theoretical model for the slice-compression test to measure interfacial mechanical properties.

The analysis on the two-cylinder model can be combined into fiber-bridging analysis of CMCs to determine the effects of debonding at fiber/matrix interfaces on matrix cracking (such as the work reported in [23-24]). A popular and convenient way to embody the mechanical effects of bridging fibers on a composite with a crack is to introduce a continuous distribution of non-linear springs that connect the opposing faces of the crack in a homogeneous material [14-15]. Using this idea and the results in [14,

30], Budiansky *et al.* [41] investigated the relations between matrix cracking and fiber-matrix debonding including the frictional effect. Marshall and Cox [42] extended the approach to analyze matrix cracking in composites accompanied by fiber failure. Budiansky and Cui [43] used the method to investigate the tensile strength of a CMC containing a crack-like flaw. Bao and Suo [44] presented a review on crack-bridging concepts.

The validity of constant or Coulomb friction has been discussed by Bao and Song [45]. They proposed some slip-dependent bridging models for the interface friction. As for the justification of the spring modeling of fiber bridging, some questions have arisen too. Xia *et al.* [46] examined critically the use of the spring model in large interface sliding situations, and developed a large scale sliding model (LSS). They compared the predictions from the LSS model with those from the line-spring model for composites with through-cracks. For bridged cracks over the entire range of sizes from a small one spanned by a single fiber to very large cracks, the validity of using distributed spring models has been examined in detail by Meda and Steif [47, 48]. They presented the conditions under which the distributed spring models can be expected to yield reliable results.

Because distributed spring models are usually not applicable to a small crack bridged by a single fiber or pure matrix flaws, it is therefore required to develop effective analysis for small cracks. Since discrete fibers and the interactions between interfaces and microcracks should be considered in the analysis, the resulting problems are usually very complicated, and in most cases numerical techniques must be used to solve the problem.

Wang *et al.* [16, 17] proposed a local flaw model to study the relationships between the stresses inducing matrix crack initiation and the influencing factors in microstructure for some CMCs. Their microstructural model consists of two adjacent fibers separated by matrix material and a uniform composite medium outside the fibers with a matrix and some interface flaws present. A finite element procedure incorporating the unit cell was developed for fracture analysis. They predicted the initiation stress for matrix cracking and compared it with their experimental results.

Some authors used the singular integral equation technique to analyze the fracture of two-cylinder models. For instance, Erdogan and Ozbek [49] first considered the problem of annular interfacial cracks. Recently Wijeyewichrema *et al.* [50-53] have investigated a series of axisymmetric problems. The first problem they solved was that of an infinitely long elastic fiber embedded into an infinite cracked matrix, with perfect interfacial bonding [50]. The second problem they solved was similar to the first one except that the outer matrix was finite [51]. In the third one multiple matrix cracking along the axial direction was investigated also with perfect interface bonding [52]. In all three problems the composite cylinders were under uniform stretching at infinity, and the solutions were given in terms of stress intensity factors and interfacial stresses, which were functions of the material constants of the fiber and matrix and geometry parameters, such as the locations and lengths of cracks. The bonding conditions were considered in the fourth paper [53]. The model used in that study was also a composite cylinder of finite outer radius. However, the interfacial slip was considered with matrix crack terminating and blunting at the interface. The solution was given in terms of interfacial stresses and crack opening displacements. Kaw and Pagano [54] investigated the

thermoelastic response of a composite cylinder containing an annular matrix crack, with the bond represented by distributed shear springs. The shear stress at the interface was then related linearly to the difference of the axial displacements between the fiber and the matrix at the interface. By changing the stiffness of the spring, a varying degree of sliding resistance could be represented. The results were presented in terms of stress intensity factors and interfacial stresses under both mechanical and thermal loads. The more general and meaningful fracture analysis of a two-cylinder problem has been completed recently by Zhang *et al.* [55]. The authors used the same two-cylinder geometry as that in [49,50], but with both matrix and interfacial cracks present. Simultaneous interfacial and matrix cracking was investigated thoroughly and detailed results were presented in terms of stress intensity factors.

2.2 Multiple matrix cracking and associated damage progression

After the initial matrix cracking and ensuing interfacial debonding, the damage will progress in a mode of multiple matrix cracking accompanied by further interfacial debonding. The multiple matrix cracking is mainly responsible for the non-linear behavior of the brittle-matrix composite before the occurrence of fiber breaking and pull-out. Predicting the non-linear behavior of the brittle composite is therefore closely related to the analysis of multiple matrix cracking and its progression.

Using their refined shear-lag analysis [18] on a cracked two-cylinder configuration with finite matrix crack spacing, which was estimated from experimental results, Kuo and Chou [20] examined the multiple matrix cracking of unidirectional and cross-ply ceramic matrix composites. They predicted the moduli and matrix crack initiation stresses for the

composites, and investigated the effects of bonding energy and debonding length on the stresses. However, they did not consider matrix cracking evolution. Using a similar model Lee and Daniel [21] developed their analysis for multiple matrix cracking. Assuming that new matrix cracks form at the middle cross sections of existing cracks when the matrix stress exceeds an ultimate matrix strength, they obtained crack densities to characterize the matrix crack evolution and predicted the tensile behavior of the composite. Starting from their approximate analysis on a two-cylinder model and using the energy balance criterion instead of the ultimate strength, Weitsman and Zhu [19] investigated the influences of micromechanical parameters on the response of uniaxially fiber-reinforced ceramic composites under monotonically increasing loading. More recently Solti, Mall and Robertson [22] extended Kuo and Chou's shear-lag analysis [18] to analyze the damage progression dominated by multiple matrix cracking. They used a critical matrix strain energy, which was estimated from test results, to determine the crack density and an interfacial shearing strength to control the interface debonding. They also investigated the effects of some micromechanical parameters on the response of a ceramic-matrix composite during loading and unloading processes.

The above analyses have clearly shown that the multiple matrix cracking is mainly responsible for the nonlinear behavior of the composite. The influence of the toughness of the fiber-matrix interface on the behavior of the composite, however, has not been addressed yet. It has been known that the toughness of the fiber-reinforced composite is mainly governed by the behavior of the interface, which in turn is greatly influenced by interfacial flaws and their development. Such flaws could be voids formed during manufacturing or minute cracks caused by debonding during loading. Both may be

approximated by interface cracks. Although weak fiber-matrix interfacial bond is required for a tough composite, it may still be appropriate to analyze the interface debond using the principle of fracture mechanics. The exact asymptotic solution near an interface crack tip has been obtained by several authors [56-58]. Although the solution involves oscillatory stress singularities around the crack tip, which are interpreted as the results of overlapping crack surfaces near the crack tip, the stress intensity factors and the strain energy release rates thereby derived can still be used as suitable characteristic parameters to describe the crack-tip behavior [59]. Nevertheless, it is difficult to combine such a description with an analysis such as shear-lag analysis without the capability to capture stress singularities.

2.3 Fiber breaking and fiber-matrix interfacial debonding

The above studies are mainly based on the assumption that fibers remain intact during matrix cracking. However the actual damage modes, including the initiation of microcracks, their propagation and interaction, may be strongly affected by many factors, such as loading condition, structural geometry, manufacturing process, the properties of constituent materials, etc. Instead of remaining intact, some fibers may break at very early stage of loading, owing to pre-existing flaws on fiber surfaces. A broken fiber will then induce stress concentration in its surroundings. The magnitude and extent of such concentration, as well as its influence on the behavior of the composite, should also be considered when designing composite materials.

Much effort has been expanded to analyze fiber breakage. Using the shear lag model, Hedgepeth [60] first analyzed stress concentration near broken fibers in two-

dimensional filamentary composites. Hedgepeth and Van Dyke [61] considered three-dimensional cases. Because of its simplicity, the shear lag model has been widely used by many authors in analyzing the effects of broken fibers: Reedy [62, 63], Goree and Gross [64], and Rossettos and Shishesaz [65], to name a few. In general, the shear lag model can only give stress distributions in an average sense.

Some serious attempts at the solution to the problem of a broken fiber embedded in an infinite matrix have also appeared in the literature. Muki and Sternberg [66], who treated the fiber as a one-dimensional continuum and developed an integral equation for the problem, first investigated the load-absorption by a discontinuous filament in a fiber-reinforced composite. Later a rigorous three-dimensional solution to this problem was developed by Ford [67]. In both cases the authors assumed perfect fiber-matrix interface bond, which is obviously unrealistic in many composites. In order to reveal the influence of the more realistic weak bonding, Dollar and Steif [68] introduced unbonded frictional fiber-matrix interface described by Coulomb friction law in a two-dimensional model composite and analyzed the problem using the integral equation technique. Under the same assumption for the fiber-matrix interface, Schwietert and Steif [69] solved an axisymmetric bimaterial problem with a broken fiber using the integral equation method at the interface. The same problem was also investigated by Aksel *et al.*[70] using the finite element method. The main concern in their analyses was the load transfer through the weak fiber-matrix interface governed by the Coulomb friction law after the break of a fiber. The actual interface bonding, however, depends on the properties of the fiber and the matrix and the manufacturing process, and may not be so weak. Recently, Zhang *et al.* [71] analyzed the fiber break problem in a brittle composite using fracture mechanics

approach with the singular integral equation technique. Using strain energy release rates, the authors investigated the initiation of fiber break and the possible propagation modes of the fiber break. They discussed the possibility of crack-penetration into the surrounding matrix from the broken fiber, which did not appear to have been addressed in literature before.

3 *Development of a Three-Cylinder Model*

3.1 Experimental studies on ceramic matrix composites

Experimental studies have shown that the tensile behavior of a fiber-reinforced ceramic matrix composite is closely associated with damage modes in the composite [7-10]. Using an *in situ* observation technique has made it possible to record damage modes and related changes in elastic moduli in the composite simultaneously. Since the theoretical modeling in this study is based on the experimental investigation completed at The City College of New York (CCNY), the following brief introduction will be limited to the experimental procedure developed at CCNY and associated results [9, 10].

3.1.1 Experimental procedure

The experimental arrangement and the specimen geometry used to conduct tensile test and observe the surface of test specimens during loading are shown in Fig. 3.1. A specimen is mounted to the tensile substage firmly and the substage is then placed inside the chamber of a Hitachi S-2400 SEM. By using the X-Y staging control of the scanning electron microscope, micrographical patterns on the central gage area of the specimen can be observed and recorded *in situ*. The tensile substage is driven by a variable-speed motor to load the specimen. The load and the related deflection can be recorded digitally. The applied load is increased gradually until the specimen fails totally. During this loading process, damage in the specimen initiates and propagates mainly in such modes as matrix

cracking, fiber-matrix interfacial debonding, fiber breaking and pull-out. All these damage modes can be observed and recorded *in situ*.

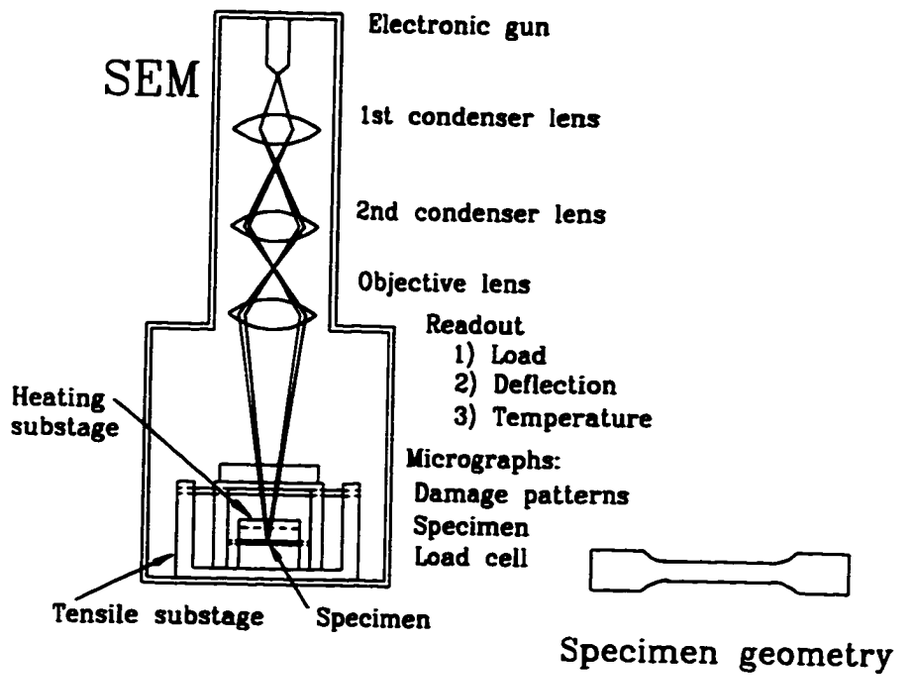

Fig. 3.1 The tensile test set-up under a scanning electron microscope with tensile/heating substage and the specimen geometry.

3.1.2 Experimental results

A typical tensile stress-strain curve of a Nicalon/CAS II with 40% fiber volume fraction at room temperature is shown in Fig. 3.2. The general features can be easily identified from this curve and correlated to the recorded damage modes. Initially the behavior of the composite was linearly elastic up to a strain of approximately 0.12%. The modulus for this linear portion was approximately equal to that given by the rule of

mixtures. Corresponding to this early loading, the composite remained intact as shown in Fig. 3.3, which is identical to Fig. 1.2.

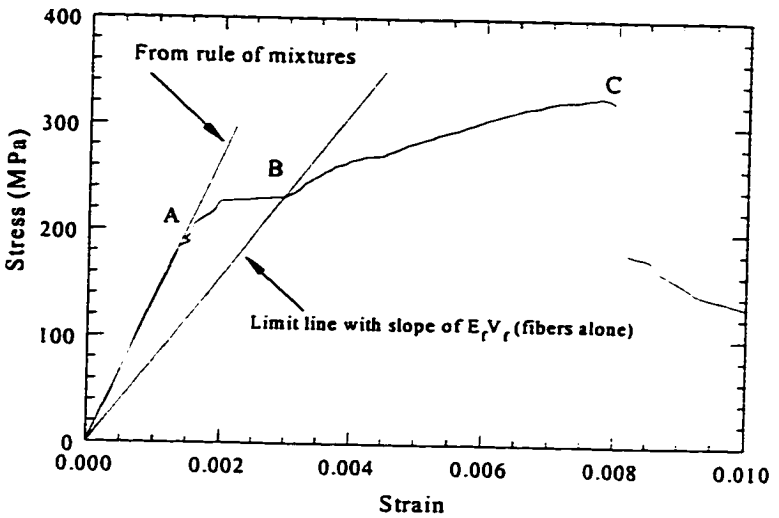

Fig. 3.2 A typical tensile stress-strain curve of Nicalon/CAS II tested at room temperature ($V_f = 0.4$, $E_f = 195$ GPa, $E_m = 95$ GPa).

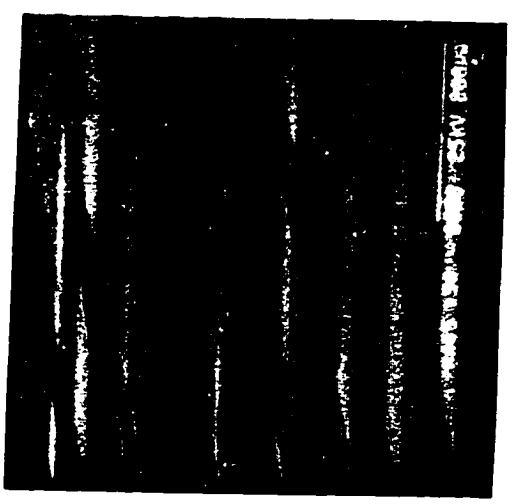

Fig. 3.3 SEM micrograph of undamaged unidirectional Nicalon/CAS II.

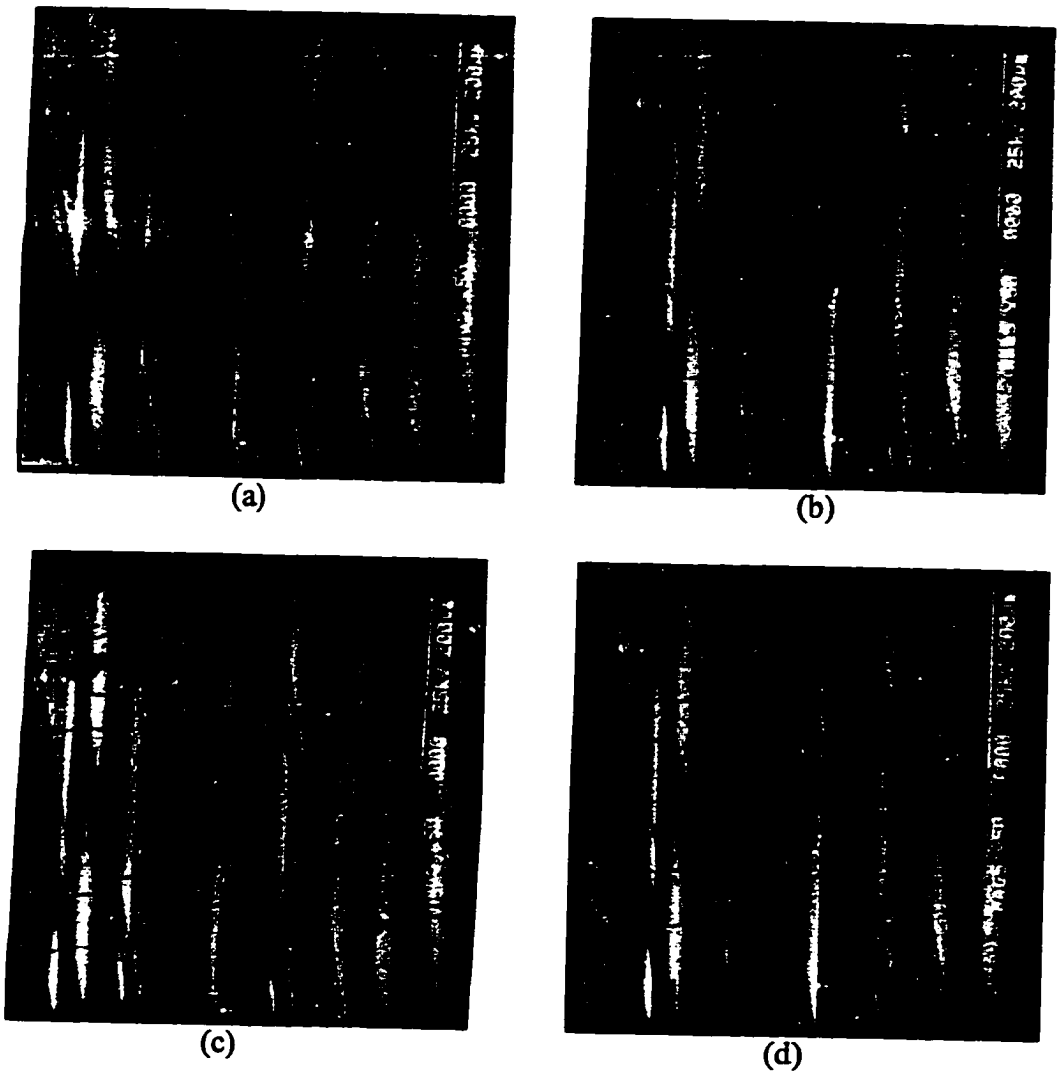

Fig. 3.4 SEM micrographs showing progression of multiple matrix cracking with gradually increasing loading from (a) to (d).

When the load increased further, transverse matrix cracking initiated, as indicated by SEM micrograph (a) in Fig. 3.4 (which is identical to (a) in Fig. 1.3), and the stress-strain curve began to deviate from the initial linear portion. It is believed that Point A on the curve indicates the beginning of matrix cracking. Soon after the formation of the matrix cracks, fiber-matrix interfacial debonding occurred. When the specimen was

loaded further, matrix cracks multiplied and are bridged by intact fibers. This phenomenon is called *fiber-bridged multiple matrix cracking*. The SEM micrographs (a-d) in Fig. 3.4 show clearly the progression of the multiple matrix cracking with increasing loading. The multiple matrix cracking, interfacial debonding and the frictional-interfacial sliding on debonded areas are all energy dissipation mechanisms. It is believed that these mechanisms make the brittle composite behave non-linearly. The progression continued with continuous loading until the matrix was saturated with transverse matrix cracks. Point B on the stress-strain curve indicates roughly the ending of multiple matrix cracking.

Following the saturation of matrix cracks, further loading caused further matrix crack opening, fiber breaking and pull-out. Ideally, if fiber breaking does not occur, the elastic moduli in this region (starting from Point B) should be greater than or at least equal to that for the fibers alone ($E_f V_f$). The experimental curve, however, shows much smaller moduli in this portion, implying occurrence of serial fiber breaking. Fiber breaking and pull-out continued with increasing stretching until the final separation of the specimen occurred.

The above test results affirm that failure of the composite in tension occurs progressively in several stages: matrix cracking, then multiple matrix cracking accompanied by fiber-matrix interfacial debonding, and finally fiber breaking and pull-out. The following model was developed to analyze initial matrix cracking, multiple matrix cracking and fiber-matrix interfacial debonding. The final stage of the damage progression, fiber breaking and pull-out, is out of the scope of this study.

3.2 Theoretical modeling

3.2.1 Three-cylinder model

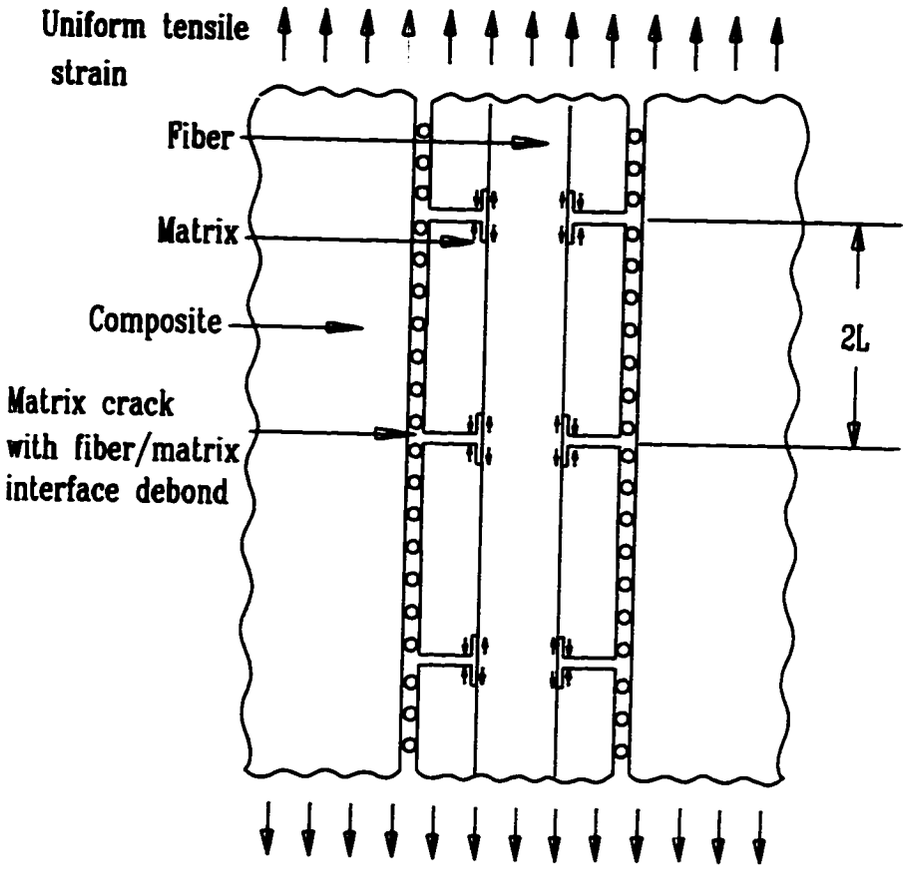

Fig. 3.5 Schematic of the three-cylinder model.

A three-cylinder model as shown in Fig 3.5 was proposed to analyze the experimentally observed damage modes. In the model, a single fiber with surrounding matrix material which has been damaged by transverse cracks is used to represent a typical damaged composite. The influence of the remaining composite is simulated collectively by a homogeneous composite medium surrounding the representative unit.

Transverse matrix cracks are bridged by the intact fiber and spaced at an average distance $2L$. The fiber-matrix interfacial debonding is modeled as interfacial cracks with frictional force being present. Since the matrix cracks are distributed periodically, one only needs to analyze a representative unit shown in Fig 3.6.

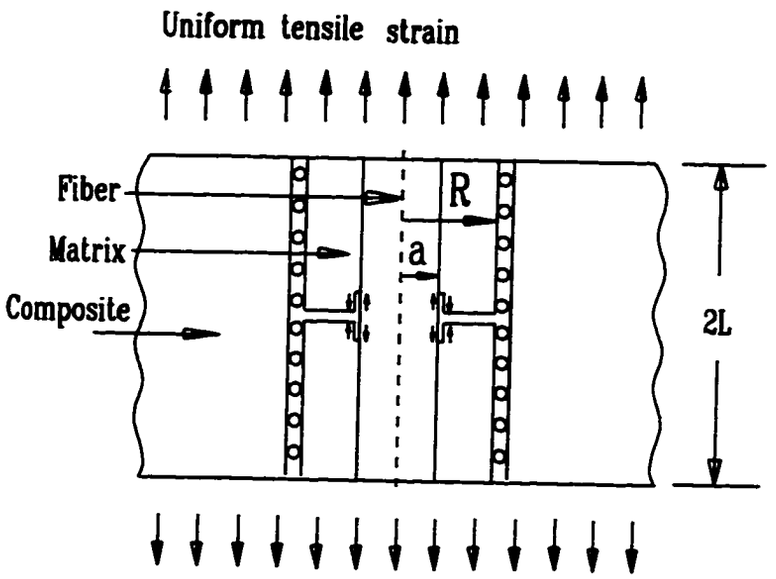

Fig. 3.6 A representative unit.

3.2.2 Damage modeling

The microdamage modes considered in the model are multiple matrix cracking, interfacial debonding, and frictional sliding at debonded interfacial area. The effective behavior of the composite can be modeled by the behavior of the fiber-matrix cylinder. The onset of matrix cracking can be modeled by multiple cracking with very large spacing $2L$ and very short interfacial debonding. Then as the loading continues, either the

multiple matrix cracking may evolve with the spacing $2L$ being reduced, or the interfacial debonding may propagate further, depending on the micromaterial properties of the constituents of the composite.

While the matrix crack spacing remains unchanged, the interfacial debonding is the prospective damage mode. As shown in Fig. 3.6, it is assumed that the representative volume is loaded by uniform strain ε, and that a constant frictional stress τ_s exists at the debonded interfacial area. It is also assumed that the matrix crack plane remain to be the plane of symmetry during the interfacial debonding. Using basic concepts of linear fracture mechanics, the criterion for interfacial debonding can be established as

$$G_{12} = C_{12}(k_1^2 + k_2^2) \geq \gamma_{db} \tag{3.1}$$

where G_{12} is the interfacial debonding energy release rate, C_{12} is a constant depending on material constants and the crack length, k_1 and k_2 are stress intensity factors of mode I and mode II at the interfacial crack tip, respectively (see their definitions in Eqs. (A.42)), and γ_{db} is the interfacial debonding energy. C_{12} has been derived by Malyshev and Salganik [72] and is given in Eq. A.44. Using the principle of superposition, one can express the stress intensity factors as

$$k_1 = C_{p1}\varepsilon - C_{s1}\tau_s, \tag{3.2a}$$

$$k_2 = C_{p2}\varepsilon - C_{s2}\tau_s, \tag{3.2b}$$

where C_{p1}, C_{p2}, C_{s1} and C_{s2} are functions of geometry parameters. Substituting the above equations for k_1 and k_2 in Eq. (3.1), one obtains the following equation for determining the critical strain for interfacial debonding:

$$(C_{p1}^2 + C_{p2}^2)\varepsilon^2 - 2(C_{p1}C_{s1} + C_{p2}C_{s2})\varepsilon + (C_{s1}^2 + C_{s2}^2)\tau_s^2 = \gamma_{db} / C_{12} \tag{3.3}$$

For multiple matrix cracking, one can also establish a criterion using an energy balance concept. For the upper half portion of the unit depicted in Fig. 3.6, after the strain is applied, the strain energy U_1 stored in that portion of the fiber-matrix cylinder can be expressed as

$$U_1 = \frac{1}{2}\pi R^2 \sigma_1 \varepsilon L - W_s, \tag{3.4}$$

where R is the radius of the matrix cylinder, σ_1 is the average stress over the fiber-matrix cylinder, and W_s is the energy dissipated due to frictional sliding along the interfacial crack. If the multiple cracking evolves, it is assumed that new matrix cracks appear at the middle sections between old cracks and the spacing is therefore reduced from $2L$ to L, while the interfacial crack length remains unchanged. After further matrix cracking has occurred at the same strain, the strain energy stored in the same volume (upper half portion of the fiber-matrix cylinder in Fig. 3.6) can then be expressed as

$$U_2 = 2\frac{1}{2}\pi R^2 \sigma_2 \varepsilon \frac{L}{2} - 2W_s = \frac{1}{2}\pi R^2 \sigma_2 \varepsilon L - 2W_s \ , \tag{3.5}$$

here σ_2 is the new average stress over the fiber-matrix cylinder associated with new matrix crack spacing L. Considering the balance of energy in this prosess yields the criterion for the progression of multiple matrix cracking:

$$U_1 - U_2 \geq \gamma_m \pi (R^2 - a^2) + 2\pi a c_3 \gamma_{db} \ , \tag{3.6}$$

where γ_m is the critical surface energy for the matrix, a is the radius of the fiber, and c_3 is the interfacial crack length (measured from matrix crack plane). The second term on the

right side in the above equation accounts for the energy required for the associated interfacial debonding.

The frictional energy dissipation W_s associated with interfacial slip can be evaluated from the difference of the axial fiber and matrix displacements along the interfacial crack. Under the action of both the applied strain ε and frictional stress τ_s, the difference of the displacements can be calculated as

$$u_z^2(z) - u_z^1(z) = \frac{-1}{2\mu_1}\int_{c_3}^{z}\left[\varepsilon\varphi_4^p(t) - \tau_s\varphi_4^s(t)\right]dt, \tag{3.7}$$

where $u_z^1(z)$ and $u_z^2(z)$ are the axial displacements of the fiber and matrix on the debonded interface, respectively, μ_1 is the shear modulus of the fiber, $\varphi_4(t)$ is the axial dislocation along the interfacial crack, with superscripts p and s being used to denote the dislocations caused by a unit tensile strain and a unit shearing stress on the interfacial crack, respectively. (The definition of this dislocation function will be given later in this chapter.) The frictional energy dissipation can now be calculated from the dislocation functions and expressible as

$$W_s = 2\pi a\tau_s\int_0^{c_3}\left(u_z^2 - u_z^1\right)dz = \frac{\pi a\tau_s}{\mu_1}\int_0^{c_3} t\left[\varepsilon\varphi_4^p(t) - \tau_s\varphi_4^s(t)\right]dt\ . \tag{3.8}$$

Since the average stresses σ_1 and σ_2 are proportional to the given strain ε with different proportionality constants, one can solve Eq. (3.6) for critical strain, the only unknown in that equation for multiple matrix cracking.

If both interfacial debonding and multiple matrix cracking are considered simultaneously, the experimentally observed damage modes in a composite can be

simulated and its tensile stress-strain curve can be predicted. The simulation and prediction procedure may be summarized as follows. For a given composite with given material constants and micromechanical parameters γ_m, γ_{db} and τ_s, the simulation can begin with a very large matrix crack spacing $2L$ and a very small interfacial debond. Then two critical strains can be calculated from Eqs (3.3) and (3.6). The smaller one is the possible strain for the damage to evolve. Based on this critical strain and the related configuration, an effective (or average) stress can be determined, and therefore the effective elastic modulus in the loading direction can be computed. Now after the damage has been allowed to progress a small step in the predicted mode (i.e., either interfacial debonding or multiple matrix cracking), one can calculate a new possible critical strain, a new effective stress and a new elastic modulus for the updated configuration of the model. This process can be repeated until the fiber is debonded completely from the matrix or matrix crack saturation occurs. A series of strains can be obtained and a simulated stress-strain curve can thus be plotted from these strains and associated stresses. The detailed numerical results are presented in Chapter 4.

3.3 Formulation of the model

3.3.1 Description of the problem

As shown in Fig. 3.6, the geometry of the model consists of a cylindrical rod representing a fiber, a cylindrical tube representing the surrounding matrix, and the outer composite medium. The fiber and the matrix are both homogeneous, isotropic and linearly elastic; while the composite medium is homogeneous, transversely isotropic and

linearly elastic. The fiber and the matrix are bonded together perfectly except for some debonded regions, in which sliding can occur and frictional forces may exist. For the matrix and the composite medium interface it is assumed that neither bonding nor friction exists. By varying the material constants of the composite medium, the model can be reduced to a common two-cylinder model of finite outer radius with a free outer surface or with an outer surface which is restricted in radial direction but free in axial direction. A series of transverse matrix cracks and associated interfacial cracks are used to model the damage.

Because of the complexity of both the geometry and crack configuration, it is difficult to formulate the problem directly. The formulation was actually divided into two parts: the first part is an accurate formulation of the three cylinders with a single matrix crack combined with a fiber-matrix interface crack (Fig. 3.7); the second part is the solution of the multiple matrix cracking (Fig. 3.6), which was derived using the solution of the first one and iterative technique. The first problem can also be considered as the limiting case of the second one as the matrix crack spacing $2L$ goes to infinity.

3.3.2 Formulation of three cylinders with a single matrix crack and an interfacial crack

The solution of the problem can be obtained by the superposition of two problems: the first is the uncracked geometry under given loading, and the second, called the perturbation problem as shown in Fig 3.7b, is the cracked geometry loaded on the crack surfaces by the negative of stresses obtained from the first one. Since it is not difficult to find the exact solution of the first one, the following will focus on the formulation of the

perturbation problem. Unless stated otherwise, superscripts and subscripts 1, 2, and 3 refer to the fiber, the matrix and the composite medium, respectively.

Since the fiber and the matrix can be treated as a basic composite cell, their radii should be chosen so that

$$\frac{a^2}{R^2} = V_f, \tag{3.9}$$

where V_f is the fiber volume fraction of the composite. μ_i and ν_i (i = 1, 2) are used to denote the shear moduli and Poisson's ratios of the fiber (i = 1) and the matrix (i = 2), respectively. For the transversely isotropic composite medium, five independent effective material constants are needed to characterize the generalized Hooke's law [73]:

$$\begin{aligned}
\varepsilon_{rr} &= a_{11}\sigma_{rr} + a_{12}\sigma_{\theta\theta} + a_{13}\sigma_{zz} \\
\varepsilon_{\theta\theta} &= a_{12}\sigma_{rr} + a_{11}\sigma_{\theta\theta} + a_{13}\sigma_{zz} \\
\varepsilon_{zz} &= a_{13}(\sigma_{rr} + \sigma_{\theta\theta}) + a_{33}\sigma_{zz} \\
\gamma_{rz} &= a_{44}\tau_{rz}
\end{aligned} \tag{3.10}$$

Expressing the coefficients of deformation by means of the engineering constants, one has:

$$\begin{aligned}
a_{11} &= \frac{1}{E_{31}}, \; a_{12} = -\frac{\nu_{31}}{E_{31}}, \; a_{33} = \frac{1}{E_{32}}, \\
a_{13} &= -\frac{\nu_{32}}{E_{32}}, \; a_{44} = \frac{1}{G_{32}},
\end{aligned} \tag{3.11}$$

where E_{31}, E_{32} are Young's moduli in the plane of isotropy and in z direction, respectively, ν_{31} is the Poisson's ratio in the plane of isotropy, ν_{32} is the Poisson ratio characterizing transverse contraction in the plane of isotropy due to the tension in z direction, and G_{32} is the shear modulus in r-z plane. These material constants can be

expressed in terms of the constituent properties of the composite. Various micromechanical models are available for predicting the coefficients, such as those due to Hashin and Rosen [74-76], which are presented in Appendix B.

For the isotropic cylindrical fiber and matrix, the axisymmetric displacement and stress fields can be easily expressed in terms of Love's stress functions, which are biharmonic [50, 51]:

$$\Phi_1(r,z) = \frac{2}{\pi}\int_0^\infty [f_1(s)I_0(rs) + f_2(s)rsI_1(rs)]\sin(zs)ds$$

$$+ \int_0^\infty f_0(p)p(2\nu_1 + zp)e^{-zp}J_0(rp)dp, \tag{3.12}$$

$$\Phi_2(r,z) = \frac{2}{\pi}\int_0^\infty [f_3(s)I_0(rs) + f_4(s)rsI_1(rs) + f_5(s)K_0(rs)$$

$$+ f_6(s)rsK_1(rs)]\sin(zs)ds + \int_0^\infty g_0(p)p(2\nu_2 + zp)e^{-zp}J_0(rp)dp, \tag{3.13}$$

where f_i (i=0,...,6) and g_0 are unknown functions, and J_j, I_j, K_j (j=0,1) are Bessel functions of the first kind, and modified Bessel functions of the first kind and the second kind, respectively. The expressions for any displacement and stress components in the fiber and matrix can easily be derived from the above two functions (see Appendix C).

For the transversely isotropic composite medium, as in the case of an isotropic body, it is possible to introduce a stress function $\Phi_3(r,z)$, which the stresses are related to by [73]:

$$\sigma_{rr} = -\frac{\partial}{\partial z}\left[\frac{\partial^2\Phi_3}{\partial r^2} + \frac{b_c}{r}\frac{\partial\Phi_3}{\partial r} + a_c\frac{\partial^2\Phi_3}{\partial z^2}\right],$$

$$\sigma_{\theta\theta} = -\frac{\partial}{\partial z}\left[b_c\frac{\partial^2\Phi_3}{\partial r^2} + \frac{1}{r}\frac{\partial\Phi_3}{\partial r} + a_c\frac{\partial^2\Phi_3}{\partial z^2}\right],$$

$$\sigma_{zz} = \frac{\partial}{\partial z}\left[c_c\frac{\partial^2\Phi_3}{\partial r^2} + \frac{c_c}{r}\frac{\partial\Phi_3}{\partial r} + d_c\frac{\partial^2\Phi_3}{\partial z^2}\right], \tag{3.14}$$

$$\tau_{rz} = -\frac{\partial}{\partial r}\left[\frac{\partial^2\Phi_3}{\partial r^2} + \frac{1}{r}\frac{\partial\Phi_3}{\partial r} + a_c\frac{\partial^2\Phi_3}{\partial z^2}\right],$$

where

$$a_c = \frac{a_{13}(a_{11}-a_{12})}{a_{11}a_{33}-a_{13}^2},\quad b_c = \frac{a_{13}(a_{13}+a_{44})-a_{12}a_{33}}{a_{11}a_{33}-a_{13}^2},$$

$$c_c = \frac{a_{13}(a_{11}-a_{12})+a_{11}a_{44}}{a_{11}a_{33}-a_{13}^2},\quad d_c = \frac{a_{11}^2-a_{12}^2}{a_{11}a_{33}-a_{13}^2}. \tag{3.15}$$

The displacement field can also be expressed in terms of this stress function as:

$$u_r = -e\frac{\partial^3\Phi_3(r,z)}{\partial r\partial z},\quad u_z = a_{44}\nabla^2\Phi_3(r,z) + g\frac{\partial^2\Phi_3(r,z)}{\partial z^2}, \tag{3.16}$$

where ∇^2 is the axisymmetric Laplacian and

$$e = a_{11} + a_{12}b_c - a_{13}c_c,\quad g = a_{13}(1+b_c-2a_c) + a_{33}(d_c-c_c). \tag{3.17}$$

Introducing the following notation

$$s_1 = \sqrt{\frac{a_c+c_c+\sqrt{(a_c+c_c)^2-4d_c}}{2d_c}},\quad s_2 = \sqrt{\frac{a_c+c_c-\sqrt{(a_c+c_c)^2-4d_c}}{2d_c}}, \tag{3.18}$$

and the operators

$$\nabla_i^2 = \frac{\partial^2}{\partial r^2} + \frac{1}{r}\frac{\partial}{\partial r} + \frac{1}{s_i^2}\frac{\partial^2}{\partial z^2},\quad (i=1,2), \tag{3.19}$$

the governing equation for the stress function can be written as follows:

$$\nabla_1^2 \nabla_2^2 \Phi_3(r,z) = 0. \tag{3.20}$$

Through direct substitution, it can be shown that the governing equation (3.20) is satisfied by the following expression for the stress function:

$$\Phi_3(r,z) = \frac{2}{\pi}\int_0^\infty \left[f_7(s)K_0(rs/s_1) + f_8(s)K_0(rs/s_2)\right]\sin(zs)ds, \tag{3.21}$$

where f_7 and f_8 are unknown functions to be determined. The displacement and stress fields for the composite cylinder can be derived readily from the stress function (see Appendix C)

Introducing three dislocation functions:

$$\varphi_2(r) = \frac{\mu_2}{1-\nu_2}\frac{\partial u_z^2(r,+0)}{\partial r}, \tag{3.22a}$$

$$\varphi_3(z) = 2\mu_1 \frac{\partial}{\partial z}\left[u_r^2(a+0,z) - u_r^1(a-0,z)\right], \tag{3.22b}$$

$$\varphi_4(z) = 2\mu_1 \frac{\partial}{\partial z}\left[u_z^2(a+0,z) - u_z^1(a-0,z)\right], \tag{3.22c}$$

and considering continuity and boundary conditions make all the unknowns f_i (i=0,...,8) and g_0 in the stress functions expressible in terms of these three new functions. After some lengthy manipulations (see Appendix C), the following system of three singular integral equations is obtained:

$$\frac{1}{\pi}\int_a^R \frac{\varphi_2(t)}{t-r}dt + \frac{2}{\pi}\int_a^R k_{22}(t,r)\varphi_2(t)dt + \frac{2}{\pi}\sum_{j=3}^{4}\int_0^{c_3} k_{2j}(t,r)\varphi_j(t)dt = -p_2(r),$$

$$a < r < R, \tag{3.23a}$$

$$\frac{1}{\pi}\int_0^{c_3}\left(\frac{1}{t-z}+\frac{1}{t+z}\right)\varphi_3(t)\,dt+\gamma\varphi_4(z)$$

$$+\frac{2}{\pi\gamma_{11}}\sum_{j=2}^{4}\int_{b_j}^{c_j}k_{3j}(t,z)\,\varphi_j(t)\,dt=\frac{-p_3(z)}{\gamma_{11}},\qquad 0<z<c_3, \tag{3.23b}$$

$$\frac{1}{\pi}\int_0^{c_3}\left(\frac{1}{t-z}-\frac{1}{t+z}\right)\varphi_4(t)\,dt-\gamma\varphi_3(z)$$

$$+\frac{2}{\pi\gamma_{11}}\sum_{j=2}^{4}\int_{b_j}^{c_j}k_{4j}(t,z)\,\varphi_j(t)\,dt=\frac{p_4(z)}{\gamma_{11}},\qquad 0<z<c_3, \tag{3.23c}$$

where $b_2=a$, $c_2=R$, $b_4=b_3$, $c_4=c_3$, $\gamma=\gamma_{12}/\gamma_{11}$,

$$\gamma_{11}=\frac{\lambda+\kappa_1+1+\lambda\kappa_2}{2(\lambda+\kappa_1)(1+\lambda\kappa_2)},\quad \gamma_{12}=\frac{\lambda+\kappa_1-(1+\lambda\kappa_2)}{2(\lambda+\kappa_1)(1+\lambda\kappa_2)}, \tag{3.24a}$$

$$\lambda=\mu_1/\mu_1,\qquad \kappa_i=3-4\nu_i\,(i=1,2), \tag{3.24b}$$

and $k_{2j}(t, r)$ (j=2, 3, 4), $k_{ij}(t,z)$ (i=3, 4, j=2, 3, 4), are Fredholm kernels (see Appendix C for details).

3.3.3 Formulation of multiple matrix cracking

As mentioned before, the analysis of multiple matrix cracking can be reduced to the analysis of a representative unit (Fig. 3.6). Using the principle of superposition, the analysis of this unit can be decomposed into solving two problems, as shown in Fig. 3.8. The first is the uncracked unit loaded by the same uniform tensile strain as that exerted on the original one, and the second is the cracked unit loaded on the crack surfaces by tractions, which are the negative of stresses obtained from the solution of the first one and

the frictional force. Axial constraints must also be imposed on the top and bottom edges of the second geometry, because the original geometry is loaded with strain instead of stress. The first problem can be solved exactly without much difficulty. For the second one the solution can be obtained from the solution of the single matrix crack problem analyzed above.

In order to simplify the derivation procedure, it is first assumed that the pressure exerted on the matrix crack surfaces is the only load, as shown in Fig. 3.9a. Using the principle of superposition allows the solution of this problem to be built from the solutions of two other problems, which are shown in Fig. 3.9b-c. The first one is the problem of single matrix cracking, and has been analyzed using the singular integral equation technique. However, the solution of this problem is not that of the original one (Fig. 3.9a), because axial displacements are allowed at the two cross-sections located at a distance L from the matrix crack. In fact the solution can be considered as the solution of the original problem (Fig. 3.9a) but under the action of both crack surface pressure p_2 and the displacements u_z and $-u_z$ applied on its top and bottom edges, respectively. The variation of the displacements across the two sections of the fiber matrix cylinders can be ignored provided the interfacial crack is not very long compared to the spacing $2L$. The solution of the problem shown in Fig. 3.9a can now be obtained by subtracting the solution of the problem shown in Fig. 3.9c from that of the problem depicted in Fig 3.9b. The fiber and matrix of the problem shown in Fig. 3.9c are loaded by uniform tensile strain (u_z/L) and this problem can be solved following the same procedure used to solve

the original problem (Fig 3.9a). Repeatedly using this procedure one can obtain a solution of series form to the original problem (shown in Fig. 3.9a).

Denoting the uniform tensile strain by ε_0, the solution of the problem shown in Fig. 3.8b may be expressed as

$$\sigma_f = C_{f1}\varepsilon_0, \quad \text{and} \tag{3.25a}$$

$$\sigma_m = C_{m1}\varepsilon_0, \tag{3.25b}$$

where σ_f and σ_m are axial stresses in the fiber and matrix, respectively, and C_{f1} and C_{m1} are proportionality constants depending on material constants and the fiber volume fraction. If the geometry depicted in Fig. 3.8b is loaded only by the uniform strain on the fiber and matrix, one can derive the similar solution:

$$\sigma_f = C_{f2}\varepsilon_0, \quad \text{and} \tag{3.26a}$$

$$\sigma_m = C_{m2}\varepsilon_0, \tag{3.26b}$$

where two new proportionality constants are introduced. If the Poisson's ratios for the fiber and matrix are the same, C_{f1} and C_{f2} are approximately equal to E_f, while C_{m1} and C_{m2} are approximately equal to E_m.

For the single matrix crack problem (Fig. 3.9b) under the action of a unit pressure on the matrix crack surfaces (i.e. p_2=1), let us denote the stress intensity factors for the interfacial crack and the magnitude of the average axial displacements at the two cross sections by $\overline{k_1}$, $\overline{k_2}$ and $\overline{u_z}$, respectively. Obviously the average fiber stress at the matrix crack section is $(1-V_f)/V_f$, or V_m/V_f. It has been shown (see Appendix D for details) that

under the action of strain ε_0 the stress intensity factors for the interfacial crack, and the average fiber stress at the matrix crack cross section can be expressed as

$$k_1 = \varepsilon_0 C_{m1} \overline{k_1}(1 - r + r^2 - r^3 + \ldots), \tag{3.27a}$$

$$k_2 = \varepsilon_0 C_{m1} \overline{k_2}(1 - r + r^2 - r^3 + \ldots), \tag{3.27b}$$

$$\overline{\sigma_f} = \varepsilon_0 \left[-\frac{C_{m1} C_{f2}}{C_{m2}} + \left(\frac{V_m C_{m1}}{V_f} + \frac{C_{m1} C_{f2}}{C_{m2}} \right)(1 - r + r^2 - r^3 + \ldots) \right], \tag{3.27c}$$

where $r = C_{m2}\overline{u_z} / L$. Considering the fact that,

$$C_{m2} \cong E_2, \ \overline{u_z} \cong \frac{V_m c_3}{V_f E_1}, \tag{3.28a}$$

and c_3 is the interfacial crack length (measured from the matrix crack plane), one has

$$r \cong \frac{E_m V_m c_3}{E_f V_f L}. \tag{3.28b}$$

For the composite Nicalon/CAS II, E_1=195GPa, E_2=95GPa, and V_f=0.4, one has $r \cong 0.73 c_3/L$. It can be therefore concluded that for $c_2/L<1$ the convergence of the above series is guaranteed.

If an interfacial frictional force exists, its effects can be analyzed separately. For the configuration shown in Fig. 3.10a, which is loaded by an interfacial frictional force τ_s alone, the stress intensity factors and the average fiber stress can be easily derived following the above procedures. For the configuration shown in Fig. 3.10b, when a unit shearing stress is exerted on the interfacial crack surface, $\overline{k_{1s}}$, $\overline{k_{2s}}$ and $\overline{u_{zs}}$ are used to denote the stress intensity factors for the interfacial crack and the magnitude of the displacements at the two cross sections, respectively. The stress intensity factors for the

interfacial crack and the average fiber stress at the matrix crack cross section for the crack configuration shown in Fig. 3.10a can be expressed as (see Appendix D for details)

$$k_1 = \tau_s \left[\overline{k_{1s}} - \frac{\overline{u_{zs}} C_{m2} \overline{k_1}}{L} (1 - r + r^2 - r^3 + \ldots) \right], \tag{3.29a}$$

$$k_2 = \tau_s \left[\overline{k_{2s}} - \frac{\overline{u_{zs}} C_{m2} \overline{k_2}}{L} (1 - r + r^2 - r^3 + \ldots) \right], \tag{3.29b}$$

$$\overline{\sigma_f} = \tau_s \frac{\overline{u_{zs}}}{L} \left(C_{f2} + \frac{V_m C_{m2}}{V_f} \right) (1 - r + r^2 - r^3 + \ldots). \tag{3.29c}$$

Under the action of both applied strain and the friction force, the response of the representative volume shown in Fig. 3.8a can be obtained by combining each equation in Eqs (3.27a-c) with the related one in Eqs (3.29a-c). Adding up the fiber stresses given in Eqs (3.25a), (3.27c) and (3.29c), one obtains the average fiber stress at the matrix crack cross section in Fig 3.8a caused by uniform tension. The effective (or average) stress over the fiber-matrix cylinder for the unit shown in Fig 3.9a can therefore be expressed as

$$\sigma = \overline{\sigma_f} V_f. \tag{3.30}$$

This expression is needed for predicting the tensile behavior of the unit, which is assumed to be the representative behavior of the composite.

From above expressions, it can be seen that, once the analysis of the single matrix crack problem is completed, one can readily analyze the multiple matrix cracking. Since $\overline{u_z}$ and $\overline{u_{zs}}$ depend mainly on the deformation of the fiber in the debonded area, they almost do not change with L, when L is much larger than the interfacial crack length c_3. It is therefore very convenient to investigate the influence of crack spacing, This is

especially advantageous in simulating the stress-strain curves, where the progress of multiple matrix cracking should be considered.

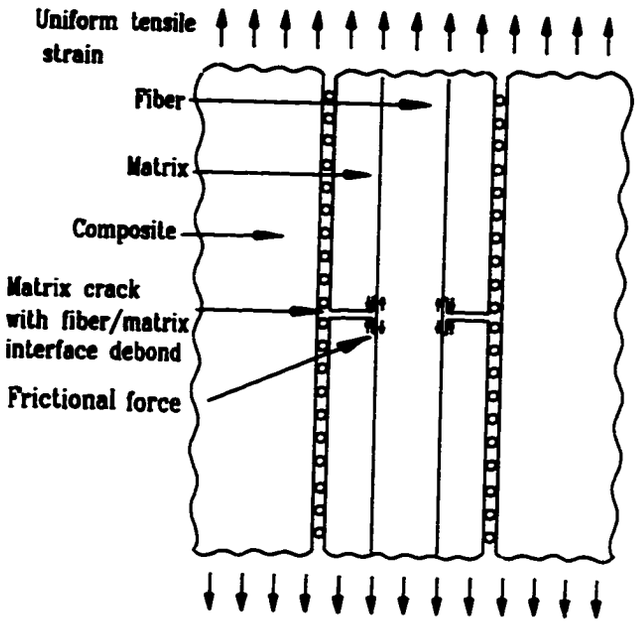

(a)

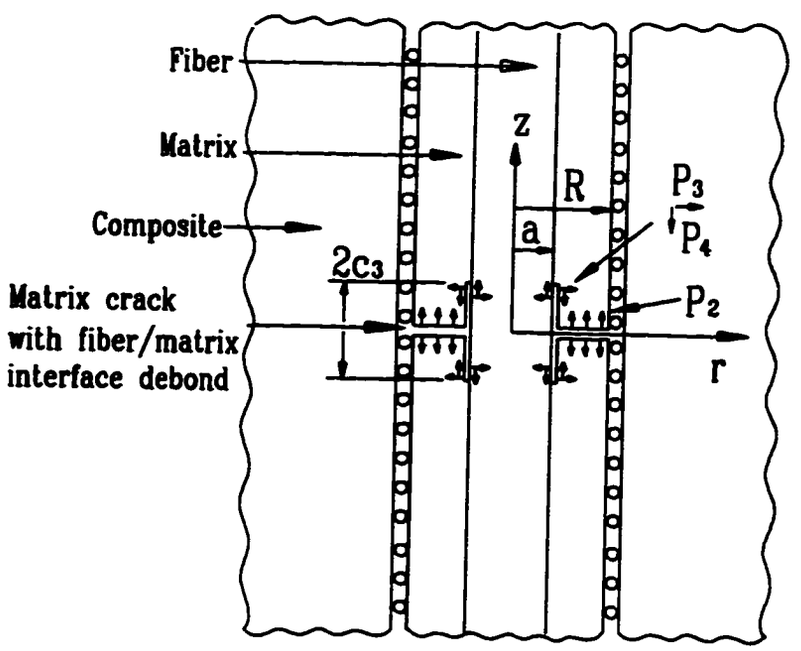

(b)

Fig. 3.7 Schematic of the single matrix crack problem, (a) original problem, (b) related perturbation problem.

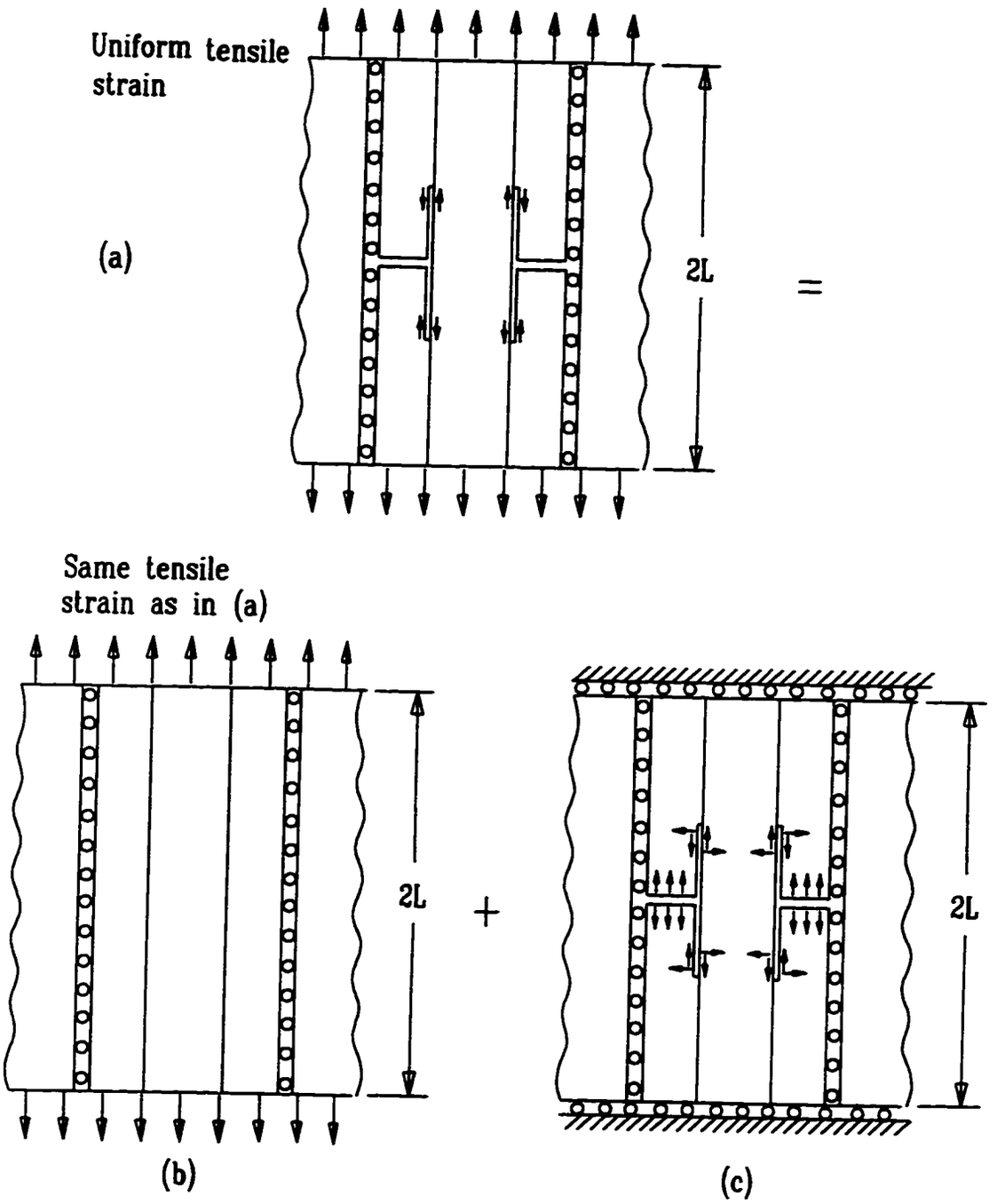

Fig. 3.8 Schematic showing the decomposition of the representative unit into two new problems.

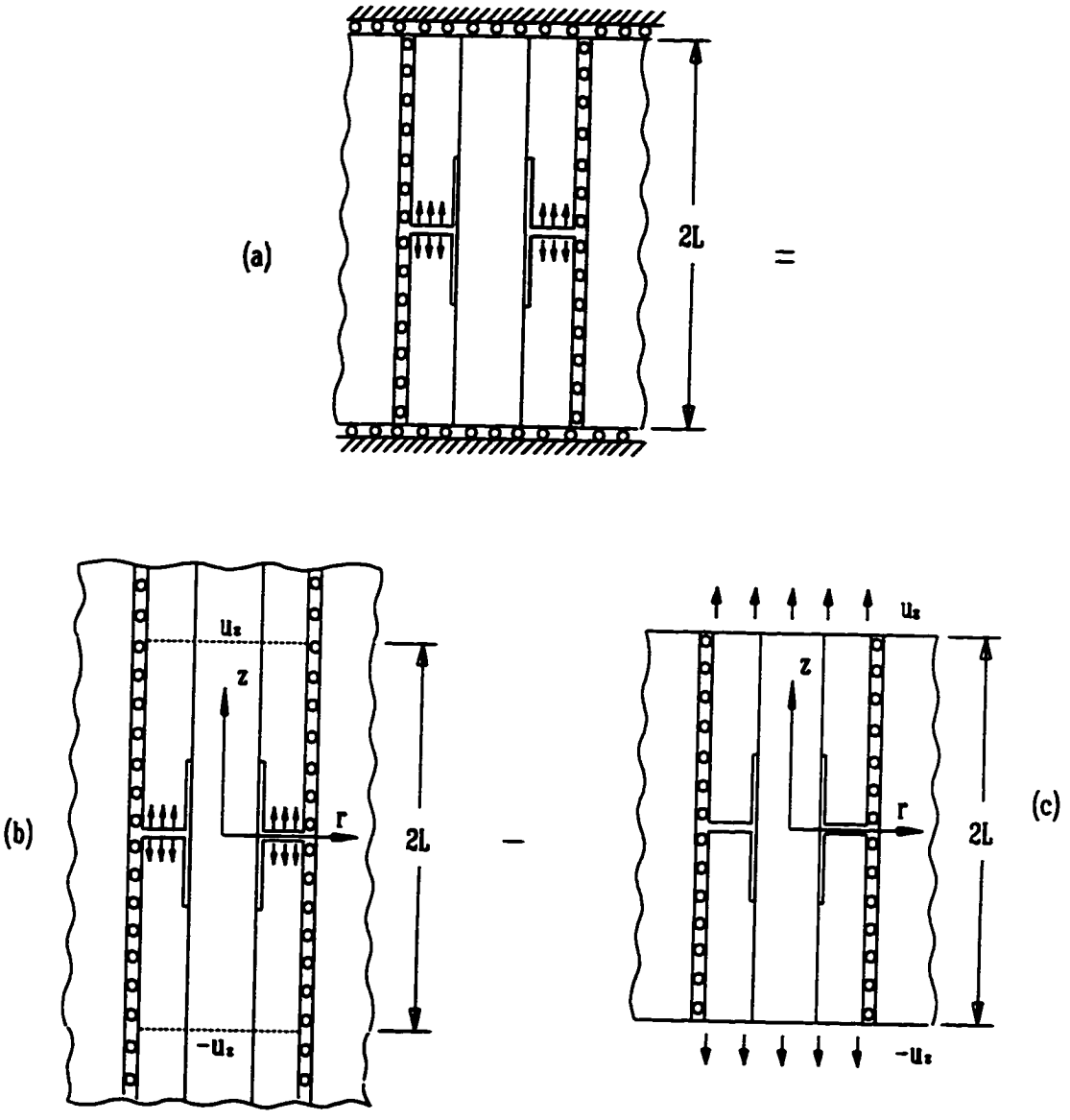

Fig. 3.9 Solution procedure of the problem shown in Fig. 3.8 (c), when the matrix crack pressure is exerted alone.

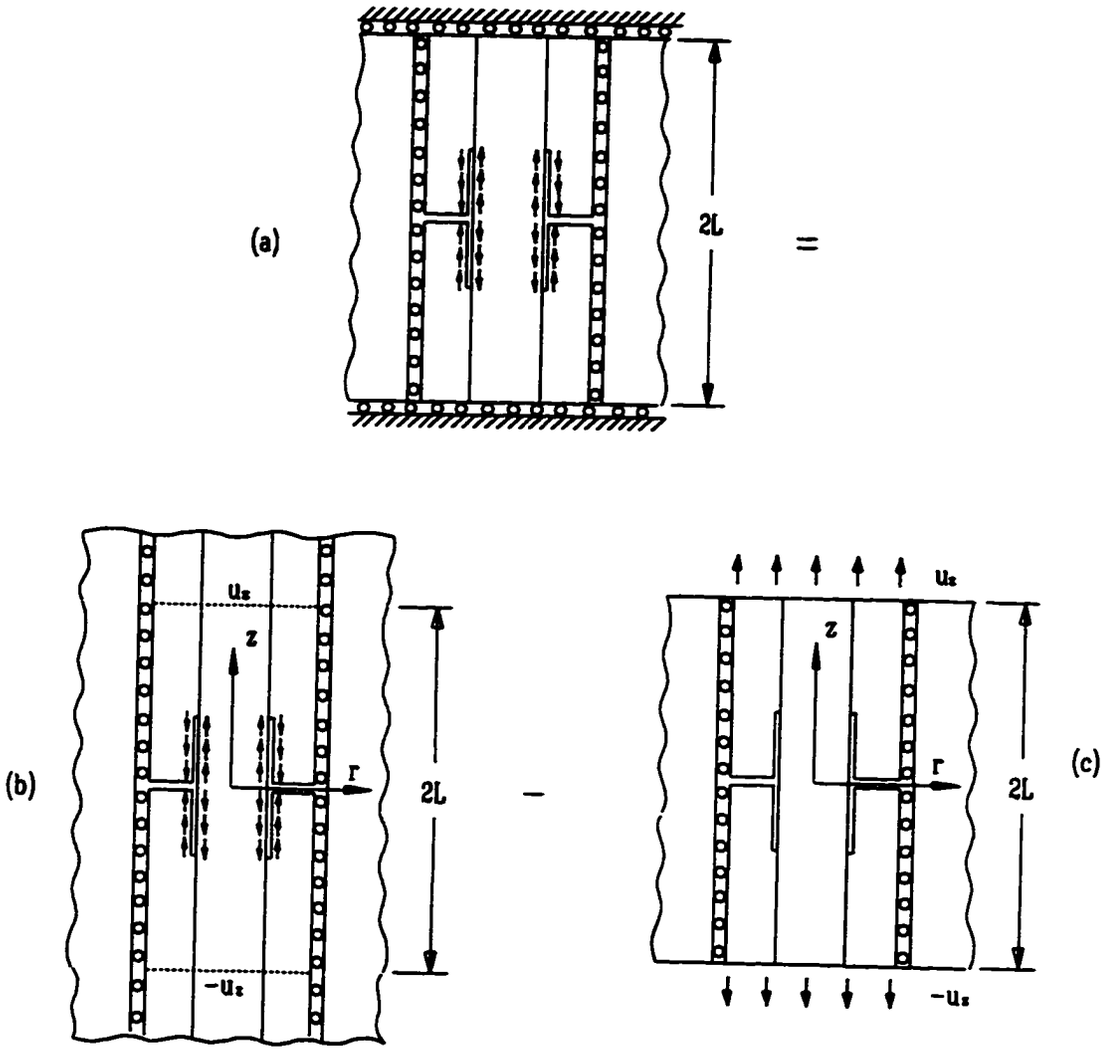

Fig. 3.10 Solution procedure of the problem shown in Fig. 3.8 (c), when the interfacial friction is the only load.

4 Numerical Results and Discussion

4.1 Introduction

It was shown in Chapter 3 that the solution of the multiple matrix cracking problem of the three-cylinder model can be derived from the solution of the single matrix crack problem. The latter is formulated using the singular integral equation technique. In order to solve the singular integral equations accurately and efficiently, the behavior of their kernels must first be analyzed. Because of the involvement of three different materials in the problem, algebraically it will be very lengthy and complicated to derive those kernels in closed form. An alternative procedure used in this research is to first reduce the three-cylinder configuration to a two-cylinder counterpart as shown in Fig. 4.1, which is also an interesting tow-cylinder model, and then derive the kernels of closed-form for this simplified problem. The singular parts of these kernels are applicable to the three-cylinder problem because the singular behaviors of these kernels are determined by the local materials around the crack tips.

Basic numerical procedures were first developed for solving the singular integral equations for the two-cylinder problem and then modified for the three-cylinder problem. Some subroutines available in IMSL [77] were used to evaluate definite integrals, compute Lobatto-Jacobi quadratures, and solve linear algebraic equations. The analysis of the two-cylinder problem and the detailed numerical procedures and schemes are presented in Appendix A. The main results for the analysis of the two-cylinder model have been published [55].

The numerical results are presented in two parts. First the numerical schemes are tested by comparing the current results with those available in the literature. A typical ceramic matrix composite is then analyzed using the three-cylinder model. The results are compared with available experimental data.

4.2 Verification of the numerical schemes

The single interface crack problem, as shown in Fig. 4.2, was studied in [49]. The same problem was reanalyzed here to test the validity of the proposed numerical schemes. Table 4.1 is the comparison of the current results with their adjusted results (The stress intensity factors reported in [49] should be multiplied by a factor of $(\mu_1 + \mu_2\kappa_1)/(\mu_2 + \mu_1\kappa_2)$, which is equal to 1.507 for the given materials). The very fast convergence of this study is observed.

Table 4.1 Stress intensity factors for the case of a single interface crack with λ=25, ν_1=0.2, ν_2=0.35, p_3= constant and $p_4 = 0$. Here n is the number of terms in the series expansion of the dislocations.

	Present Results								**Results in [49]**	
a/c_3	**k_1/p_3c_3**				**k_2/p_3c_3**				**k_1/p_3c_3**	**k_2/p_3c_3**
	n=10	n=15	n=20	n=25	n=10	n=15	n=20	n=25		
0.1	0.21857	0.21987	0.22021	0.22035	0.03261	0.03325	0.03346	0.03356	0.2143	0.03165
1.0	0.65201	0.65226	0.65235	0.65238	0.05095	0.05108	0.05113	0.05116	0.6453	0.05048
10.0	0.96878	0.96882	0.96883	0.96884	0.11650	0.11652	0.11653	0.11653	0.9594	0.1154
∞	1.0000				0.1310				1.0000	0.1310

When both materials for the fiber and the matrix are the same, the single matrix crack problem is reduced to a circular annulus crack in an infinite body, as shown in

Fig. 4.3, which has been studied by many authors. The singular integral equation derived here for the matrix crack is also valid for this case. Table 4.2 is the comparison of the present results with those in the literature with the crack surface pressure p_2 being constant, with good agreement between them being observed. The accuracy can be further enhanced by increasing the number of points in the quadrature formula.

Table 4.2 Stress intensity factors for the circular annulus crack in a homogeneous material, with $\overline{k_b} = \sqrt{2}k_{b_2} / \left(p_2\sqrt{c_2 - b_2}\right)$ and $\overline{k_c} = \sqrt{2}k_{c_2} / \left(p_2\sqrt{c_2 - b_2}\right)$.

b_2/c_2	Present results		Results in [78]		Results in [79]		Results in [80]	
	$\overline{k_b}$	$\overline{k_c}$	$\overline{k_b}$	$\overline{k_c}$	$\overline{k_b}$	$\overline{k_c}$	$\overline{k_b}$	$\overline{k_c}$
0.1	1.949	0.911	1.972	0.909	1.972	0.909	1.972	0.909
0.2	1.492	0.920	1.502	0.918	1.503	0.917	1.502	0.918
0.3	1.305	0.928	1.310	0.927	1.316	0.923	1.310	0.927
0.4	1.201	0.938	1.204	0.936	1.224	0.927	1.204	0.936
0.5	1.135	0.947	1.137	0.946	1.187	0.926	1.137	0.946
0.6	1.090	0.957	1.091	0.956	1.204	0.918	1.089	0.957
0.7	1.057	0.967	1.058	0.966	1.296	0.902	1.057	0.967
0.8	1.033	0.977	1.033	0.977	1.531	0.875	1.032	0.978
0.9	1.014	0.988	1.015	0.988	2.180	0.854	1.014	0.988
0.99	1.001	0.999	1.001	0.998	7.232	1.420	1.001	0.999

When the materials of the fiber and the matrix are different, as shown in Fig. 4.4, the stress intensity factors for a single matrix crack loaded by constant crack surface pressure are available in [50]. Although the integral equation in this study for the matrix crack is the same as that in [50], the results do not match exactly. This may be due to different numerical approaches being used, particularly for the case of a crack tip terminating at the interface. When the inner matrix crack tip terminates at the interface, for material combinations of λ=1/7 and λ=7 (i.e., ν_1=ν_2=0.25), β_1 takes the values

-0.71488 and -0.33040, respectively. In Figs. 4.5 and 4.6 the numerical results of this study are compared with those found in [50]. Although some error may result from reproducing the curves reported in [50], the results agree very well except for some values in Fig. 4.6(a) when a/c_2 approaches to zero. That is the case of crack terminating at the interface.

4.3 Damage analysis of brittle matrix composites

4.3.1 Introduction

This section presents damage analysis of brittle matrix composites using the three-cylinder model. The same assumption used by Weitsman and Zhu [19] is also adopted for multiple matrix cracking. That is the evolution of matrix cracking is governed by an energy criterion, and new cracks form at the mid-spans of existing cracks. In addition to multiple matrix cracking, interfacial debonding is also considered as a possible damage mode. The prediction is compared with the experimental results for a composite Nicalon/CAS II, which has the following material properties: E_f = 195 GPa, ν_f = 0.28, E_m = 95 GPa, ν_m = 0.28, and V_f = 0.4. The radius of the fiber is a = 7.5 μm.

In addition to the above properties, the matrix fracture energy γ_m, the interfacial debonding energy γ_{db}, and the interfacial friction τ_s are also required for the stress-strain simulation. Although many models and techniques have been developed for the measurement of these properties, it is still difficult to measure them precisely. For CMCs, the reported typical ranges are 5–50 J.m^{-2} for γ_m, 0–5 J.m^{-2} for γ_{db}, and 1–200 MPa for

τ_s [81]. For composite SiC/CAS, the reported ranges are 0–1 $J.m^{-2}$ for $\gamma_{db.}$ and 15–25 MPa for τ_s [82]. For composite Nicalon/CAS II, however, no reliable data are available in literature. The actual magnitudes of these parameters for a CMC will depend on both the manufacturing process of the composite and the method of measurements. The varied ranges for these parameters used in this study are 5–15 $J.m^{-2}$ for γ_m, 0–0.5 $J.m^{-2}$ for γ_{db}, and 0–15 MPa for τ_s. Latter numerical results will show that the choice of these ranges is reasonable.

4.3.2 Analysis of interfacial debonding associated with a single matrix crack

After a transverse matrix crack forms with fiber bridging, the fiber-matrix interface will debond further with increasing loading. The model shown in Fig. 3.5 can be used to analyze the behavior of debonding. The model can also be reduced to a two-cylinder model with a transverse matrix crack by changing the material constants of the composite cylinder. Reducing the moduli of the third composite cylinder to zero, one obtains a two-cylinder model with the free outer surface; while raising the moduli of the composite cylinder to infinity, one obtains a two-cylinder model with the radial displacement of the outer surface of the matrix cylinder being constrained. Two-cylinder models are commonly used with shear lag analysis.

For the two-cylinder model with a free outer surface, as the interfacial crack length approaches to infinity, one can easily derive the strain energy release rate:

$$G_0 = \frac{p_2^2 a V_m}{4 E_f V_f}\left(\frac{E_f}{E_m} + \frac{V_m}{V_f}\right) \quad , \tag{4.1}$$

where p_2 is the pressure exerted on the matrix crack surfaces. In what follows, G_0 is used to normalize the strain energy release rates.

Figures 4.7-10 show the normalized stress intensity factors and strain energy release rates (see Eq. (3.1) and (A.44) for the definition of the strain energy release rate) for three different boundary conditions imposed on the outer surface of the matrix cylinder. Here the material used is the Nicalon/CAS II composite with 0.4 fiber volume fraction, and interfacial friction is not considered. It can be seen from Figs 4.7-9 that, the properties of the third composite cylinder do not have much influence on mode II stress intensity factor, but have significant effect on mode I. When the outer surface of the matrix cylinder is free, the opening mode stress intensity factor always exists. When the outer surface of the matrix cylinder is constrained in the radial direction, the interface crack is closed provided the crack length is larger than about $0.2a$. Figure 4.10 shows the strain energy release rates for three different conditions. It indicates that in each case the strain energy release rate approaches a limit value as the crack length increases.

Figure 4.11 shows the effect of the fiber volume fraction on stress intensity factors. Reducing the fiber volume fraction results in increase in the stress intensity factors. The effect on mode II is especially significant. This fact may imply easier debonding wherever fibers are sparsely distributed within the composite.

4.3.3 Analysis of interfacial debonding associated with multiple matrix cracking

Following the initial matrix cracking, another possible damage mode is multiple matrix cracking. In reality the interfacial debonding and multiple matrix cracking may

progress alternatively. The multiple matrix cracking will result in a dropping in the stress intensity factors or the strain energy release rate for the interfacial crack. With the evolution of multiple matrix cracking, therefore, the interfacial debonding will slow down.

Figure 4.12 shows the effect of the multiple matrix cracking on the strain energy release rate. Here the matrix crack spacing $2L$ is used to specify the state of the multiple matrix cracking. It can be seen that for a given matrix crack spacing, the longer the interfacial crack length, the more the release rate drops with decrease in the matrix crack spacing. For a large spacing $2L = 200a$, obvious dropping in the release rate can still be observed.

4.3.4 Simulation of damage process in unidirectional ceramic-matrix composites

The multiple matrix-cracking model (Fig. 3.5), combined with the two criteria derived in Chapter 3 , was used to predict the behavior of the composite with micro-damage. The micro damage mechanisms considered are multiple matrix cracking, interfacial debonding, and frictional sliding at debonded interfacial areas. Three variables, the matrix crack spacing $2L$, the interface debond length c_3, and the relative fiber-matrix interfacial slide are used to measure the micro-damage mechanisms in the composite. The progression of the damage is controlled by loading, the matrix fracture energy γ_m, the interfacial debond energy γ_{db}, and the interfacial friction stress τ_s. The effective behavior of the composite is modeled by that of the fiber-matrix cylinder shown in Fig. 3.5. The onset of matrix cracking can be modeled by multiple matrix cracking with very large

spacing L and very short interfacial debonding. Then as the loading continues, the multiple matrix cracking may evolve with the matrix crack spacing being reduced, or the interfacial debonding may propagate further, depending on the stage of the loading and the material properties of the constituents of the composite. In this study, the simulated results are compared with experimental data obtained at CCNY [9, 10].

As the first attempt to simulate the nonlinear behavior of the composite, the simulation starts form the loading stage when matrix crack saturation has been reached. Based on the experimental stress-strain curves in Fig. 4.13 and the SEM micro-graphs shown in Fig. 3.4, a stress of 240 MPa is chosen as the corresponding effective stress, and a spacing $20a$ as the corresponding matrix crack spacing. Using the stress and the spacing a critical interfacial strain energy release rate can be estimated, which is then used to control the propagation of the interfacial crack. Fig. 4.13 shows the predicted results using three different conditions imposed on the outer surface of the matrix cylinder, with interfacial friction being ignored. It is observed that without interfacial friction, the interfacial debonding can occur under an almost constant effective stress.

Fig. 4.14 shows the results with interfacial friction being considered. In this case and also in what follows, only the unreduced three-cylinder model is used. From the four curves corresponding to four different values of the interfacial friction (τ_s=0, 5, 10, 15 MPa), one can see the effect of the friction on the behavior of the composite.

If one considers interfacial debonding and multiple matrix cracking together, it is unnecessary to estimate any parameters from tensile test results, except that parameters γ_m, τ_s, and γ_{db} should be given. Because no reliable data are available in literature for

these parameters, various values within the reported ranges are therefore selected to investigate their influence on the behavior of the composite. The spacing $L = 640a$ is chosen as the initial half matrix crack spacing and $L = 10a$ as the saturated one for convenience. Actually choosing different initial values for this parameter does not have much influence on the predicted results, provided it is large enough. The final saturated spacing can be predicted in this model if the tensile stress, with the energy balance criterion derived in Chapter 3, is used to govern the fracture of the matrix.

Figure 4.15 shows a typical predicted stress-strain curve in comparison with experimental results, while the following figures are the results of detailed parametric study.

First of all, from Fig. 4.15 one can easily identify four phases. The first phase, which corresponds to the initial linear portion of the stress-strain curves, is from the beginning of the loading to the initiation of the first matrix cracking. The composite remains undamaged during this phase, and thus the modulus of the composite is almost equal to that calculated from the rule-of-mixtures.

The second phase begins with the initiation of the first matrix cracking and ends with the start of multiple matrix cracking. During this phase, the dominant damage is interfacial debonding, although multiple matrix cracking may also occur. The departure of the predicted curve from linearity is not obvious.

The third phase is dominated by multiple matrix cracking, although interfacial debonding is also possible. This phase is characterized by highly nonlinear behavior of the composite. As multiple matrix cracking progresses, the axial stress in the matrix is released rapidly, with very slow increase and some fluctuations in the effective stress

being observed, which is analog to yielding in metals. This fact can explain the plateaus observed on tensile test curves. This phase ends with the matrix crack saturation.

The last phase begins with the occurrence of matrix crack saturation. In this phase high matrix crack density and long interfacial debonding prevent matrix stresses from reaching high values as the loading continues, and most of the load is therefore sustained by fibers. The interfacial debonding, however, can still occur. The effective stress increases more rapidly with strain in this stage than in the third phase, which is similar to strain hardening in metals. With further increase in the loading, the stress-strain relationship will approach to the limiting line with slope $E_f V_f$ if fiber break does not occur. Comparing the influences of the various damage mechanisms on the behavior of the composite, it can be conclude that the multiple matrix cracking is the main energy dissipation mechanism.

Figures 4.16-18 show the effects on the behavior of the composite of the matrix fracture energy and the interfacial debonding energy, with interfacial friction τ_s=10 MPa. From Fig. 4.16 to 4.18, three different values of the matrix fracture energy: γ_m=5, 10, and 15 J/m^2 were chosen, respectively. In each of the figures three different simulation curves are presented corresponding to three interfacial debond energies: γ_{db}= 0.1, 0.2, and 0.5 J/m^2. All three figures show that, with increase in the interfacial debonding energy the predicted curves shift upward, which means enhancement in stress for multiple matrix cracking. This phenomenon may be explained as follows: When the interfacial debond energy increases, interfacial debonding process will be slowed down. Since, as the

calculations have shown, the energy available for multiple matrix cracking decreases with a decrease in the interfacial debond length, multiple matrix cracking thus occurs at higher strain levels and higher stresses. It can be observed that both the stress level and duration of multiple matrix cracking increase with increasing debond energy.

One can also see the influence of the matrix surface energy on the behavior of the composite, if one picks a curve from Fig. 4.16 and compare it with its two counterparts from Fig.4.17 and Fig. 4.18. Increasing its value also shifts the curve upward, because high matrix surface energy can delay the occurrence of multiple matrix cracking. The curve corresponding to the debond energy of 0.1 J/m^2 and the matrix surface energy of 15 J/m^2 in Fig. 4.18 indicates that, if the interfacial bond is too weak and the interfacial friction is too small, multiple matrix cracking, the desirable mechanism for a tough composite, may not occur.

In Figures 4.19-21, a greater interfacial frictional stress of 15 MPa was used; and for interfacial debond and matrix surface energies the same values as used in Fig. 4.16-18 were selected, except for Fig. 4.21 in which a debond energy of 0.05 J/m^2 was used to replace the energy of 0.5 J/m^2. This is because for the given friction, the interfacial debond energy of 0.5 J/m^2 is too high to model the test results. By comparing each predicted curve in Fig. 4.19 with the corresponding one in Fig. 4.16, one can observe upward shifting of the whole curve and the more rapid increase in the stress with the strain in the fourth phase, which is the result of higher interfacial frictional force. The higher interfacial friction therefore will result in a stronger composite without its other effects being considered. Figs. 4.20-21 are comparable to Figs. 4.17-18, respectively. In

Fig. 4.21, obvious influence of the interfacial debond energy on the predictions can also bee seen even though a very small range of it was used with the highest matrix surface energy and interfacial sliding stress.

In summary, the three-cylinder model was used successfully to predict the response of a ceramic-matrix composite. The model shows its great ability to capture the damage progression, including fiber-matrix interface debonding, and multiple matrix cracking, with minimum reliance on empirical data. The predicted stress-strain curves are closely correlated to the micromechanical parameters and, for some combinations of these parameters, are in very good agreement with the experimental test results. It has been verified that multiple matrix cracking is the main energy dissipation mechanism, which is responsible for the occurrence of plateaus in tensile test curves. The parametric study indicates clearly the influence of the micromechanical parameters on the macro-behavior of the composite, and provides us an insight into the relationships between the properties of the constituents of the composite and the bulk behavior of the composite.

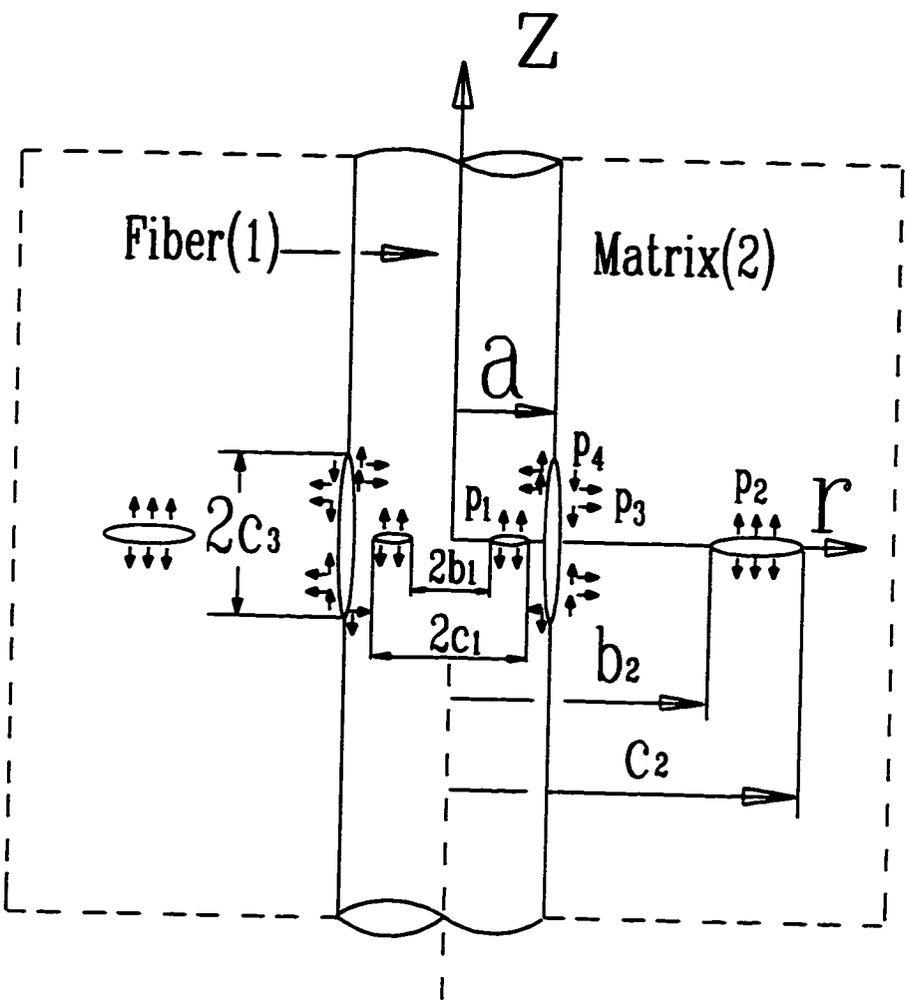

Fig. 4.1 Geometry of the two-cylinder problem

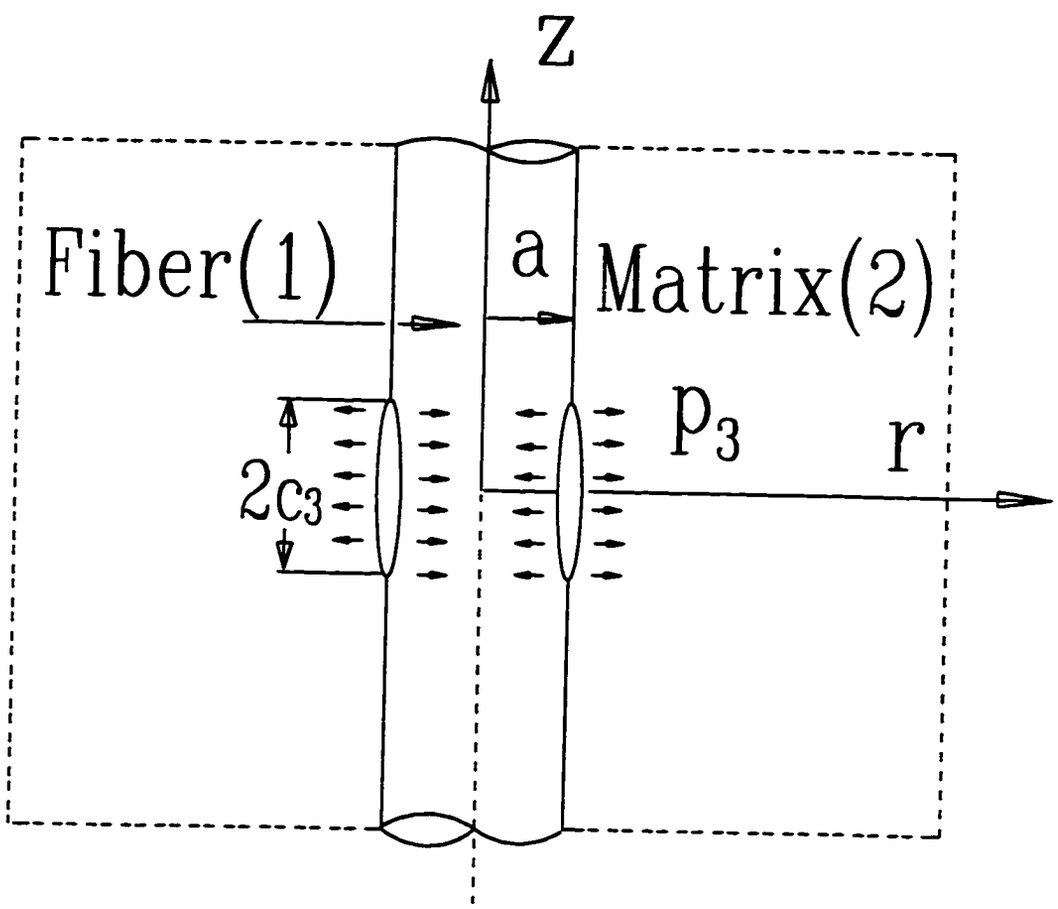

Fig. 4.2 Schematic of the single interfacial crack problem.

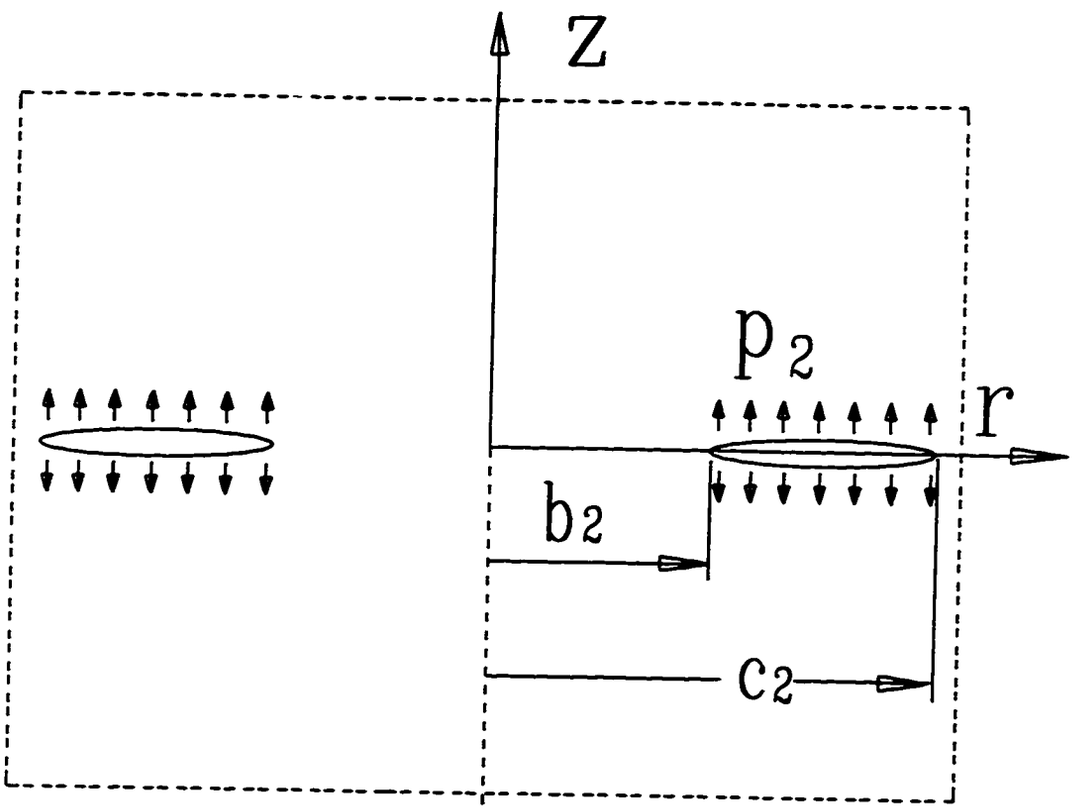

Fig. 4.3 Schematic of the problem with a circular annulus crack in an infinite body.

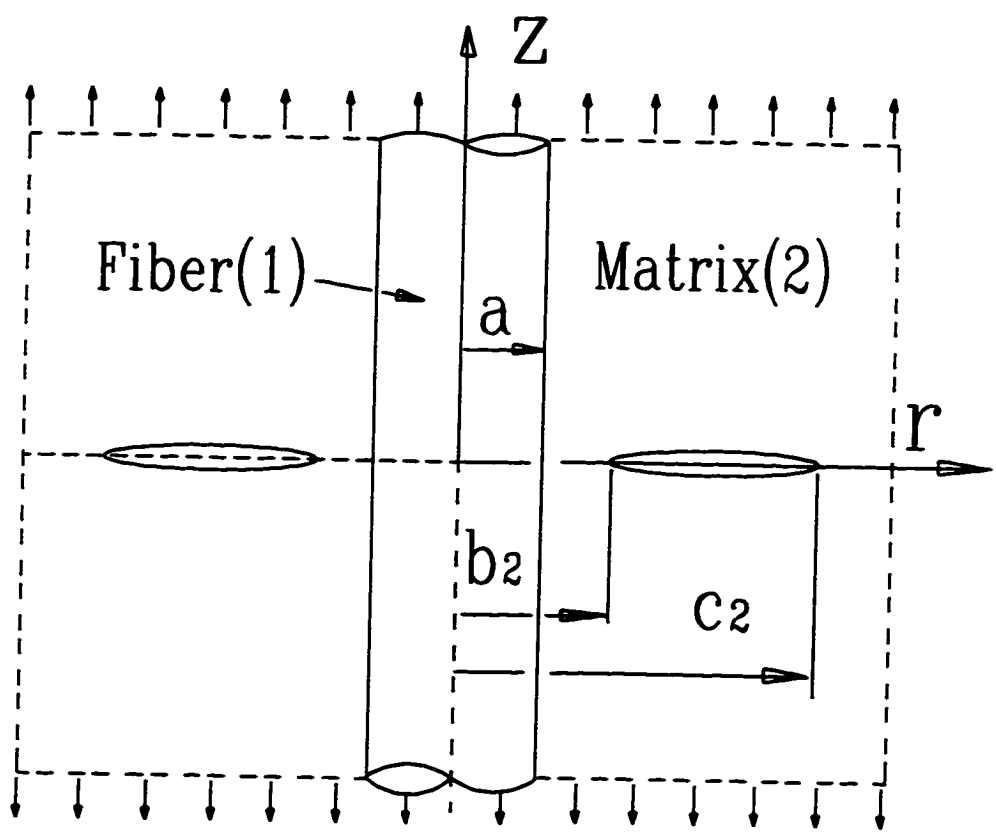

Fig. 4.4 Schematic of the two-cylinder problem with a single matrix crack.

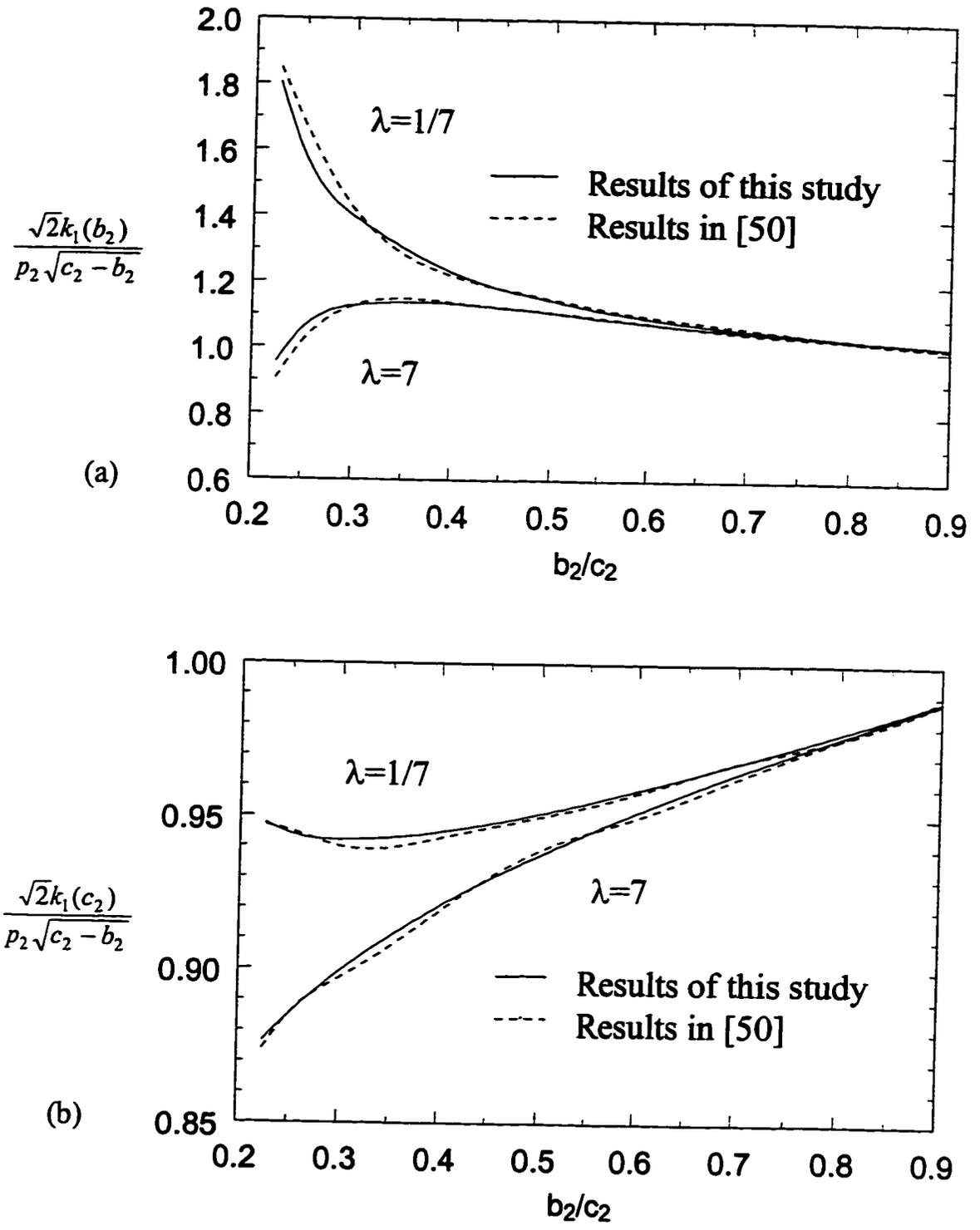

Fig. 4.5 Stress intensity factors for the matrix crack when the inner crack tip is away from the interface, $a/c_2 = 0.2$, $\nu_1 = \nu_2 = 0.25$, $\lambda = \mu_1/\mu_2$.

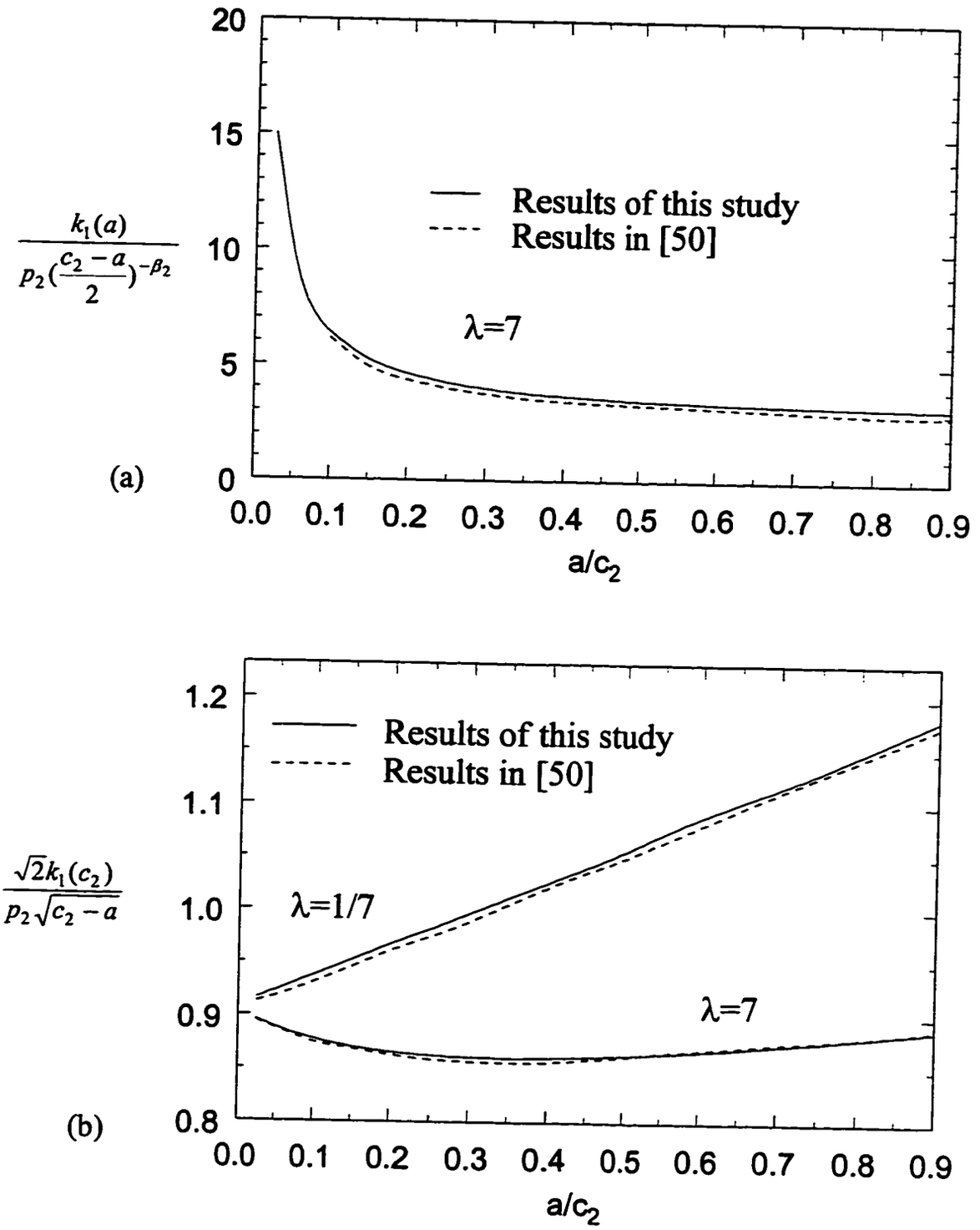

Fig. 4.6 Stress intensity factors for the matrix crack when the inner crack tip terminates at the interface, $\nu_1=\nu_2=0.25$, $\lambda = \mu_1/\mu_2$.

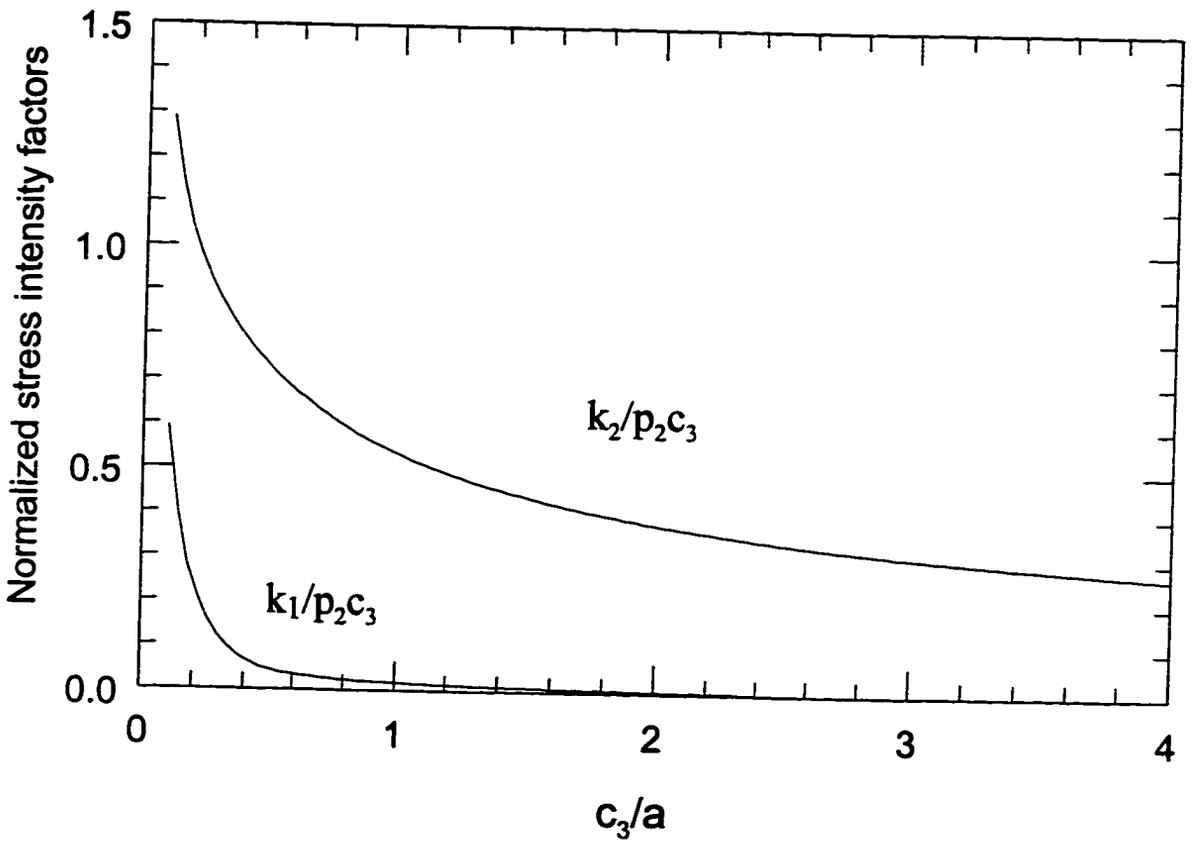

Fig. 4.7 Stress intensity factors for interfacial crack as functions of the crack length, when the composite cylinder exists, $V_f = 0.4$.

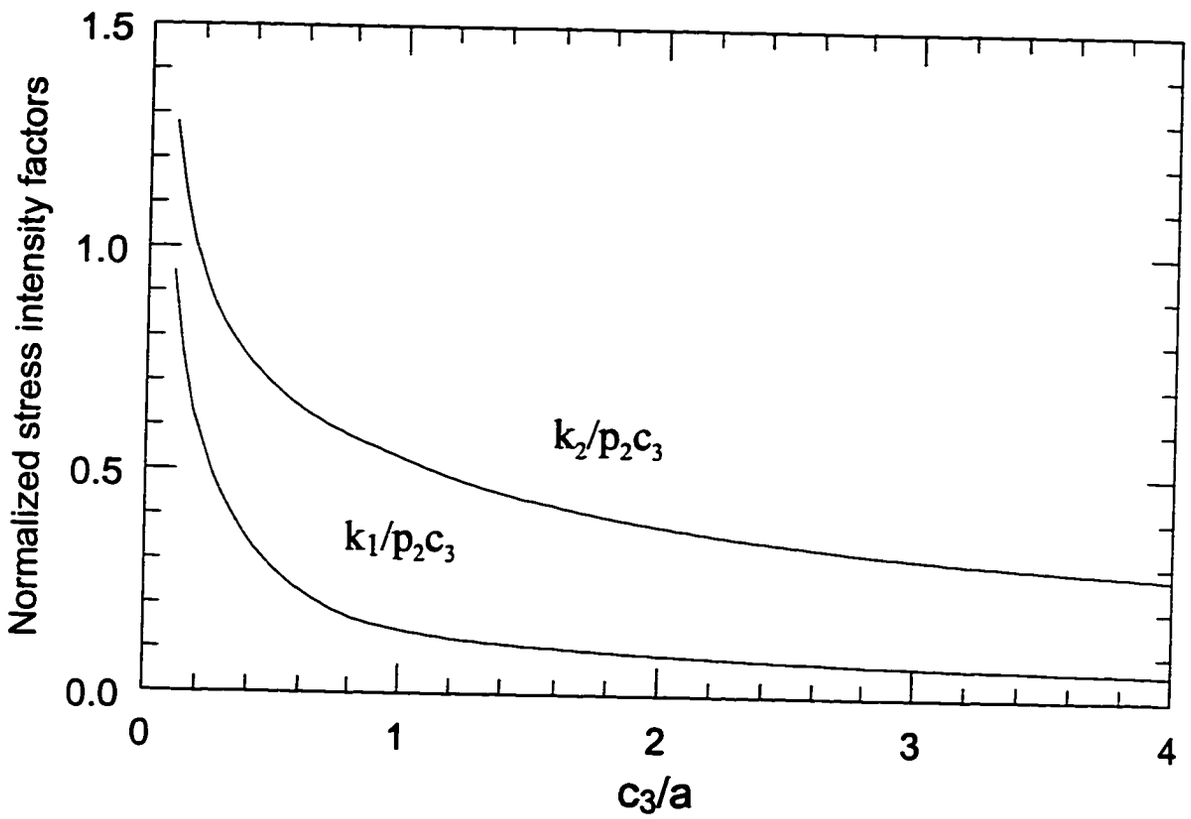

Fig. 4.8 Stress intensity factors for interfacial crack as functions of the crack length, when the outer surface of the matrix cylinder is free, $V_f = 0.4$.

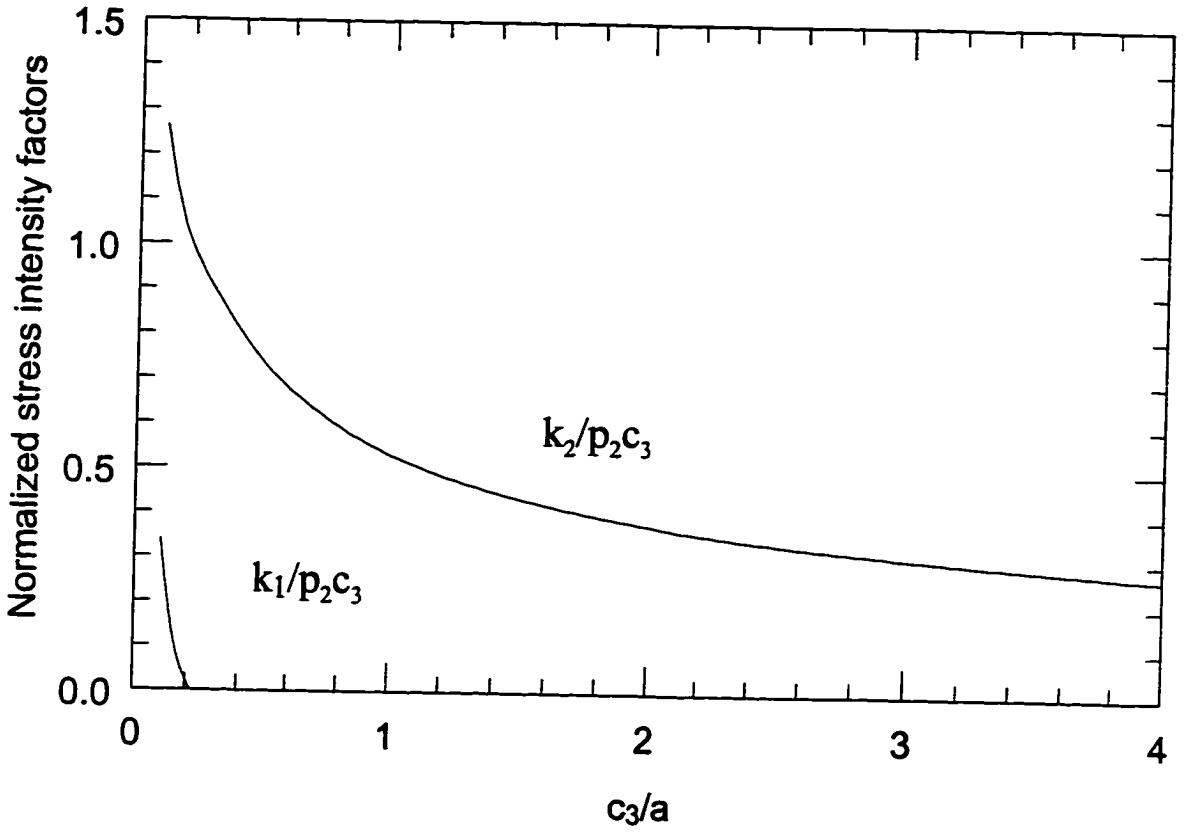

Fig. 4.9 Stress intensity factors for interfacial crack as functions of the crack length, when the radial displacement of the outer surface of the matrix cylinder is prohibited, $V_f = 0.4$.

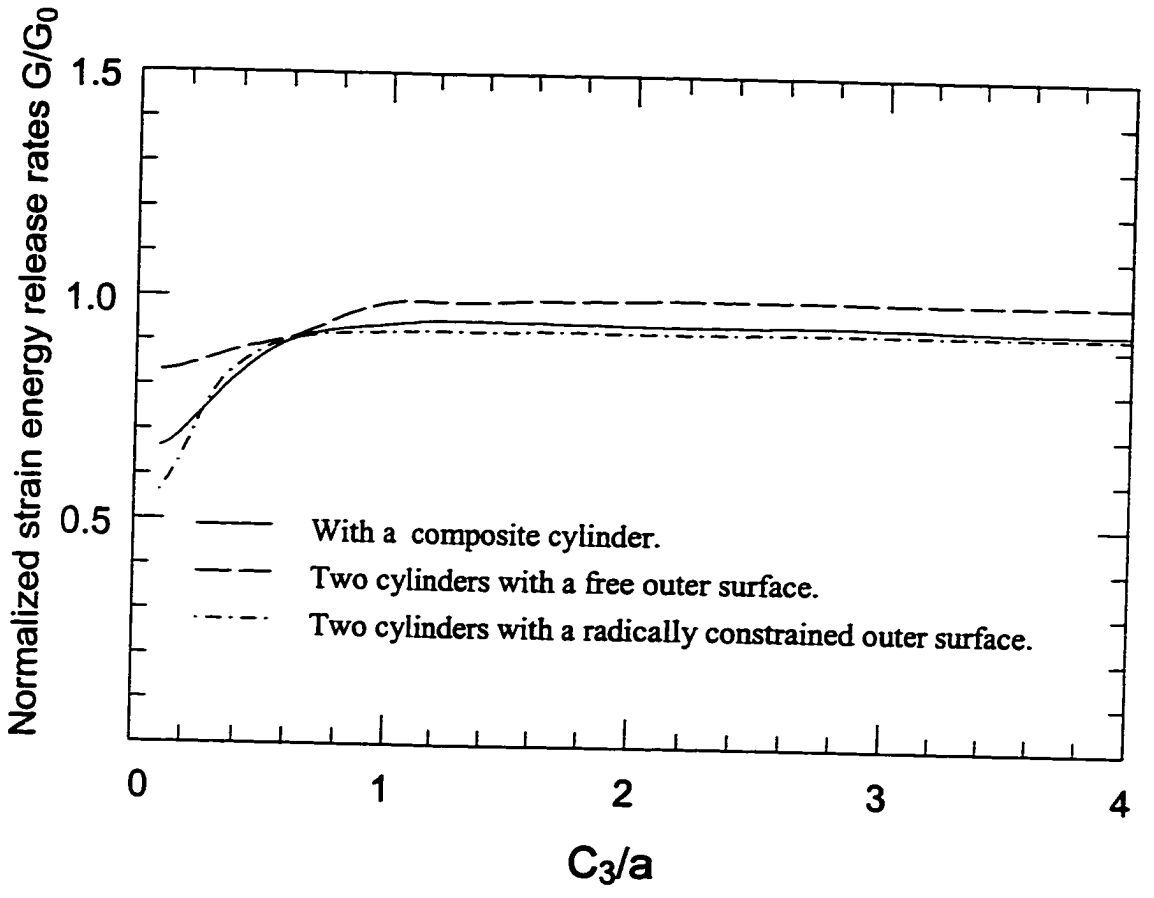

Fig. 4.10 Strain energy release rates as functions of of the crack length, with different boundary conditions being imposed on the outer surface of the matrix cylinder, $V_f = 0.4$.

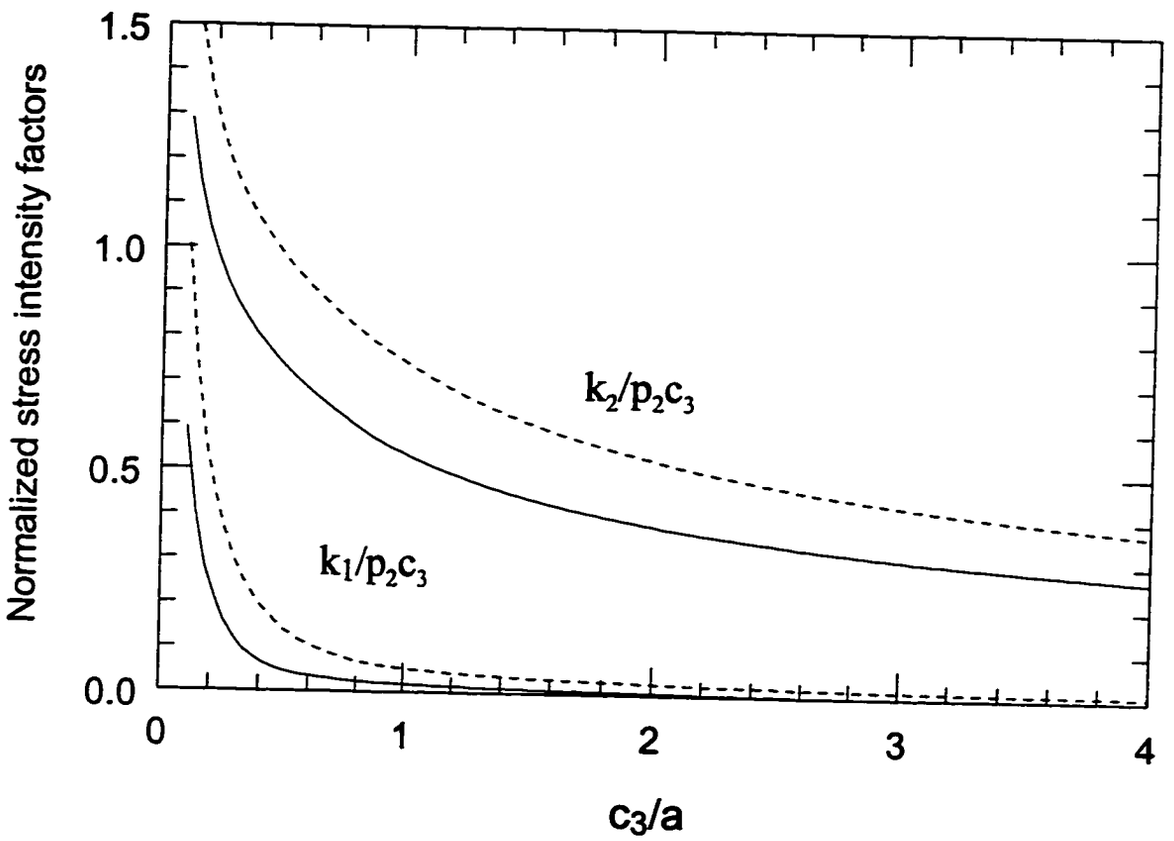

Fig. 4.11 Effect of fiber volume fraction on stress intensity factors for interfacial crack, when the composite cylinder exists, solid lines: $V_f = 0.4$; dashed lines: $V_f = 0.3$.

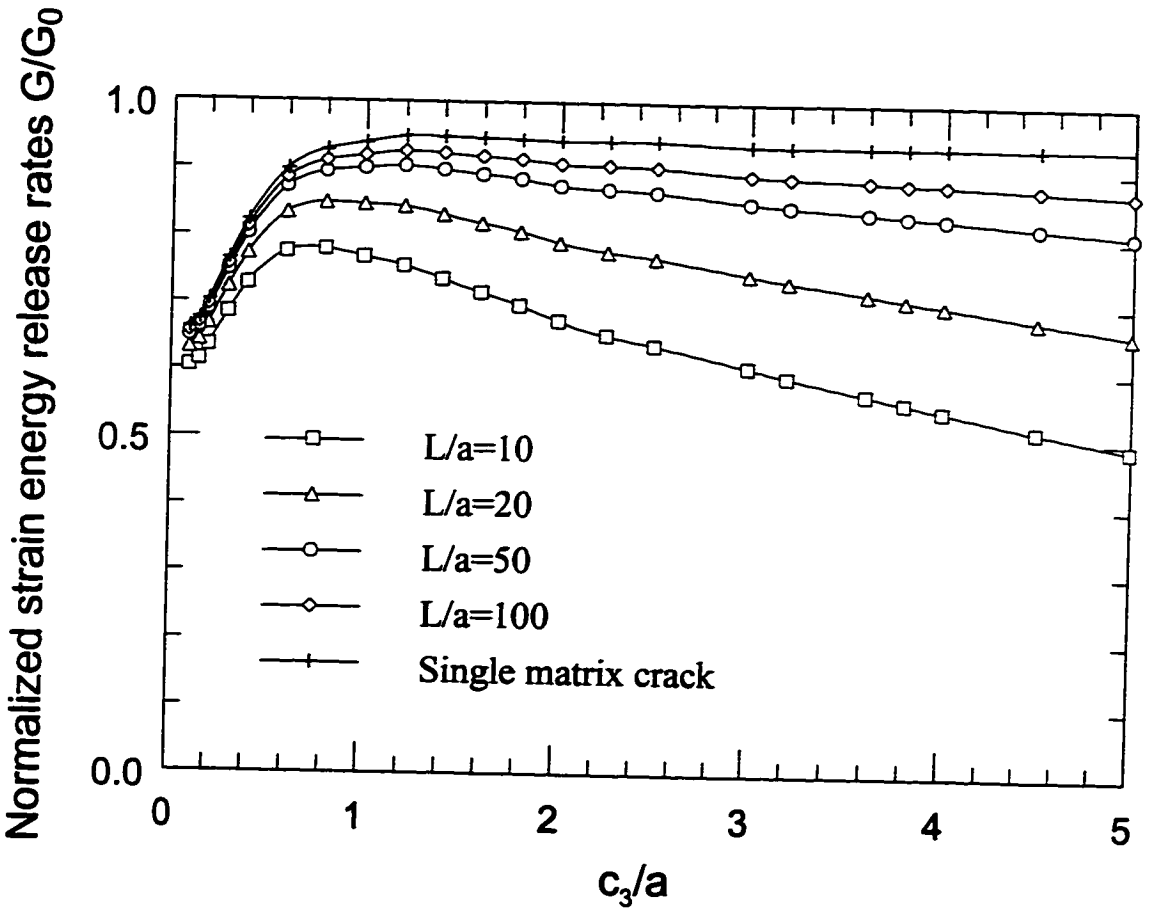

Fig. 4.12 Effect of matrix crack spacing on strain energy release rate for three-cylinder model, $V_f = 0.4$.

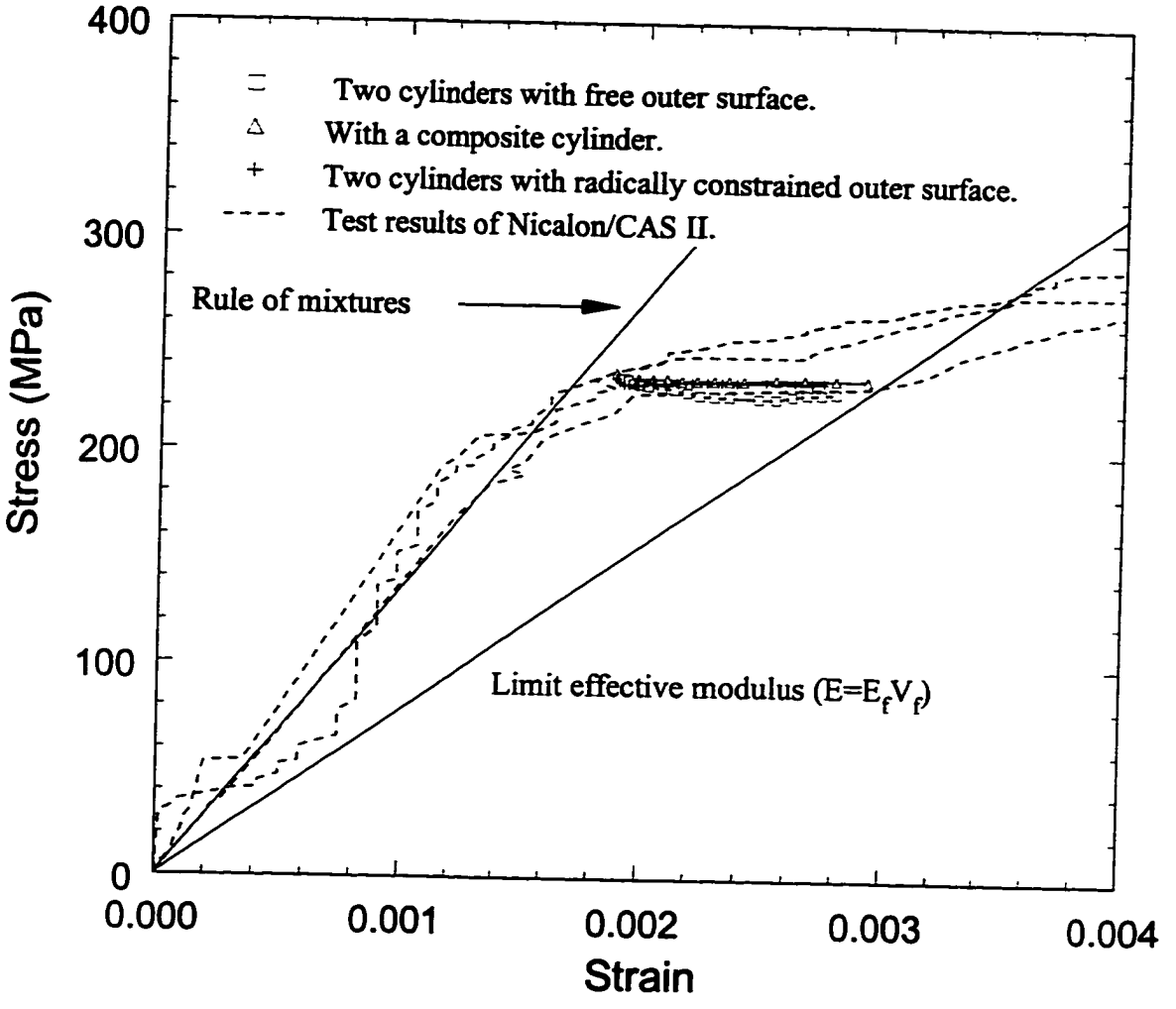

Fig. 4.13 Simple simulation of stress-strain curves considering only interface debonding without friction.

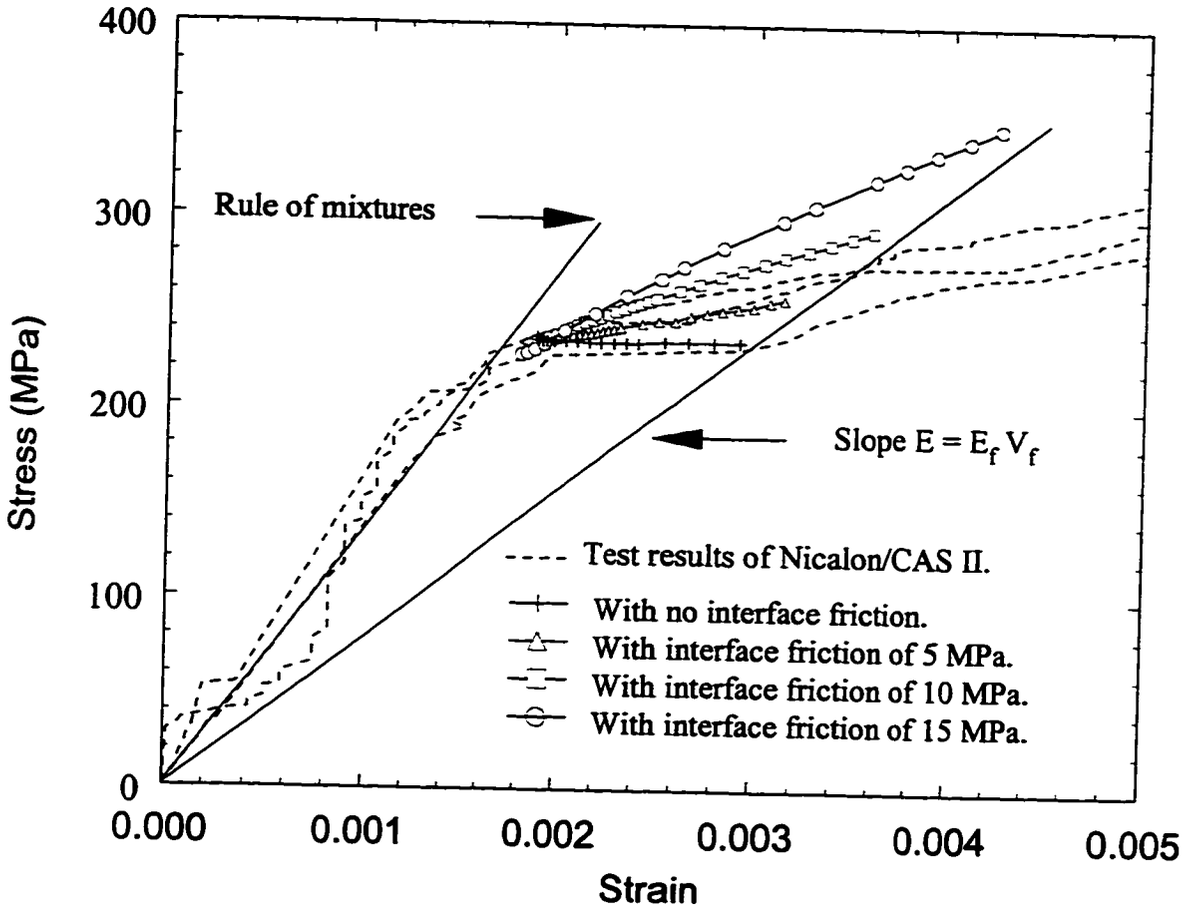

Fig. 4.14 Simple simulation of test results from considering only interface debonding with friction.

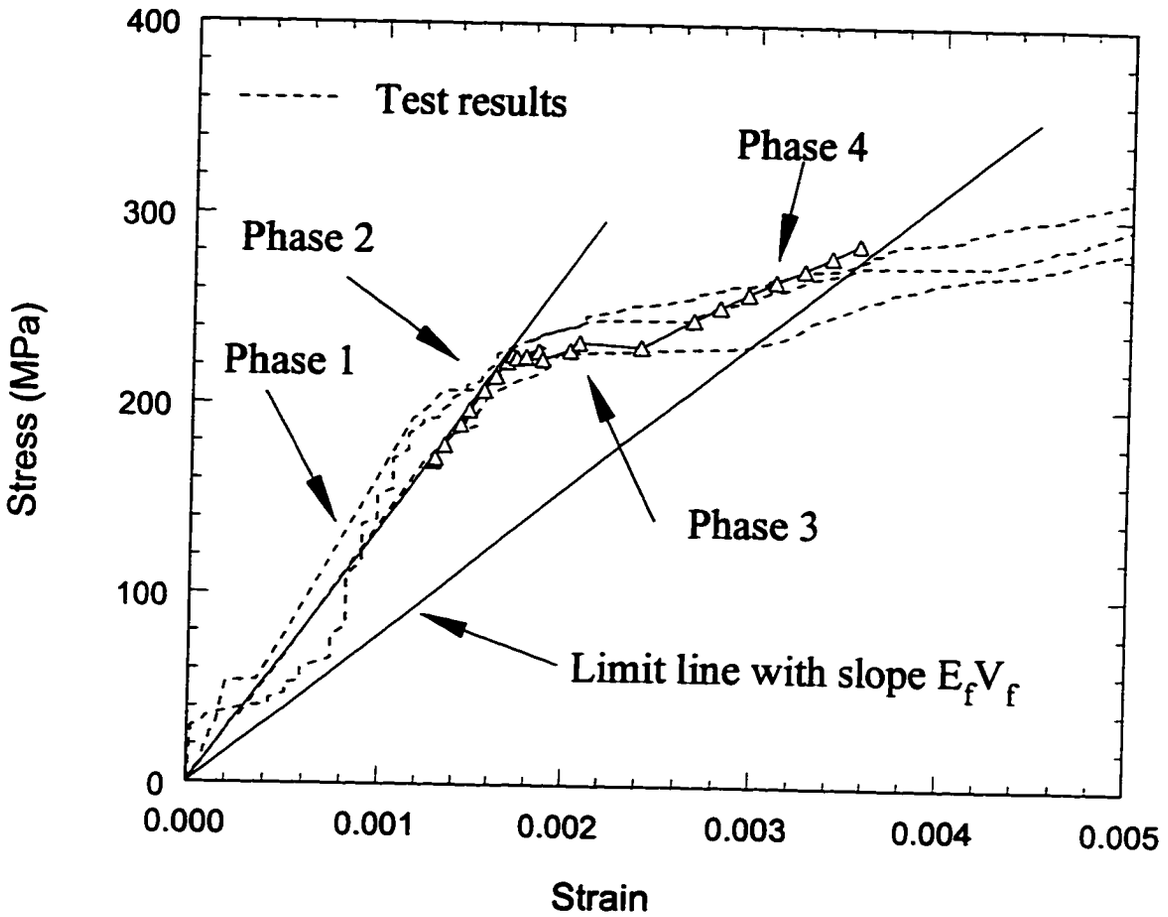

Fig. 4.15 A typical predicted curve compared with test results for Nicalon/CAS II at room temperature, with $V_f = 0.4$. Parameters used in the prediction are: $\tau_s = 10$ MPa, $\gamma_m = 5$ J/m^2, $\gamma_{db} = 0.5$ J/m^2.

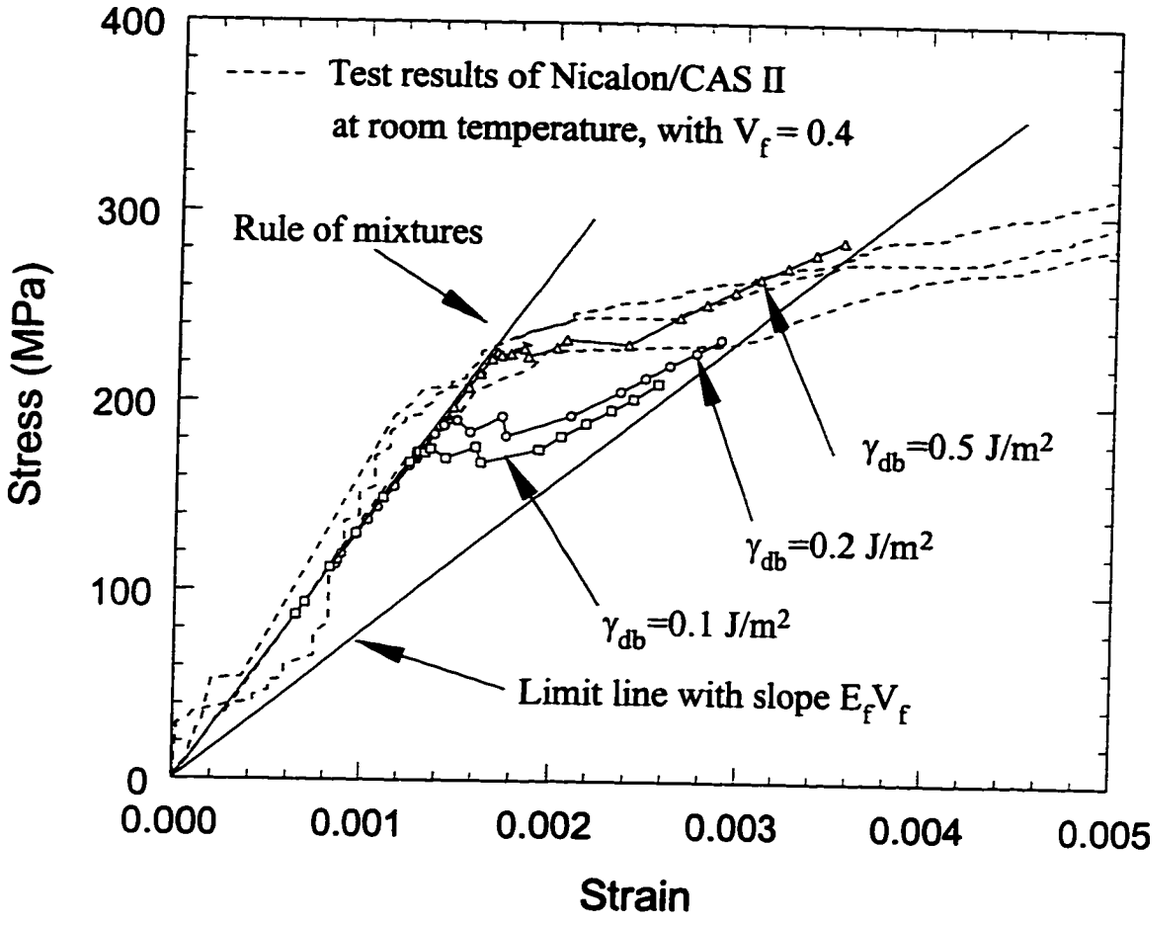

Fig. 4.16 Effect of critical debond energy on the prediction, with τ_s = 10 MPa, γ_m = 5 J/m^2.

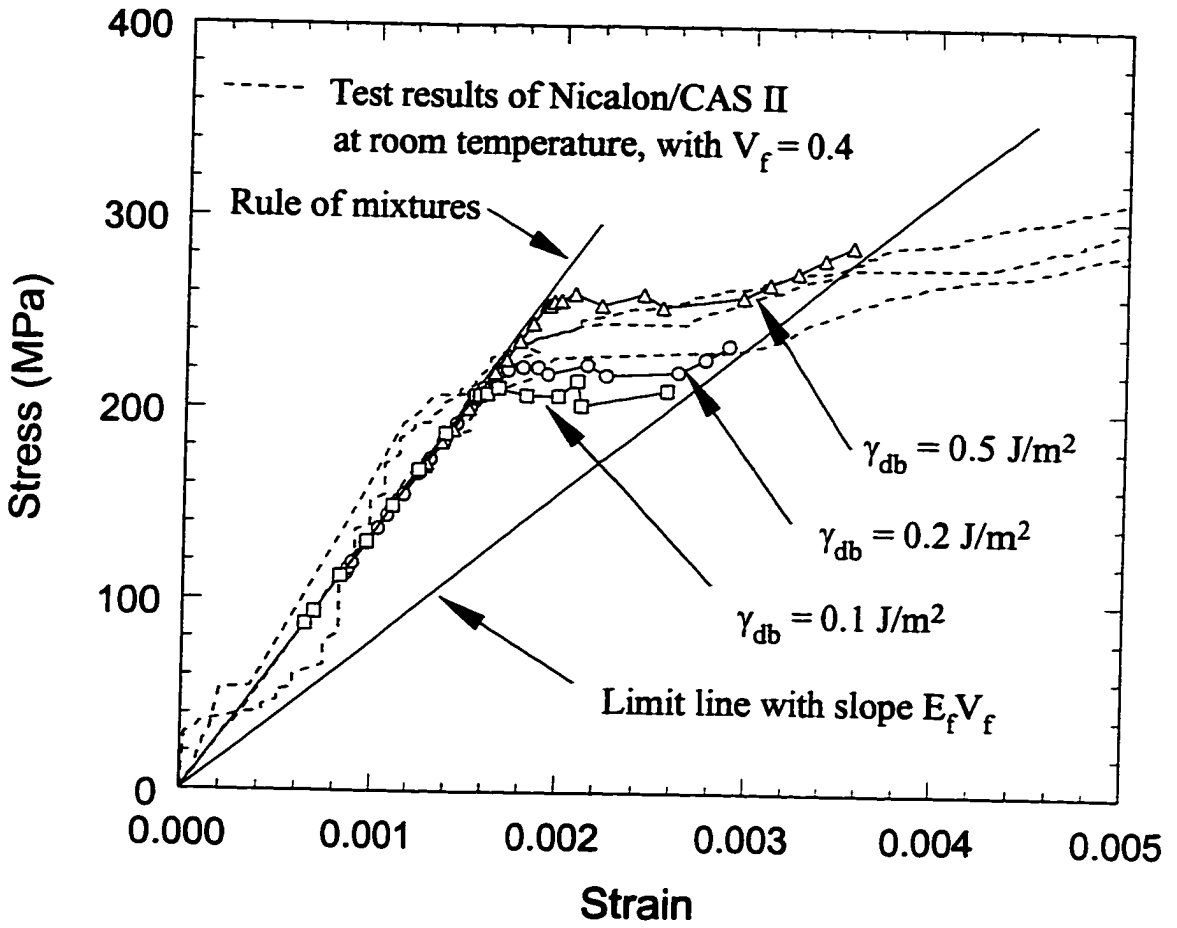

Fig. 4.17 Effect of critical debond energy on the prediction, with $\tau_s = 10$ MPa, $\gamma_m = 10$ J/m^2.

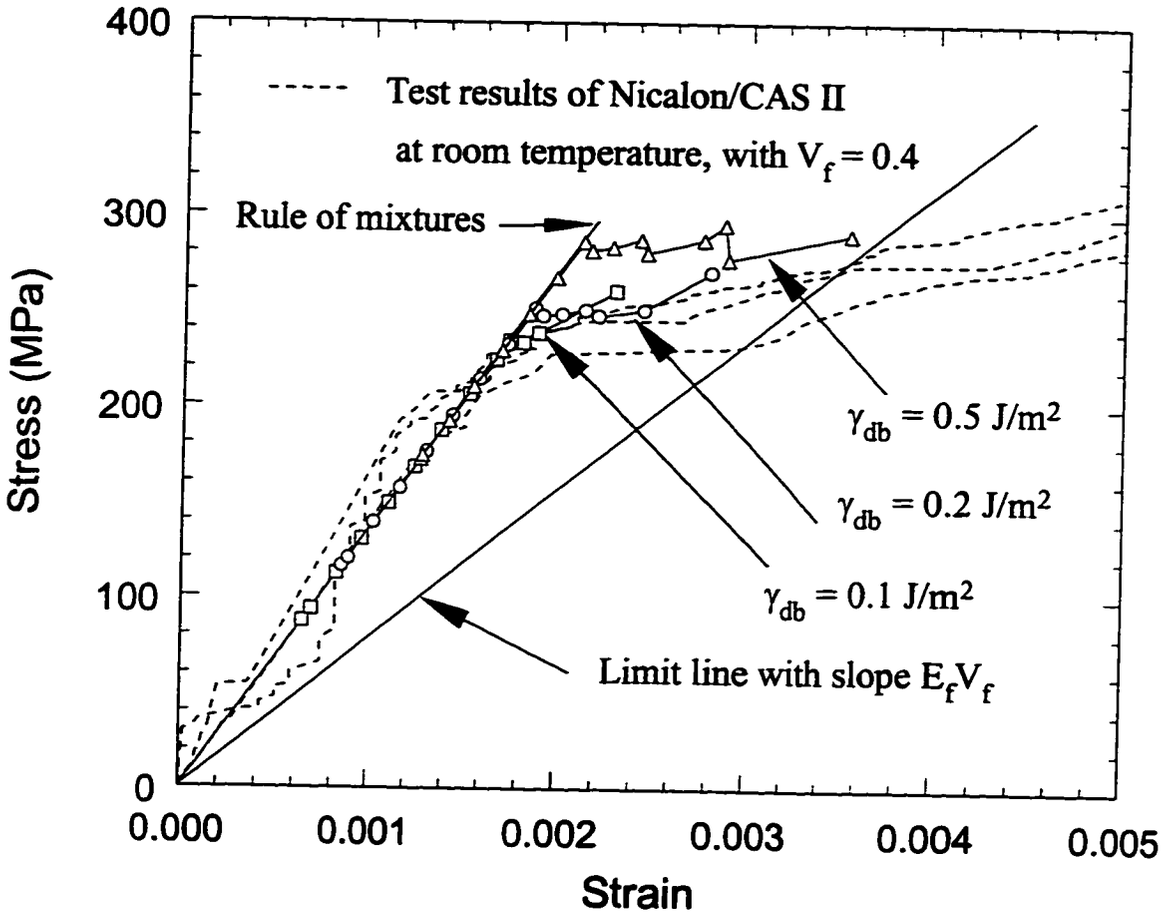

Fig. 4.18 Effect of critical debond energy on the prediction, with $\tau_s = 10$ MPa, $\gamma_m = 15$ J/m^2.

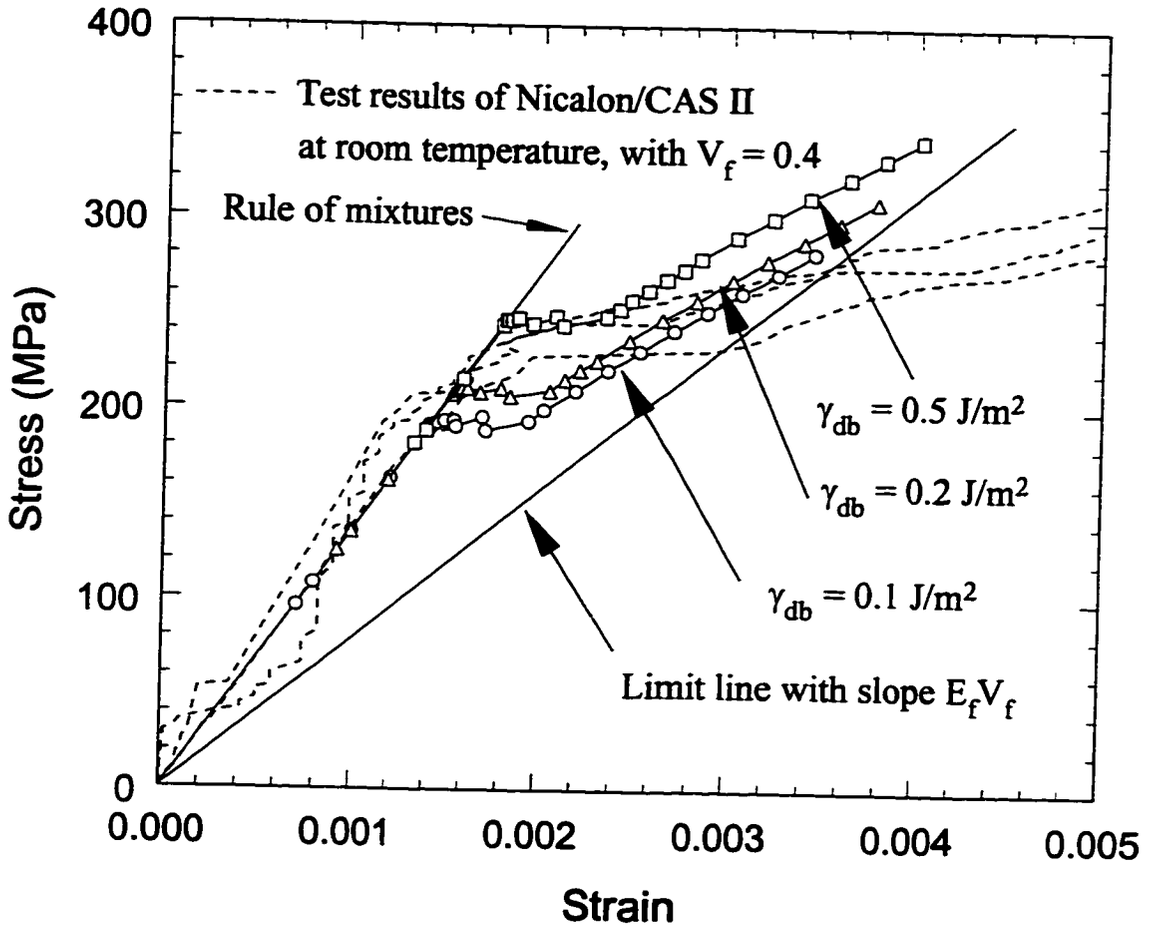

Fig. 4.19 Effect of critical debond energy on the prediction, with $\tau_s = 15$ MPa, $\gamma_m = 5$ J/m^2.

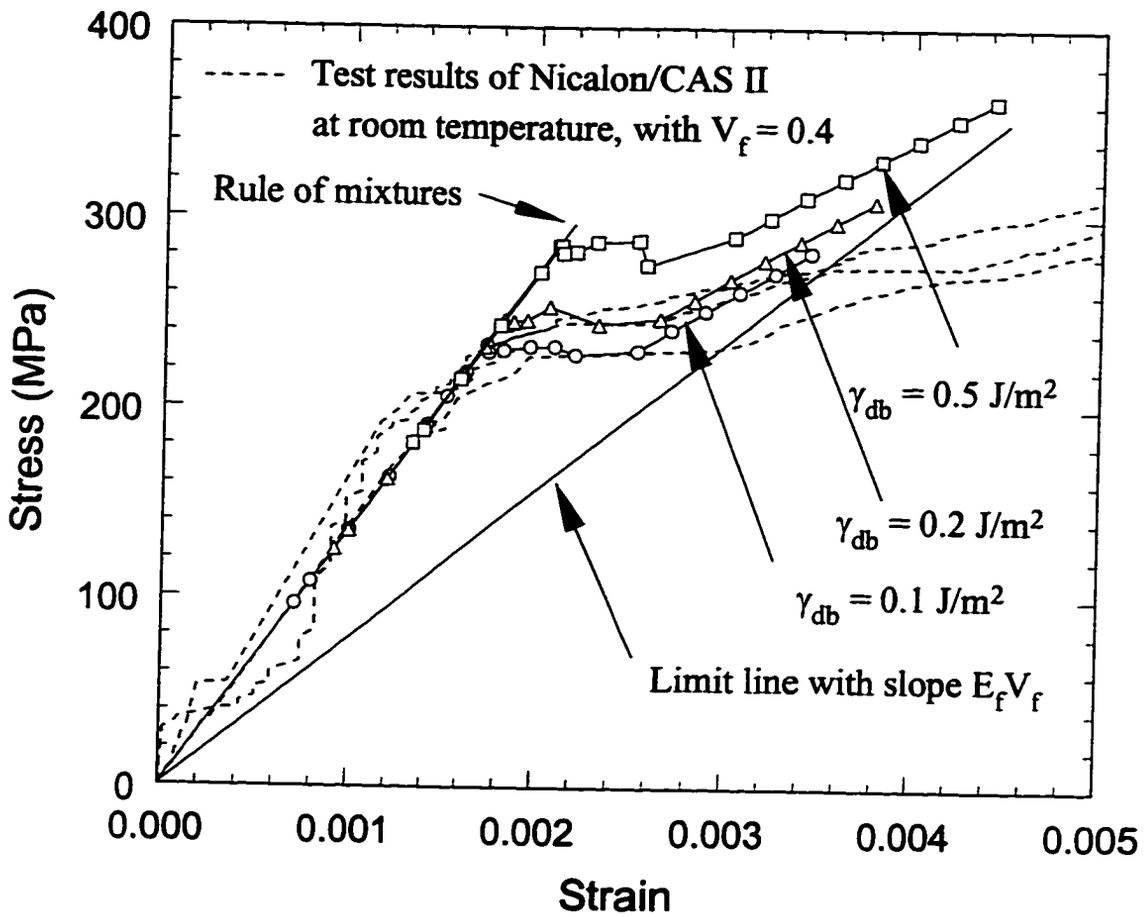

Fig. 4.20 Effect of critical debond energy on the prediction, with $\tau_s = 15$ MPa, $\gamma_m = 10$ J/m^2.

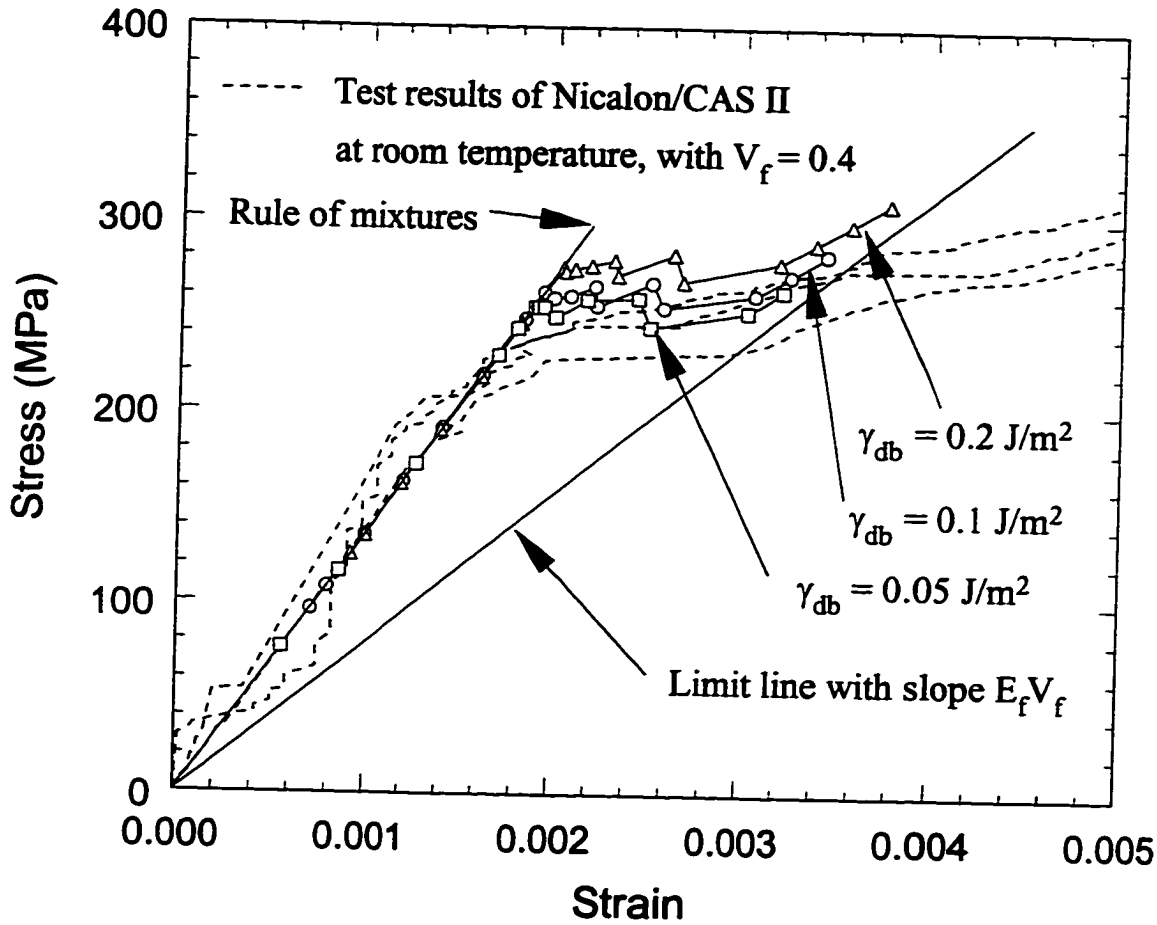

Fig. 4.21 Effect of critical debond energy on the prediction, with $\tau_s = 15$ MPa, $\gamma_m = 15$ J/m^2.

5 *Summary and Conclusions*

The three-cylinder model of fiber-reinforced composites developed in this study is one of the most realistic cylinder-like models ever proposed. Introducing the third composite cylinder to the conventional two-cylinder model makes the model capable of considering the influence of the rest of the composite on the representative unit. Another important feature of the model is the rigorous formulation using the singular integral equation technique, and the accurate interfacial debonding analysis using fracture mechanics. Therefore, the detailed microfracture analysis in this study is a contribution to the understanding of microdamage in composites.

In simulating the damage development in composites, this study differs from previous similar studies in that it considered not only the matrix fracture energy and the interfacial sliding stress, but also another important micromechanical parameter, the interfacial debonding energy. Compared to the matrix fracture energy, the interfacial debonding energy is usually very small. This study, however, has shown that the initiation of multiple matrix cracking is very sensitive to this parameter; and therefore, it is inappropriate to ignore its effect on the behavior of ceramic matrix composites. Since the stress level of multiple matrix cracking is the first concern for engineering applications, it is of importance to reveal the effect of the interfacial debond energy on this level while the matrix fracture energy and interfacial sliding stress are given. The stress-strain curves predicted by this model are in very good agreement with the

experimental test results, and clearly revealed the correlation between the behavior of the composite and its micromechanical parameters.

In general, this study indicates that a matrix with a higher matrix fracture energy can yield a composite with a higher stress for multiple matrix cracking and a wider plateau. Such a composite is desirable, because a higher matrix cracking stress implies a higher allowable stress for engineering applications and a wider plateau indicates the higher toughness of the composites. Nevertheless, the desirable improvements can only be achieved with the appropriately designed fiber-matrix interface. If the interface is too weak (i.e., both interfacial debond energy and interfacial sliding stress are too small), the desirable multiple matrix cracking may not happen.

The study also shows that the stronger interface (that is, the one with higher interfacial debond energy and interfacial sliding stress), can improve the behavior of the composite in the same way. The interface, of course, should be weak enough to prevent fibers from being broken. In literature, it seems that only the importance of the weak interface has been emphasized, while the importance of the relatively stronger interface has been ignored. Before the saturation of matrix cracks, the two interfacial parameters seem to have similar effects on the behavior of the composite, but the interface debond energy plays a key role in the initiation of interfacial debonding.

Much work can be done to refine and expand this study. First, thermal effects and residual stresses can be considered in the model for modeling the high-temperature behavior of composites. For the interfacial sliding stress, other types of friction may be used. Second, fiber stresses can be investigated and fiber break may be considered as another damage mode to extend the usefulness of the model. Third, the detailed effects of

the micromechanical parameters on the behavior of the composite can further be investigated by simulating the loading and unloading behaviors of composites. The simulation with tensile loading and unloading experimental results may be used to identify the three parameters conveniently.

Appendix A

Analysis of the Two-Cylinder Problem and Development of Numerical Procedures

A.1 Formulation of the problem

As shown in Fig. 4.1 the geometry of the problem consists of a fiber embedded in an infinite matrix with cracks present in the fiber, within the matrix and along the fiber/matrix interface. Both the fiber and matrix are isotropic, homogeneous and linearly elastic. In what follows, the superscripts and subscripts 1 and 2 refer to the fiber and matrix, respectively, unless stated otherwise. The composite cylinder is loaded by a uniform longitudinal tensile strain ε_0 applied at $z = \pm\infty$, but it can also be loaded by a thermal load, or both, provided the axisymmetric condition is preserved. The solution of the problem can be obtained by the superposition of two problems. The first is that of uncracked geometry under given loading, which can be solved without much difficulty. The latter, also called the perturbation problem, is the cracked geometry loaded on the crack surfaces by the negative of stresses obtained from the solution of the uncracked problem and interfacial frictional stress (if it exists). Since the singular part will be obtained only from the second solution, only the perturbation problem will be considered here.

A.1.1 Displacement and stress fields

For an isotropic body, the axisymmetric displacement and stress fields can be expressed in terms of Love's stress function Φ as follows [83, 84]:

$$u_r(r,z) = -\frac{1}{2\mu}\frac{\partial^2\Phi}{\partial r\partial z}, \tag{A.1a}$$

$$u_z(r,z) = \frac{1}{2\mu}\left[2(1-\nu)\nabla^2\Phi - \frac{\partial^2\Phi}{\partial z^2}\right], \tag{A.1b}$$

$$\sigma_{rr}(r,z) = \frac{1}{\partial z}\left[\nu\nabla^2\Phi - \frac{\partial^2\Phi}{\partial r^2}\right], \tag{A.1c}$$

$$\sigma_{\theta\theta}(r,z) = \frac{1}{\partial z}\left[\nu\nabla^2\Phi - \frac{\partial^2\Phi}{r\partial r}\right], \tag{A.1d}$$

$$\sigma_{zz}(r,z) = \frac{1}{\partial z}\left[(2-\nu)\nabla^2\Phi - \frac{\partial^2\Phi}{\partial z^2}\right], \tag{A.1e}$$

$$\tau_{rz}(r,z) = \frac{1}{\partial r}\left[(1-\nu)\nabla^2\Phi - \frac{\partial^2\Phi}{\partial z^2}\right], \tag{A.1f}$$

$$\nabla^2\nabla^2\Phi(r,z) = 0, \tag{A.1g}$$

where μ is the shear modulus, ν the Poisson's ratio, u_r and u_z are the radial and z-direction components of the displacement vector, respectively, and ∇^2 is the axisymmetric Laplace's operator. Since the problem considered here is also symmetric about the plane $z = 0$, in what follows only the upper half, i.e., the $0 \le z < \infty$ region, will be considered.

The two stress functions for the fiber and the matrix can be expressed as [50, 51]

$$\Phi_1(r,z) = \frac{2}{\pi}\int_0^\infty [f_1(s)I_0(rs) + f_2(s)rsI_1(rs)]\sin(zs)ds$$

$$+ \int_0^\infty f_0(p)p(2\nu_1 + zp)e^{-zp}J_0(rp)dp, \qquad \text{(A.2a)}$$

$$\Phi_2(r,z) = \frac{2}{\pi}\int_0^\infty [f_3(s)K_0(rs) + f_4(s)rsK_1(rs)]\sin(zs)ds$$

$$+ \int_0^\infty g_0(p)p(2\nu_2 + zp)e^{-zp}J_0(rp)dp. \qquad \text{(A.2b)}$$

Using the relations in Eqs (A.1a-f) and the stress functions yields the displacement and stress fields:

$$u_r^1(r,z) = -\frac{1}{2\mu_1}\frac{2}{\pi}\int_0^\infty [f_1(s)I_1(rs) + f_2(s)rsI_0(rs)]s^2\cos(zs)ds$$

$$+ \frac{1}{2\mu_1}\int_0^\infty f_0(p)p^3(1-2\nu_1 - zp)e^{-zp}J_1(rp)dp, \qquad \text{(A.3a)}$$

$$u_z^1(r,z) = \frac{1}{2\mu_1}\frac{2}{\pi}\int_0^\infty \{f_1(s)I_0(rs) + f_2(s)[4(1-\nu_1)I_0(rs) + rsI_1(rs)]\}s^2\sin(zs)ds$$

$$- \frac{1}{2\mu_1}\int_0^\infty f_0(p)p^3[2(1-\nu_1) + zp)]e^{-zp}J_0(rp)dp, \qquad \text{(A.3b)}$$

$$\sigma_{rr}^1(r,z) = \frac{2}{\pi}\int_0^\infty \{f_1(s)[-I_0(rs) + I_1(rs)/rs]$$

$$+ f_2(s)[(2\nu_1 - 1)I_0(rs) - rsI_1(rs)]\}s^3\cos(zs)ds$$

$$+ \int_0^\infty f_0(p)p^4[(1-zp)J_0(rp) - (1-2\nu_1 - zp)J_1(rp)/rp]e^{-zp}dp, \qquad \text{(A.3c)}$$

$$\sigma_{zz}^1(r,z) = \frac{2}{\pi}\int_0^\infty \{f_1(s)I_0(rs) + f_2(s)[2(2-\nu_1)I_0(rs) + rsI_1(rs)]\}s^3\cos(zs)ds$$

$$+\int_0^\infty f_0(p)p^4(1+zp)J_0(rp)e^{-zp}dp, \tag{A.3d}$$

$$\tau_{rz}^1(r,z)=\frac{2}{\pi}\int_0^\infty\{f_1(s)I_1(rs)+f_2(s)[rsI_0(rs)+2(1-\nu_1)I_1(rs)]\}s^3\sin(zs)ds$$

$$+\int_0^\infty f_0(p)p^5zJ_1(rp)e^{-zp}dp, \tag{A.3e}$$

$$u_r^2(r,z)=\frac{1}{2\mu_2}\frac{2}{\pi}\int_0^\infty[f_3(s)K_1(rs)+f_4(s)rsK_0(rs)]s^2\cos(zs)ds$$

$$+\frac{1}{2\mu_2}\int_0^\infty g_0(p)p^3(1-2\nu_2-zp)e^{-zp}J_1(rp)dp, \tag{A.3f}$$

$$u_z^2(r,z)=\frac{1}{2\mu_2}\frac{2}{\pi}\int_0^\infty\{f_3(s)K_0(rs)+f_4(s)[rsK_1(rs)-4(1-\nu_2)K_0(rs)]\}s^2\sin(zs)ds$$

$$-\frac{1}{2\mu_2}\int_0^\infty g_0(p)p^3[2(1-\nu_2)+zp)]e^{-zp}J_0(rp)dp, \tag{A.3g}$$

$$\sigma_{rr}^2(r,z)=\frac{2}{\pi}\int_0^\infty\{-f_3(s)[K_0(rs)+K_1(rs)/rs]$$

$$+f_4(s)[(1-2\nu_2)K_0(rs)-rsK_1(rs)]\}s^3\cos(zs)ds$$

$$+\int_0^\infty g_0(p)p^4[(1-zp)J_0(rp)-(1-2\nu_2-zp)J_1(rp)/rp]e^{-zp}dp, \tag{A.3h}$$

$$\sigma_{zz}^2(r,z)=\frac{2}{\pi}\int_0^\infty\{f_3(s)K_0(rs)+f_4(s)[-2(2-\nu_2)K_0(rs)+rsK_1(rs)]\}s^3\cos(zs)ds$$

$$+\int_0^\infty g_0(p)p^4(1+zp)J_0(rp)e^{-zp}dp, \tag{A.3i}$$

$$\tau_{rz}^2(r,z)=\frac{2}{\pi}\int_0^\infty\{-f_3(s)K_1(rs)+f_4(s)[-rsK_0(rs)+2(1-\nu_2)K_1(rs)]\}s^3\sin(zs)ds$$

$$+\int_0^\infty g_0(p)p^5 z J_1(rp)e^{-zp}dp, \qquad \text{(A.3j)}$$

where f_i $(i = 0,1,...,4)$ and g_0 are unknown functions, and J_j, I_j, K_j $(j=0,1)$ are Bessel functions of the first kind, and modified Bessel functions of the first and the second kind, respectively.

A.1.2 Boundary and continuity conditions

The boundary and continuity conditions at the interface are:

$$u_r^1(a,z) = u_r^2(a,z), \qquad 0 \le z < b_3,\ c_3 < z < \infty, \qquad \text{(A.4a)}$$

$$\sigma_{rr}^1(a,z) = \sigma_{rr}^2(a,z), \qquad 0 \le z < \infty, \qquad \text{(A.4b)}$$

$$\sigma_{rr}^1(a,z) = \sigma_{rr}^2(a,z) = -p_3(z), \qquad b_3 \le z < c_3, \qquad \text{(A.4c)}$$

$$u_z^1(a,z) = u_z^2(a,z), \qquad 0 \le z < b_3,\ c_3 < z < \infty, \qquad \text{(A.4d)}$$

$$\tau_{rz}^1(a,z) = \tau_{rz}^2(a,z), \qquad 0 \le z < \infty, \qquad \text{(A.4e)}$$

$$\tau_{rz}^1(a,z) = \tau_{rz}^2(a,z) = p_4(z), \qquad b_3 < z < c_3. \qquad \text{(A.4f)}$$

Also at $z = 0$ plane the boundary and symmetry conditions are:

$$u_z^1(r,0) = 0, \qquad 0 \le r < b_1,\ c_1 < y < a, \qquad \text{(A.4g)}$$

$$\tau_{rz}^1(r,0) = 0, \qquad 0 \le r < a, \qquad \text{(A.4h)}$$

$$u_z^2(r,0) = 0, \qquad a < r < b_2,\ c_2 < r < \infty, \qquad \text{(A.4i)}$$

$$\tau_{rz}^2(r,0) = 0, \qquad a < r < \infty, \qquad \text{(A.4j)}$$

$$\sigma_{zz}^{1}(r,0) = -p_1(r), \qquad b_1 < r < c_1, \tag{A.4k}$$

$$\sigma_{zz}^{2}(r,0) = -p_2(r), \qquad b_2 < r < c_2, \tag{A.4l}$$

where p_i (i=1,...,4) are the possible tractions on the crack surfaces.

A.1.3 Definition of continuous dislocations

Applying the conditions given above directly, the problem can be reduced to a system of dual integral equations. It can also be reduced to a system of singular integral equations by introducing the following four dislocation functions:

$$\varphi_1(r) = \frac{\mu_1}{1-\nu_1}\frac{\partial u_z^1(r,+0)}{\partial r}, \tag{A.5a}$$

$$\varphi_2(r) = \frac{\mu_2}{1-\nu_2}\frac{\partial u_z^2(r,+0)}{\partial r}, \tag{A.5b}$$

$$\varphi_3(z) = 2\mu_1\frac{\partial}{\partial z}\left[u_r^2(a+0,z) - u_r^1(a-0,z)\right], \tag{A.5c}$$

$$\varphi_4(z) = 2\mu_1\frac{\partial}{\partial z}\left[u_z^2(a+0,z) - u_z^1(a-0,z)\right]. \tag{A.5d}$$

From the above definitions and Eqs (A.4a-i) it can easily be seen that the each dislocation function φ_i (i = 1, ..,4) vanishes except along its relevant crack line.

A.1.4 Derivation of singular integral equations

Using Eqs (A.4g), (A.4i) and (A.5a-b), one can show that

$$f_0(p) = \frac{1}{p^3}\int_{b_1}^{c_1} r\varphi_1(r) J_1(rp)dr\,, \tag{A.6a}$$

and

$$g_0(p) = \frac{1}{p^3}\int_{b_2}^{c_2} r\varphi_2(r) J_1(rp)dr\,. \tag{A.6b}$$

The remaining four unknown functions f_i (i=1,...,4) can also be expressed in terms of the unknown functions φ_j (j=1,..,4). Using Eqs (A.4b), (A.4e), (A.5c) and (A.5d) and taking the inverse transforms, one obtains the following system of four algebraic equations:

$$f_1(s)(-I_0(as) + I_1(as)/as) + f_2(s)[(2\nu_1 - 1)I_0(as) - asI_1(as)]$$
$$+f_3(s)(K_0(as) + K_1(as)/as) + f_4(s)[-(1-2\nu_2)K_0(as) + asK_1(as)] = R_1(s), \tag{A.7a}$$

$$f_1(s)I_1(as) + f_2(s)[(asI_0(as) + 2(1-\nu_1)I_1(as)] + f_3(s)K_1(as)$$
$$+f_4(s)[asK_0(as) - 2(1-\nu_2)K_1(as)] = R_2(s), \tag{A.7b}$$

$$-f_1(s)I_1(as) - f_2(s)asI_0(as) - f_3(s)\lambda K_1(as) - f_4(s)\lambda asK_1(as) = R_3(s), \tag{A.7c}$$

$$-f_1(s)I_0(as) - f_2(s)[4(1-\nu_1)I_0(as) + asI_1(as)] + f_3(s)\lambda K_0(as)$$
$$+f_4(s)[-4\lambda(1-\nu_2)K_0(as) + \lambda asK_1(as)] = R_4(s), \tag{A.7d}$$

where $\lambda=\mu_1/\mu_2$, and the right hand side terms (R_i, i=1,..,4) are given by:

$$R_i(s) = -\frac{1}{s^3}\int_{b_1}^{c_1} t\varphi_1(t)h_{1i}dt + \frac{1}{s^3}\int_{b_2}^{c_2} t\varphi_2(t)h_{2i}dt\,, \qquad (i=1,2), \tag{A.8a}$$

$$R_3(s) = -\frac{1}{s^3}\int_{b_1}^{c_1} t\varphi_1(t)h_{13}dt + \frac{\lambda}{s^3}\int_{b_2}^{c_2} t\varphi_2(t)h_{23}dt + \frac{1}{s^3}\int_{b_3}^{c_3} \varphi_3(t)\sin(ts)\,dt\,, \tag{A.8b}$$

$$R_4(s) = -\frac{1}{s^3}\int_{b_1}^{c_1} t\varphi_1(t)h_{14}dt + \frac{\lambda}{s^3}\int_{b_2}^{c_2} t\varphi_2(t)h_{24}dt + \frac{1}{s^3}\int_{b_3}^{c_3} \varphi_4(t)\cos(ts)\,dt\,, \tag{A.8c}$$

here h_{ki} (k=1, 2, i=1,...,4) can further be expressed as

$$h_{11} = [K_0(as) + K_1(as)/as]ts^2 I_0(ts)$$

$$- \{K_0(as) + [a^2s^2 + 2(1-\nu_1)]K_1(as)/as\} sI_1(ts), \quad \text{(A.9a)}$$

$$h_{12} = ts^2 K_1(as) I_0(ts) - asK_0(as) sI_1(ts), \quad \text{(A.9b)}$$

$$h_{13} = -ts^2 K_1(as) I_0(ts) + [asK_0(as) + 2(1-\nu_1)K_1(as)] sI_1(ts), \quad \text{(A.9c)}$$

$$h_{14} = ts^2 K_0(as) I_0(ts) + [-asK_1(as) + 2(1-\nu_1)K_0(as)] sI_1(ts). \quad \text{(A.9d)}$$

$$h_{21} = [I_0(as) - I_1(as)/as]ts^2 K_0(ts)$$

$$+ \{I_0(as) - [a^2s^2 + 2(1-\nu_2)]I_1(as)/as\} sK_1(ts), \quad \text{(A.9e)}$$

$$h_{22} = -ts^2 I_1(as) K_0(ts) + asI_0(as) sK_1(ts), \quad \text{(A.9f)}$$

$$h_{23} = ts^2 I_1(as) K_0(ts) + [-asI_0(as) + 2(1-\nu_2)I_1(as)] sK_1(ts), \quad \text{(A.9g)}$$

$$h_{24} = ts^2 I_0(as) K_0(ts) - [asI_1(as) + 2(1-\nu_2)I_0(as)] sK_1(ts), \quad \text{(A.9h)}$$

The solution of Eqs (A.7a-d) can be expressed as

$$f_i(s) = \frac{1}{D(s)} \sum_{j=1}^{4} C_{ji}(s) R_j(s), \quad (i=1,..,4), \quad \text{(A.10a)}$$

where $D(s)$ is the determinant of the matrix of coefficients of Eqs (A.7*a-d*) and $C_{ji}(s)$ (i, j = 1,...,4) are the elements of the adjoint of the matrix. Using Eqs (A.8*a-c*), Eq. (A.10a) may be written as

$$f_i(s) = \frac{1}{D(s)s^3} \left\{ -\int_{b_1}^{c_1} t\varphi_1(t) \sum_{j=1}^{4} C_{ji} h_{1j}(s,t) dt + \int_{b_2}^{c_2} t\varphi_2(t) H_i(s,t) dt + \right.$$

$$\left. + \int_0^{c_3} \varphi_3(t) C_{3i}(s) \sin(ts) dt + \int_0^{c_3} \varphi_4(t) C_{4i}(s) \cos(ts) dt \right\}, \quad (i = 1,...,4), \quad \text{(A.10b)}$$

where

$$H_i(s,t) = C_{1i}h_{21} + C_{2i}h_{22} + \lambda C_{3i}h_{23} + \lambda C_{4i}h_{24}. \qquad \text{(A.10c)}$$

Now substituting Eqs (A.6a-b) and (A.10b) for f_i (i = 0,...,4) and g_0 in Eqs (A.3c-e) and (A.3i), and after lengthy algebra and asymptotic analysis, one can obtain the following system of singular integral equations:

$$\frac{1}{\pi}\int_{b_1}^{c_1}\frac{\varphi_1(t)}{t-r}dt + \frac{2}{\pi}\sum_{j=1}^{4}\int_{b_j}^{c_j}k_{1j}(t,r)\varphi_j(t)dt = -p_1(r), \qquad b_1 < r < c_1, \qquad \text{(A.11a)}$$

$$\frac{1}{\pi}\int_{b_2}^{c_2}\frac{\varphi_2(t)}{t-r}dt + \frac{2}{\pi}\sum_{j=1}^{4}\int_{b_j}^{c_j}k_{2j}(t,r)\varphi_j(t)dt = -p_2(r), \qquad b_2 < r < c_2, \qquad \text{(A.11b)}$$

$$\frac{1}{\pi}\int_{b_3}^{c_3}\left(\frac{1}{t-z}+\frac{1}{t+z}\right)\varphi_3(t)dt + \gamma\varphi_4(z)$$

$$+\frac{2}{\pi\gamma_{11}}\sum_{j=1}^{4}\int_{b_j}^{c_j}k_{3j}(t,z)\varphi_j(t)dt = \frac{-p_3(z)}{\gamma_{11}}, \qquad b_3 < z < c_3, \qquad \text{(A.11c)}$$

$$\frac{1}{\pi}\int_{b_3}^{c_3}\left(\frac{1}{t-z}-\frac{1}{t+z}\right)\varphi_4(t)dt - \gamma\varphi_3(z)$$

$$+\frac{2}{\pi\gamma_{11}}\sum_{j=1}^{4}\int_{b_j}^{c_j}k_{4j}(t,z)\varphi_j(t)dt = \frac{p_4(z)}{\gamma_{11}}, \qquad b_3 < z < c_3, \qquad \text{(A.11d)}$$

where $b_4 = b_3$, $c_4 = c_3$, $\gamma = \gamma_{12}/\gamma_{11}$,

$$\gamma_{11} = \frac{\lambda+\kappa_1+1+\lambda\kappa_2}{2(\lambda+\kappa_1)(1+\lambda\kappa_2)}, \quad \gamma_{12} = \frac{\lambda+\kappa_1-(1+\lambda\kappa_2)}{2(\lambda+\kappa_1)(1+\lambda\kappa_2)}, \quad \kappa_i = 3-4\nu_i\,(i=1,2), \qquad \text{(A.12)}$$

and the kernels k_{ij} $(i, j=1,...,4)$ can be expressed as:

$$k_{11}(t,r) = -t\int_0^\infty \left[k_1^1(rs)\sum_{i=1}^4 C_{i1}h_{1i}(s,t) + k_2^1(rs)\sum_{i=1}^4 C_{i2}h_{1i}(s,t) \right] \frac{ds}{D(s)}$$

$$+\frac{1}{2}\begin{cases} E(r/t)/(t+r) + (E(r/t)-1)/(t-r), & r<t \\ (E(t/r)-1)/(t-r) - E(t/r)/(t+r) + 2K(t/r)/r, & t<r \end{cases}, \quad \text{(A.13a)}$$

$$k_{12}(t,r) = t\int_0^\infty \left(k_1^1(rs)H_1(s,t) + k_2^1(rs)H_2(s,t) \right) \frac{ds}{D(s)} \quad \text{(A.13b)}$$

$$k_{13}(t,r) = \int_0^\infty \left[k_1^1(rs)C_{31}(s) + k_2^1(rs)C_{32}(s) \right] \sin(ts)/D(s)ds, \quad \text{(A.13c)}$$

$$k_{14}(t,r) = \int_0^\infty \left[k_1^1(rs)C_{41}(s) + k_2^1(rs)C_{42}(s) \right] \cos(ts)/D(s)ds, \quad \text{(A.13d)}$$

$$k_{21}(t,r) = -t\int_0^\infty \left[k_1^2(rs)\sum_{i=1}^4 C_{i3}(s)h_{1i}(s,t) + k_2^2(rs)\sum_{i=1}^4 C_{i4}(s)h_{1i}(s,t) \right] \frac{ds}{D(s)} \quad \text{(A.14a)}$$

$$k_{22}(t,r) = t\int_0^\infty \left[\sum_{i=1}^2 k_i^2(rs)B_i(s,t) \right] \frac{ds}{D(s)}$$

$$+\frac{1}{2}\begin{cases} \dfrac{E(r/t)}{t+r} + \dfrac{E(r/t)-1}{(t-r)}, & r<t \\ \dfrac{E(t/r)-1}{t-r} - \dfrac{E(t/r)}{t+r} + \dfrac{2K(t/r)}{r}, & t<r \end{cases}, \quad \text{(A.14b)}$$

$$k_{23}(t,r) = \int_0^\infty \left[k_1^2(rs)C_{33}(s) + k_2^2(rs)C_{34}(s) \right] \sin(ts)/D(s)ds, \quad \text{(A.14c)}$$

$$k_{24}(t,r)=\int_0^{\infty}\left[k_1^2(rs)C_{43}(s)+k_2^2(rs)C_{44}(s)\right]\cos(ts)/D(s)ds, \tag{A.14d}$$

$$k_{31}(t,z)=-t\int_0^{\infty}\left[k_1^3(s)\sum_{i=1}^{4}C_{i1}(s)h_{1i}(s,t)+k_2^3(s)\sum_{i=1}^{4}C_{i2}(s)h_{1i}(s,t)\right]\frac{\cos(zs)}{D(s)}ds$$

$$+\frac{\pi t}{2}\int_0^{\infty}p\left[(1-zp)J_0(ap)-(1-2\nu_1-zp)J_1(ap)/ap\right]J_1(tp)e^{-zp}dp, \tag{A.15a}$$

$$k_{32}(t,z)=t\int_0^{\infty}\left(k_1^3(s)H_1(s,t)+k_2^3(s)H_2(s,t)\right)\cos(zs)/D(s)ds, \tag{A.15b}$$

$$k_{33}(t,z)=\int_0^{\infty}\left[(k_1^3(s)C_{31}(s)-k_2^3(s)C_{32}(s))/D(s)-\gamma_{11}\right]\sin(ts)\cos(zs)ds, \tag{A.15c}$$

$$k_{34}(t,z)=\int_0^{\infty}\left[(k_1^3(s)C_{41}(s)-k_2^3(s)C_{42}(s))/D(s)-\gamma_{12}\right]\cos(ts)\cos(zs)ds, \tag{A.15d}$$

$$k_{41}(t,z)=-t\int_0^{\infty}\left[k_1^4(s)\sum_{i=1}^{4}C_{i1}(s)h_{1i}(s,t)+k_2^4(s)\sum_{i=1}^{4}C_{i2}(s)h_{1i}(s,t)\right]\frac{\sin(zs)}{D(s)}ds$$

$$+\frac{\pi t}{2}\int_0^{\infty}p^2J_1(ap)J_1(tp)e^{-zp}dp, \tag{A.16a}$$

$$k_{42}(t,z)=t\int_0^{\infty}\left(k_1^4(s)H_1(s,t)+k_2^4(s)H_2(s,t)\right)\sin(zs)/D(s)ds, \tag{A.16b}$$

$$k_{43}(t,z)=\int_0^{\infty}\left[(k_1^4(s)C_{31}(s)+k_2^4(s)C_{32}(s))/D(s)+\gamma_{12}\right]\sin(ts)\sin(zs)ds, \tag{A.16c}$$

$$k_{44}(t,z)=\int_0^{\infty}\left[(k_1^4(s)C_{41}(s)+k_2^4(s)C_{42}(s))/D(s)+\gamma_{11}\right]\cos(ts)\sin(zs)ds, \qquad \text{(A.16d)}$$

here

$$\begin{aligned}
&k_1^1(rs)=I_0(rs), && k_2^1(rs)=2(2-\nu_1)I_0(rs)+rsI_1(rs),\\
&k_1^2(rs)=K_0(rs), && k_2^2(rs)=-2(2-\nu_2)K_0(as)+rsK_1(rs),\\
&k_1^3(s)=-I_0(as)+I_1(as)/as, && k_2^3(s)=(2\nu_1-1)I_0(as)-I_1(as)/as,\\
&k_1^4(s)=I_1(as), && k_2^4(s)=asI_0(as)+2(1-\nu_1)I_1(as),
\end{aligned} \qquad \text{(A.17)}$$

$$\begin{aligned}
B_i(s,t)&=C_{1i+2}(s)h_{21}(s,t)+C_{2i+2}(s)h_{22}(s,t)\\
&\quad+\lambda C_{3i+2}(s)h_{21}(s,t)+C_{4i+2}(s)h_{22}(s,t),
\end{aligned} \qquad \text{(A.18)}$$

and the functions $E(\,)$ and $K(\,)$ are complete elliptic integrals of the first and second kind, respectively. These kernels are bonded in their respective closed domains of definitions or at most weakly singular whenever the inner matrix crack tip and the outer fiber crack tip do not terminate at the interface.

When the matrix crack or the crack in the fiber terminates at the interface, some kernels will not be bounded for all values of the augments in their respective domains of definitions. These singular behaviors, which determine the singular behaviors of the dislocations, will be considered in the following section.

A.2 Singularities at crack tips

It is well known that the singular behavior in singular integral equations depends only on the singular parts of the kernels, which in turn depend on crack configurations. In comparing the above integral equations with those derived for plane problems [85, 86],

one observes that they have the same singular parts for similar crack configurations. If any crack tip of the matrix crack and/or the fiber crack touches the interface, some of the Fredholm kernels in Eqs. (A.13-16) will become singular. The singular parts can easily be determined using the techniques developed for plane problems.

A.2.1 Singularities for embedded cracks

For this well known crack configuration where both the fiber and the matrix cracks are away from the interface, the form of the solution can be found from [85-87]:

$$\varphi_1(t) = (c_1 - t)^{\alpha_1}(t - b_1)^{\beta_1} g_1(t), \qquad b_1 < t < c_1, \tag{A.19a}$$

$$\varphi_2(t) = (c_2 - t)^{\alpha_2}(t - b_2)^{\beta_2} g_2(t), \qquad b_2 < t < c_2, \tag{A.19b}$$

$$\varphi(t) = (c_3 - t)^{\alpha_3}(t - b_3)^{\beta_3} g(t), \qquad b_3 < t < c_3, \tag{A.19c}$$

where $\varphi = \varphi_3 + i\varphi_4$,

$$\alpha_1 = \beta_1 = -\tfrac{1}{2},\ \alpha_2 = \beta_2 = -\tfrac{1}{2},$$

$$\alpha_3 = -1/2 - i\omega,\ \ \beta_3 = -1/2 + i\,\omega,\ \ \omega = \frac{1}{2\pi}\log\left(\frac{1+\gamma}{1-\gamma}\right), \tag{A.20}$$

$g_1(t)$, $g_2(t)$ and $g(t)$ are regular functions in their respective domains of definitions.

A.2.2 Singularities for a transverse crack terminating at the interface without intersecting the interface crack

When the matrix crack terminates at the interface without intersecting another

crack, k_{22} is the only kernel that exhibits singular behavior as r and t approach the interface simultaneously. The singular part can be separated by using asymptotic expansion techniques. After some lengthy manipulations the asymptotic expression of k_{22} may be written as

$$k_{22}^{\infty}(t,r) = k_{22}^{s}(t,r) + k_{22}^{r}(t,r), \tag{A.21a}$$

where k^{s}_{22} is the singular part, which has the form

$$k_{22}^{s}(t,r) = \frac{1}{2}\sqrt{\frac{t}{r}}\left[\frac{c_{20}}{(r+t-2a)} + \frac{c_{21}(r-a)}{(r+t-2a)^2} + \frac{c_{22}(r-a)^2}{(r+t-2a)^3}\right], \tag{A.21b}$$

$$c_{20} = \frac{1}{2} - \frac{\lambda(1+\kappa_2)}{2(\lambda+\kappa_1)} - \frac{3(1-\lambda)}{2(1+\lambda\kappa_2)}, \tag{A.21c}$$

$$c_{21} = \frac{6(1-\lambda)}{(1+\lambda\kappa_2)}, \quad c_{22} = \frac{-4(1-\lambda)}{(1+\lambda\kappa_2)}, \tag{A.21d}$$

and $k_{22}^{r}(t,r)$ is the regular part, which is too complicated to be given here. The above expressions were also derived in [50].

The kernel $k_{22}^{s}(t,r)$ and the Cauchy singular kernel in Eq. (A.11*b*) constitute the so-called generalized Cauchy kernel. Following the procedures cited in [87, 88], or using the results in [50, 85, 87] directly, one may obtain the following two characteristic equations to determine the powers of singularity for φ_2:

$$\cot(\pi\alpha_2) = 0, \tag{A.22*a*}$$

$$\cos(\pi\beta_2) + c_{20} - c_{21}\beta_2 + \frac{c_{22}}{2}\beta_2(\beta_2 - 1) = 0. \tag{A.22*b*}$$

Obviously, $\alpha_2 = -\frac{1}{2}$, and β_2 can be determined by solving Eq. (A.22*b*).

Similarly as the fiber crack terminates at the interface without intersecting another crack, the asymptotic expression of k_{11} may be written as

$$k_{11}^{\infty}(t,r) = k_{11}^{s}(t,r) + k_{11}^{r}(t,r), \tag{A.23a}$$

where k_{11}^{s} is the singular part, and has the form:

$$k_{11}^{s}(t,r) = \frac{1}{2}\sqrt{\frac{t}{r}}\left[\frac{b_{10}}{(2a-r-t)} + \frac{b_{11}(a-r)}{(2a-r-t)^2} + \frac{b_{12}(a-r)^2}{(2a-r-t)^3}\right], \tag{A.23b}$$

$$b_{10} = -\frac{1}{2} - \frac{3(1-\lambda)}{2(\lambda+\kappa_1)} + \frac{1+\kappa_1}{2(1+\lambda\kappa_2)}, \tag{A.23c}$$

$$b_{11} = \frac{6(1-\lambda)}{\lambda+\kappa_1}, \quad b_{12} = \frac{-4(1-\lambda)}{\lambda+\kappa_1}, \tag{A.23d}$$

and $k_{11}^{r}(t,r)$ is the regular part. The two characteristic equations to determine the powers of singularity for φ_4 are

$$\cot(\pi\beta_1) = 0, \tag{A.24a}$$

$$\cos(\pi\alpha_1) - b_{10} + b_{11}\alpha_4 - \frac{b_{12}}{2}\alpha_1(\alpha_1 - 1) = 0. \tag{A.24b}$$

Obviously, $\beta_1 = -\frac{1}{2}$, and α_1 can be determined by solving Eq. (A.24*b*).

A.2.3 Singularities for intersecting cracks at interface

In what follows four possible cases will be considered. Since the same derivation procedure applies to all four cases, the detailed procedure will be given only in the first situation, while for the remaining three cases only the main conclusions will be presented.

(a) *Singular powers for intersecting interface and matrix cracks*: When the matrix crack intersects the interface crack while the fiber crack is away from the interface or does not exist, k_{32}, k_{42}, k_{23}, k_{24} and k_{22} all exhibit singular behavior. Again, using the asymptotic techniques, one obtains the following expressions:

$$k_{32}^{\infty} = k_{32}^{s} + k_{32}^{r} = \frac{1}{2}\sqrt{\frac{t}{a}}\left\{\frac{c_{31}(t-a)}{(t-a)^2+z^2} + \frac{c_{32}(t-a)\left[(t-a)^2-3z^2\right]}{\left[(t-a)^2+z^2\right]^2}\right\} + k_{32}^{r}, \qquad \text{(A.25}a\text{)}$$

$$k_{42}^{\infty} = k_{42}^{s} + k_{42}^{r} = \frac{1}{2}\sqrt{\frac{t}{a}}\left\{\frac{c_{31}z}{(t-a)^2+z^2} + \frac{c_{32}z\left[z^2-3(t-a)^2\right]}{\left[(t-a)^2+z^2\right]^2}\right\} + k_{42}^{r}, \qquad \text{(A.25}b\text{)}$$

$$k_{23}^{\infty} = k_{23}^{s} + k_{23}^{r} = \sqrt{\frac{a}{r}}\left\{\frac{b_{31}t}{(r-a)^2+t^2} - \frac{b_{32}t(r-a)^2}{\left[(r-a)^2+t^2\right]^2}\right\} + k_{23}^{r}, \qquad \text{(A.25}c\text{)}$$

$$k_{24}^{\infty} = k_{24}^{s} + k_{24}^{r} = \sqrt{\frac{a}{r}}\left\{\frac{b_{42}(r-a)}{(r-a)^2+t^2} + \frac{b_{32}t^2(r-a)}{\left[(t-a)^2+z^2\right]^2}\right\} + k_{24}^{r}, \qquad \text{(A.25}d\text{)}$$

where

$$c_{31} = \frac{\lambda(1+\kappa_2)}{2(\lambda+\kappa_1)}, \quad c_{32} = \frac{\lambda(1+\kappa_2)}{2(1+\lambda\kappa_2)}, \qquad \text{(A.25}e\text{)}$$

$$b_{31} = -\frac{1}{2(\lambda+\kappa_1)} + \frac{3}{2(1+\lambda\kappa_2)}, \quad b_{32} = \frac{2}{1+\lambda\kappa_2},$$

$$b_{42} = \frac{1}{2(\lambda+\kappa_1)} + \frac{1}{2(1+\lambda\kappa_2)}, \qquad \text{(A.25}f\text{)}$$

and k_{32}^{r}, k_{42}^{r}, k_{23}^{r} and k_{24}^{r} are all regular functions of t and r.

So in this case the dominant kernels of the three integral equations involved are all of generalized Cauchy type. It must be pointed out again that each of the singular kernels

in Eq. (A.25) is the same as the corresponding one in the similar plane-strain problem [85]. Therefore the singular behaviors of the solution for the current integral equations should be the same as those of the analogous plane-strain problem. The three relevant dislocation functions can be expressed as:

$$\varphi_2(t) = (t-a)^{\beta}(c_2 - t)^{\alpha_2} g_2(t), \tag{A.26a}$$

$$\varphi_3(t) = t^{\beta}(c_3 - t)^{\alpha_3} g_3(t), \tag{A.26b}$$

$$\varphi_4(t) = t^{\beta}(c_3 - t)^{\alpha_3} g_4(t), \tag{A.26c}$$

where α_2 and α_3 assume the same values as given in Eq. (A.20), and $g_2(t)$, $g_3(t)$ and $g_4(t)$ are regular functions of t. Since the fiber crack, if present, still remains embedded in a homogeneous material, the singular powers for φ_1 are the same as those given in Eq. (A.20). Substituting above expressions into Eqs (A.11b-d), and following the procedure used in [85, 87], one obtains the following three algebraic equations:

$$\left[-\cot\pi\beta - \frac{c_{20}}{\sin\pi\beta} + \frac{c_{21}\beta}{\sin\pi\beta} - \frac{c_{22}\beta(\beta-1)}{2\sin\pi\beta}\right](c_2 - a)^{\alpha_2} g_2(a)$$

$$-(b_{31} + \frac{b_{32}}{2}\beta)\frac{c_3^{\alpha_3}}{\sin\frac{\pi\beta}{2}} g_3(0) + \left[b_{42} + \frac{b_{32}(1+\beta)}{2}\right]\frac{c_3^{\alpha_3}}{\cos\frac{\pi\beta}{2}} g_4(0) = 0, \tag{A.27a}$$

$$(\frac{c_{31} + c_{32} + 2c_{32}\beta}{a_{11}})\frac{(c_2 - a)^{\alpha_2}}{2\sin\frac{\pi\beta}{2}} g_2(a)$$

$$+(\cot\pi\beta + \frac{1}{\sin\pi\beta})c_3^{\alpha_3} g_3(0) - \gamma c_3^{\alpha_3} g_4(0) = 0, \tag{A.27b}$$

$$\left[\frac{c_{31}-c_{32}-2c_{32}\beta}{a_{11}}\right]\frac{(c_3-a)^{\alpha_3}}{2\cos\dfrac{\pi\beta}{2}}g_2(a)-\gamma c_3^{\alpha_3}g_3(0)$$

$$+(-\cot\pi\beta+\frac{1}{\sin\pi\beta})c_3^{\alpha_3}g_4(0)=0\ . \tag{A.27c}$$

For the above equations to have nontrivial solution for $g_2(0)$, $g_3(0)$, and $g_4(a)$, the determinant of the coefficient matrix must be equal to zero, i.e.,

$$\frac{1}{\sin\pi\beta}\left[\cos\pi\beta-2(\beta+1)^2+1\right]=0, \tag{A.28}$$

which, as expected, gives the power of singularity as $\beta=0$. It can be shown that only one equation is independent in Eqs (A.27a-c) and can be expressed as

$$\frac{\lambda(1+k_2)}{2}(c_2-a)^{\alpha_2}g_2(a)+g_3(0)c_3^{\alpha_3}=0. \tag{A.29}$$

(b) *Singularities for intersecting interface and fiber cracks*: This is the case when the fiber crack intersects with the fiber/matrix interface crack while the matrix crack is away from the interface or not present, and thus very similar to the above one. Using the above procedure, one can derive the similar conclusions:

$$\varphi_1(t)=(a-t)^0(t-b_1)^{\beta_1}g_1(t), \tag{A.30a}$$

$$\varphi_3(t)=t^0(c_3-t)^{\alpha_3}g_3(t), \tag{A.30b}$$

$$\varphi_4(t)=t^0(c_3-t)^{\alpha_3}g_4(t), \tag{A.30c}$$

where α_3 and β_1 assume the same values as given in Eq. (A.20), and $g_1(t)$, $g_3(t)$, and $g_4(t)$ are regular functions of t. The singular powers for φ_2 remain as those as in embedded case

if the matrix crack is present. The condition relating the values of dislocations at the intersecting tip is given by equation:

$$\frac{1+\kappa_1}{2}(a-b_1)^{\beta_1} g_1(a) - g_3(0)c_3^{\alpha_3} = 0. \tag{A.31}$$

(c) *Singular powers for intersecting fiber and matrix cracks*: This is the situation when the fiber and matrix cracks cross the interface and connect with each other, while the interfacial crack keeps away from intersecting them or does not exist. The two related dislocation functions may be expressed as

$$\varphi_1(t) = (t-b_1)^{\beta_1}(a-t)^{\beta} g_1(t), \tag{A.32a}$$

$$\varphi_2(t) = (t-a)^{\beta}(c_2-t)^{\alpha_2} g_2(t), \tag{A.32b}$$

where α_2 and β_1 are equal to $-1/2$. The following characteristic equation can be derived to determine β:

$$\left[\cos\pi\beta - b_{10} + b_{11}\beta - \frac{b_{12}}{2}\beta(\beta-1)\right]\left[\cos\pi\beta + c_{20} - c_{21}\beta + \frac{c_{22}}{2}\beta(\beta-1)\right]$$

$$+\left[3b_{21} - b_{22} + 2(b_{21}-b_{22})\beta\right]\left[-3c_{31} + c_{32} + 2(c_{32}-c_{31})\beta\right] = 0. \tag{A.33}$$

Also the dislocations should satisfy the relation:

$$g_1(a)(a-b_1)^{\beta_1}\left[\cos\pi\beta - b_{10} + b_{11}\beta - \frac{b_{12}}{2}\beta(\beta-1)\right]$$

$$+g_2(a)(c_2-a)^{\alpha_2}\left[-3c_{21} + c_{22} + 2(c_{22}-c_{21})\beta\right] = 0 \tag{A.34}$$

(d) *Singularities for intersecting interface and two transverse cracks*: When the interface, fiber and matrix cracks intersect at the interface, all four singular integral equations have generalized Cauchy kernels which govern the singular powers of four

dislocations at the intersecting tip. Using the same procedure as used in case (a), one can show that they are equal to zero, that is, the solution of the equations can be assumed as

$$\varphi_1(t) = (t - b_1)^{\beta_1} g_1(t), \qquad b_1 < t < a, \tag{A.35a}$$

$$\varphi_2(t) = (c_2 - t)^{\alpha_2} g_2(t), \qquad a < t < c_2, \tag{A.35b}$$

$$\varphi(t) = (c_3 - t)^{\alpha_3} g(t), \qquad 0 < t < c_3, \tag{A.35c}$$

where α_2, α_3, and β_1 are given in Eq. (A.20), and $g_1(t)$, $g_2(t)$, and $g(t)$ are regular functions of t.

A.3 Stress intensity factors and strain energy release rates

Since the dislocation functions, which are to be determined from the solution of the singular integral equations, are singular near the crack tips, the stresses around the crack tips are singular too. In fracture mechanics stress intensity factors are used to describe the singularities of stresses. It is well known that the stress intensity factors are related directly to the values of the functions $g_1(t)$, $g_2(t)$, $g_3(t)$ and $g_4(t)$ at the crack tips. The detailed derivation procedure can be found in [87]. It is thus very convenient to determine stress intensity factors from the solutions of the integral equations and then to determine strain energy release rates.

A.3.1 Stress intensity factors for the matrix crack

If $b_2 > a$, the crack is embedded in the matrix, and the stress intensity factors are defined as

$$k_1(b_2) = \lim_{r \to b_2^-} \sqrt{2(b_2 - r)}\sigma_{zz}^2(r,0) = a_2^{-\frac{1}{2}} g_2(b_2), \tag{A.36a}$$

$$k_1(c_2) = \lim_{r \to c_2^+} \sqrt{2(r - c_2)}\sigma_{zz}^2(r,0) = -a_2^{-\frac{1}{2}} g_2(c_2), \tag{A.36b}$$

where $a_2=(c_2-b_2)/2$.

If $b_2 = a$, $c_1 < a$ and $b_3 > 0$, that is, the inner crack tip terminates at the interface without intersecting another crack, the definitions of the stress intensity factors are

$$k_1(a) = \lim_{r \to a^-} \sqrt{2}(a - r)^{-\beta_2}\, \sigma_{zz}^1(r,0) = a_2^{-\frac{1}{2}} \mu^* g_2(a), \tag{A.37a}$$

$$k_1(c_2) = \lim_{r \to c_2^+} \sqrt{2(r - c_2)}\sigma_{zz}^2(r,0) = -2^{\frac{1}{2}+\beta_2} a_2^{\beta_2} g_2(c_2), \tag{A.37b}$$

where

$$\mu^* = \frac{\lambda(1+\kappa_2)[(1+\lambda\kappa_2)(3-2\beta_2) - (\lambda+\kappa_1)(1-2\beta_2)]}{2(\lambda+\kappa_1)(1+\lambda\kappa_2)\sin\pi\beta_2}. \tag{A.38}$$

If the inner matrix crack tip intersects another crack, the stress intensity factor defined for the outer matrix crack tip in Eq. (A.37b) is still valid.

A.3.2 Stress intensity factors for the fiber crack

If $c_1 < a$, the crack is embedded in the fiber, and the stress intensity factors are defined as

$$k_1(b_1) = \lim_{r \to b_1^-} \sqrt{2(b_1 - r)}\sigma_{zz}^1(r,0) = a_1^{-\frac{1}{2}} g_1(b_1), \tag{A.39a}$$

$$k_1(c_1) = \lim_{r \to c_1^+} \sqrt{2(r - c_1)}\sigma_{zz}^1(r,0) = -a_1^{-\frac{1}{2}} g_1(c_1), \tag{A.39b}$$

where a_1=(c_1-b_1)/2.

If $c_1 = a$, $b_2 > a$ and $b_3 > 0$, that is, the outer crack tip terminates at the interface without intersecting another crack, the definitions of the stress intensity factors are

$$k_1(b_1) = \lim_{r \to b_1^-} \sqrt{2(b_1 - r)}\sigma_{zz}^1(r,0) = 2^{\frac{1}{2}+\alpha_1} a_1^{\alpha_1} g_1(b_1), \tag{A.40a}$$

$$k_1(a) = \lim_{r \to a^+} \sqrt{2}(r-a)^{-\alpha_1} \sigma_{zz}^2(r,0) = -a_1^{-\frac{1}{2}} \mu^* g_1(a), \tag{A.40b}$$

where

$$\mu^* = \frac{1+\kappa_1[(1+\lambda\kappa_2)(1+2\alpha_1)-(\lambda+\kappa_1)(3+2\alpha_1)]}{2(\lambda+\kappa_1)(1+\lambda\kappa_2)\sin\pi\alpha_1}. \tag{A.41}$$

If the outer fiber crack tip intersects other cracks at the interface, the stress intensity factor for the inner fiber crack tip defined in Eq. (A.40b) remains valid.

A.3.3 Stress intensity factors for the interfacial crack

If b_3>0, the stress intensity factors are defined as

$$k_1(b_3) + ik_2(b_3) = \lim_{z \to b_3^-} (c_3 - z)^{-\alpha_3} (b_3 - z)^{-\beta_3} \left[\sigma_{rr}^2(a,z) + \sigma_{rz}^2(a,z)\right]$$

$$= a_{11}\sqrt{1-\gamma^2}\, g(b_3), \tag{A.42a}$$

$$k_1(c_3) + ik_2(c_3) = \lim_{z \to c_3^+} (z - c_3)^{-\alpha_3} (z - b_3)^{-\beta_3} \left[\sigma_{rr}^2(a,z) + \sigma_{rz}^2(a,z)\right]$$

$$= -a_{11}\sqrt{1-\gamma^2}\, g(c_3). \tag{A.42b}$$

If $b_3 = 0$, the two interface cracks are, for the convenience of numerical scheme, usually treated as one crack extended from $-c_3$ to $+c_3$. Thus the above definition, Eq. (A.42b) remains valid.

A.3.4 Strain energy release rates

Once the stress intensity factors are determined, the strain energy release rates can be easily calculated. As an example, the strain energy release rate for the outer matrix crack tip may be defined as

$$G_1(c_2) = \lim_{\delta \to 0} \frac{2\pi}{\delta} \int_{c_2}^{c_2+\delta} \sigma_z^2(r,0) u_z^2(r,0) r dr, \tag{A.43a}$$

which can be expressed as

$$G_1(c_2) = \frac{1+\kappa_2}{4\mu_2} \pi^2 c_2 k_1^2(c_2). \tag{A.43b}$$

Similar expressions can be readily obtained for other transverse crack tips, provided the tips are embedded into a homogeneous material. Following [72], the strain energy release rate for an interface crack tip can be expressed as

$$G_{12}(c_3) = \frac{\pi(\mu_1 + \kappa_1\mu_2)(\mu_2 + \kappa_2\mu_1)}{4a_3\mu_1\mu_2[(1+\kappa_2)\mu_1 + (1+\kappa_1)\mu_2]} \left[k_1^2(c_3) + k_2^2(c_3)\right], \tag{A.44}$$

where $a_3 = (c_3 - b_3)/2$.

A.4 Solution of singular integral equations

A.4.1 Normalization of singular integral equations

For the convenience of numerical solution the singular integral equations are normalized with the following change of variables:

For the matrix and fiber cracks

$$t = \frac{c_j + b_j}{2} + \frac{c_j - b_j}{2}\tau, \quad (j = 1,2), \qquad -1 < \tau < +1, \tag{A.45a}$$

$$r = \frac{c_j + b_j}{2} + \frac{c_j - b_j}{2}x, \quad (j = 1,2), \qquad -1 < x < +1, \tag{A.45b}$$

$$\varphi_1(t) = \phi_1(\tau), \ \varphi_2(t) = \phi_2(\tau), \qquad -1 < \tau < +1 \tag{A.45c}$$

For the interface crack,

$$t = \frac{c_3 + b_3}{2} + \frac{c_3 - b_3}{2}\tau, \qquad -1 < \tau < +1, \tag{A.46a}$$

$$z = \frac{c_3 + b_3}{2} + \frac{c_3 - b_3}{2}y, \qquad -1 < y < +1, \tag{A.46b}$$

if $b_3 = 0$,

$$t = c_3\tau, \qquad z = c_3 y, \qquad -1 < \tau, y < +1, \tag{A.46c}$$

$$\varphi_3(t) = \phi_3(\tau), \quad \varphi_4(t) = \phi_4(\tau) \qquad -1 < \tau < +1 \tag{A.46d}$$

After introducing $\phi(\tau) = \phi_1(\tau) + i\phi_2(\tau)$, where $i = \sqrt{-1}$, and combining Eqs (A.11c-d), the normalized integral equations can be written as

$$\frac{1}{\pi}\int_{-1}^{+1} \frac{\phi_1(\tau)}{\tau - x} d\tau + \int_{-1}^{+1} \left[l_{1c}\phi(\tau) + \overline{l_{1c}\phi(\tau)} + l_{11}\phi_1(\tau) + l_{12}\phi_4(\tau) \right] d\tau$$

$$= r_1(x), \quad -1 < x < +1, \tag{A.47a}$$

$$\frac{1}{\pi}\int_{-1}^{+1}\frac{\phi_2(\tau)}{\tau-x}d\tau+\int_{-1}^{+1}\left[l_{2c}\phi(\tau)+\overline{l_{2c}\phi(\tau)}+l_{21}\phi_1(\tau)+l_{22}\varphi_2(\tau)\right]d\tau$$

$$=r_2(x),\quad -1<x<+1, \tag{A.47b}$$

$$-\gamma\phi(y)+\frac{1}{\pi i}\int_{-1}^{+1}\frac{\phi(\tau)}{\tau-y}d\tau+\int_{-1}^{+1}\left[l_{cr}\phi(\tau)+l_{ci}\overline{\phi(\tau)}+l_{c1}\varphi_1(\tau)+l_{c2}\phi_2(\tau)\right]d\tau$$

$$=r_4(y)-ir_3(y),\quad -1<y<+1, \tag{A.47c}$$

where

$$l_{cr}=\frac{1}{2}[l_{43}-l_{34}-i(l_{33}+l_{44})],\quad l_{ci}=\frac{1}{2}[l_{43}+l_{34}-i(l_{33}-l_{44})],$$
$$l_{cj}=l_{4j}-il_{3j},\qquad l_{jc}=\frac{1}{2}(l_{j3}-il_{j4}),\ (j=1,2), \tag{A.48a}$$

$$l_{mj}=\frac{c_j-b_j}{\pi\gamma_{11}}k_{mj},\ (m=3,4),\quad l_{nj}=\frac{c_j-b_j}{\pi}k_{nj},\ (n=1,2,\ j=1,\ldots,4), \tag{A.48b}$$

$$r_j=-p_j,\ (j=1,2), r_n=(-1)^n\frac{p_n}{\gamma_{11}},\quad (n=3,4), \tag{A.48c}$$

if $b_3=b_4>0$,

$$l_{jj}=\frac{c_3-b_3}{\pi\gamma_{11}}k_{jj}-\frac{(-1)^j}{\tau+y+c},\ (j=3,4),\ c=2\frac{c_3+b_3}{c_3-b_3}. \tag{A.48d}$$

A.4.2 Numerical solution of Cauchy singular integral equations for embedded cracks

It may be noticed that the first and second equations are singular integral equations of the first kind, while the third one is a complex singular integral equation of the second kind. Different numerical procedures should be used to solve two different kinds of equations.

The functions $\phi_1(\tau)$, $\phi_2(\tau)$ and $\phi(\tau)$ have the following forms:

$$\phi_1(\tau) = (1-\tau)^{\alpha_1}(1+\tau)^{\beta_1} f_1(\tau) = W_1(\tau) f_1(\tau), \qquad -1 < \alpha_1, \beta_1 \le 0, \tag{A.49a}$$

$$\phi_2(\tau) = (1-\tau)^{\alpha_2}(1+\tau)^{\beta_2} f_2(\tau) = W_2(\tau) f_2(\tau), \qquad -1 < \alpha_2, \beta_2 \le 0, \tag{A.49b}$$

$$\phi(\tau) = (1-\tau)^{\alpha_3}(1+\tau)^{\beta_3} f_c(\tau) = W_3(\tau) f_c(\tau), \qquad -1 < \mathrm{Re}(\alpha_3, \beta_3) \le 0, \tag{A.49c}$$

where α_1, β_1, α_2, β_2, α_3, and β_3 were given before, and $f_1(\tau)$, $f_2(\tau)$ and $f_c(\tau)$ are regular functions. Following the procedure described in [87], $\phi(\tau)$ may be approximated by Jacobi polynomials as

$$\phi(\tau) \cong W_3(\tau) \sum_{j=0}^{N_3} c_j P_j^{(\alpha_3,\beta_3)}(\tau), \tag{A.50}$$

where $c_0, c_1, \ldots c_{N_3}$ are complex coefficients. Using the property of Jacobi polynomials:

$$-\gamma P_j^{(\alpha,\beta)}(y) W(y) + \frac{1}{\pi i} \int_{-1}^{+1} W(\tau) P_j^{(\alpha,\beta)}(\tau) \frac{d\tau}{\tau - y}$$

$$= \frac{1}{2i} \sqrt{1-\gamma^2}\, P_{j-1}^{(-\alpha,-\beta)}(y), \qquad -1<y<+1, \tag{A.51}$$

and the Lobatto-Jacobi quadrature for the integrals involving $\phi_1(\tau)$ and $\phi_2(\tau)$ the integral equations (A.47a-c) can be approximated as

$$\sum_{k_1=1}^{N_1} A_{k_1} \left[\frac{1}{\pi(\tau_{k_1} - x)} + l_{11}(x, \tau_{k_1}) \right] f_1(\tau_{k_1})$$

$$+ \sum_{k_2=1}^{N_2} A_{k_2} l_{12}(x, \tau_{k_2}) f_2(\tau_{k_2})$$

$$+ \sum_{j=0}^{N_3} \left[c_j \int_{-1}^{+1} l_{1c}(x,\tau) W_3(\tau) P_j^{(\alpha_3,\beta_3)}(\tau) d\tau + \overline{c_j} \int_{-1}^{+1} \overline{l_{1c}(x,\tau) W_3(\tau)}\, \overline{P_j^{(\alpha_3,\beta_3)}(\tau)} d\tau \right]$$

$$= r_1(x), \qquad -1 < x < +1, \tag{A.52a}$$

$$\sum_{k_2=1}^{N_2} A_{k_2}\left[\frac{1}{\pi(\tau_{k_2}-x)} + l_{22}(x,\tau_{k_2})\right] f_2(\tau_{k_2}) + \sum_{k_1=1}^{N_1} A_{k_1} l_{21}(x,\tau_{k_1}) f_2(\tau_{k_1})$$

$$+\sum_{j=0}^{N_3}\left[c_j \int_{-1}^{+1} l_{2c}(x,\tau) W_3(\tau) P_j^{(\alpha_3,\beta_3)}(\tau) d\tau + \overline{c_j} \int_{-1}^{+1} \overline{l_{2c}(x,\tau) W_3(\tau)}\, \overline{P_j^{(\alpha_3,\beta_3)}(\tau)} d\tau\right]$$

$$= r_2(x), \qquad -1 < x < +1, \tag{A.52b}$$

$$\frac{\sqrt{1-\gamma^2}}{2i} \sum_{j=0}^{N_3} c_j P_{j-1}^{(-\alpha_3,-\beta_3)}(y)$$

$$+\sum_{j=0}^{N_3} \int_{-1}^{+1}\left[c_j l_{cr} W_3(\tau) P_j^{(\alpha_3,\beta_3)}(\tau) + \overline{c_j} l_{ci}\, \overline{W_3(\tau)}\, \overline{P_j^{(\alpha_3,\beta_3)}}\right] d\tau$$

$$+\sum_{k_1=1}^{N_1} A_{k_1} l_{c1}(y,\tau_{k_1}) f_1(\tau_{k_1}) + \sum_{k_2=1}^{N_2} A_{k_2} l_{c2}(y,\tau_{k_2}) f_2(\tau_{k_2})$$

$$= r_4(y) - i r_3(y), \quad -1 < y < +1, \tag{A.52c}$$

where τ_{ki} and A_{ki} are the abscissa and weight coefficients of the quadrature, respectively. In the above equations there are N_1 discrete values of $f_1(\tau)$, N_2 discrete values of $f_2(\tau)$, and N_3+1 complex coefficients c_j ($j = 0, 1, \ldots, N_3$), and therefore a total of $N_1+N_2+2N_3+2$ real algebraic equations is required to determine them.

(*a*) *Integrals involving transverse crack dislocations*: When the fiber and matrix cracks are away from the interface, $\alpha_1 = \beta_1 = \alpha_2 = \beta_2 = -1/2$, and the corresponding quadrature is defined by [89]:

$$\int_{-1}^{+1} \frac{f(t)dt}{\sqrt{1-t^2}} = \sum_{k_i=1}^{N_i} A_{k_i} f(t_{k_i}), \quad (i=1,2), \tag{A.53a}$$

where

$$\tau_{k_i} = -\cos\left[\frac{(k_i-1)\pi}{N_i-1}\right], \ (k_i = 1,2,\ldots,N_i), \ A_{k_i} = \begin{cases} \frac{\pi}{2(N_i-1)}, & k_i = 1, \ N_i \\ \frac{\pi}{N_i-1}, & k_i = 2,3,\ldots,N_i-1 \end{cases}. \tag{A.53b}$$

In order for the integral formula to be valid for evaluating the Cauchy singular integrals, the collocation points must be chosen as [89]:

$$x_{m_i} = -\cos\left[\frac{(2m_i-1)\pi}{2(N_i-1)}\right], \qquad m_i = 1,2,\ldots,N_i-1. \tag{A.54}$$

Now (N_1+N_2-2) equations can be obtained from Eqs (A.52a-b) as

$$\sum_{k_1=1}^{N_1} A_{k_1}\left[\frac{1}{\pi(\tau_{k_1}-x_{m_1})} + l_{11}(x_{m_1},\tau_{k_1})\right] f_1(\tau_{k_1})$$

$$+\sum_{k_2=1}^{N_2} A_{k_2} l_{12}(x_{m_1},\tau_{k_2}) f_2(\tau_{k_2}) + \sum_{j=0}^{N_3} c_j \int_{-1}^{+1} l_{1c}(x_{m_1},\tau) W_3(\tau) P_j^{(\alpha_3,\beta_3)}(\tau) d\tau$$

$$+\sum_{j=0}^{N_3} \overline{c_j} \int_{-1}^{+1} \overline{l_{2c}(x_{m_1},\tau) W_3(\tau) P_j^{(\alpha_3,\beta_3)}(\tau)} d\tau = r_1(x_{m_1}), \ m_1 = 1,2,\ldots,N_1-1, \tag{A.55a}$$

$$\sum_{k_2=1}^{N_2} A_{k_2}\left[\frac{1}{\pi(\tau_{k_2}-x_{m_2})} + l_{22}(x_{m_2},\tau_{k_2})\right] f_2(\tau_{k_2})$$

$$+\sum_{k_1=1}^{N_1} A_{k_1} l_{21}(x_{m_2},\tau_{k_1}) f_1(\tau_{k_1}) + \sum_{j=0}^{N_3} c_j \int_{-1}^{+1} l_{2c}(x_{m_2},\tau) W_3(\tau) P_j^{(\alpha_3,\beta_3)}(\tau) d\tau$$

$$+\sum_{j=0}^{N_3} \overline{c_j} \int_{-1}^{+1} \overline{l_{2c}(x_{m_2},\tau) W_3(\tau) P_j^{(\alpha_3,\beta_3)}(\tau)} d\tau = r_2(x_{m_2}), \ m_2 = 1,2,\ldots,N_2-1, \tag{A.55b}$$

After the integrals in the left side are evaluated, the above equations are simple algebraic equations. Since similar integrals, which are more complicated, are also involved in Eq. (A.52c), we must treat these integrals first.

(b) *Integrals involving interface crack dislocations*: It is worth discussing the behaviors of some kernels briefly before handling these integrals. In what follows the attention will be focused on a special interfacial crack, but the conclusions are generally valid. For a single interface crack ($b_3 = 0$), two typical kernels can be expressed as

$$k_{33}(z,t) = \int_0^\infty K_{33}(s)\sin(t-z)sds, \tag{A.56a}$$

$$k_{34}(z,t) = \int_0^\infty K_{34}(s)\cos(t-z)sds. \tag{A.56b}$$

It can be shown that

$$K_{33}(s) = O(\tfrac{1}{s}), \qquad K_{34}(s) = O(\tfrac{1}{s}), \quad \text{as s} \to +\infty. \tag{A.57}$$

Obviously, $k_{33}(z, t)$ is discontinuous at $t = z$, while $k_{34}(z, t)$ is logarithmically singular at $t = z$, if both are considered as functions of t with a parameter z. The same is true for kernels k_{43} and k_{44}.

A typical integral involving one of these kernels can be represented by

$$\int_{-1}^{+1} l(y,\tau) P_j^{(\alpha_3,\beta_3)}(\tau) \frac{1}{\sqrt{1-\tau^2}} \left(\frac{1+\tau}{1-\tau}\right)^{i\omega} d\tau, \tag{A.58}$$

where $l(y, \tau)$ is a normalized kernel. It seems very easy to evaluate the integral, if the factor $(1-\tau^2)^{-1/2}$ is used to construct the Gauss-Chebyshev quadrature, and the oscillating factor $[(1+\tau)/(1-\tau)]^{i\omega}$ is treated as a common function as in Ref. [86].

However the author found that it does not work even for the simplest case where the integrand consists of only these two factors. For the cases where $l(y,\tau)$ has discontinuities or logarithmic singularities, much finer treatment must be used.

If a transformation

$$u = \log\left|\frac{1+\tau}{1-\tau}\right|, \qquad or \quad \tau = \frac{e^u - 1}{e^u + 1}, \tag{A.59}$$

is introduced, the integral can be transformed into

$$\int_{-\infty}^{+\infty} \frac{1}{2\cosh(\frac{u}{2})} l(y,\tau(u)) P_j^{(\alpha_3,\beta_3)}(\tau(u))(\cos\omega u + i\sin\omega u)du. \tag{A.60}$$

It should be pointed out that as $u \to \pm\infty$, $1/\cosh(u/2) = O(e^{-|u/2|})$, which decays very quickly, and thus finite integral limits may be used to replace the infinite ones. Since the material constant ω is much less than one for usual material combinations, the oscillations from two circular functions are very weak. Therefore it is not difficult to calculate the integral accurately. This procedure is equally useful for all integrals involving $W_3(\tau)$ and $\overline{W_3(\tau)}$. For the integrals involving l_{cr} and l_{ci} which are combinations of discontinuous or weakly singular kernels k_{ij} ($i, j = 3, 4$), the integral ranges should be subdivided into smaller ranges, and the integrals can then be evaluated by using simple Gauss quadrature in each range.

The equation (A.52c) can now be reduced into algebraic equations using the weighted residual method. The weight functions used in [86, 87] are

$$(1-y)^{-\alpha_3}(1+y)^{-\beta_3} P_n^{(-\alpha_3,-\beta_3)}(y), \qquad n = 0, 1, \ldots, N_3 - 1. \tag{A.61}$$

After multiplying both sides of the equation by the above weight functions, and then integrating them with respect to y over range (–1, +1), one obtains a set of algebraic

equations. Since the first term in the left hand side of the equation is in the form of Jacobi polynomial series, the orthogonality relation of the polynomials could be used to simplify the calculations. It is, however, not easy to calculate all the other terms accurately because of the oscillatory behavior in the weight functions.

It is not difficult to realize that the above method is equivalent to approximating both sides of Eq. (A.52c) in terms of Jacobi polynomials. If the method works, or in other words, if the Jacobi polynomials are good approximations of both sides of the equation, other polynomials should work well too. Based on this reasoning, simple Chebyshev polynomials of the first kind are used as the weight functions in this study:

$$w_n(y) = \frac{1}{\sqrt{1-y^2}} T_n(y), \qquad n = 1, 2, \ldots, N_1 - 1. \tag{A.62}$$

Now the reduced algebraic equations may be expressed as

$$\frac{\sqrt{1-\gamma^2}}{2i} \sum_{j=0}^{N_3} c_j \int_{-1}^{+1} w_n(y) P_{j-1}^{(-\alpha_3,-\beta_3)}(y)dy + \sum_{j=0}^{N_3} c_j \int_{-1}^{+1} w_n(y) \left[\int_{-1}^{+1} l_{cr}(y,\tau) W_3(\tau) P_j^{(\alpha_3,\beta_3)}(\tau)d\tau \right] dy$$

$$+ \sum_{j=0}^{N_3} \overline{c_j} \int_{-1}^{+1} w_n(y) \left[\int_{-1}^{+1} l_{ci}(y,\tau) \overline{W_3(\tau)} \overline{P_j^{(\alpha_3,\beta_3)}(\tau)}d\tau \right] dy + \sum_{k_1=1}^{N_1} A_{k_1} f_1(\tau_{k_1}) \int_{-1}^{+1} w_n(y) l_{c1}(y,\tau_{k_1})dy$$

$$+ \sum_{k_2=1}^{N_2} A_{k_2} f_2(\tau_{k_2}) \int_{-1}^{+1} W_n(y) l_{c2}(y,\tau_{k_2})dy$$

$$= \int_{-1}^{+1} w_n(y)[r_4(y) - ir_3(y)]\, dy, \quad n = 0, 1, \ldots, N_3 - 1, \tag{A.63}$$

where all integrals with respect to y can be calculated using the following simple Gauss Chebyshev quadrature:

$$\int_{-1}^{+1}(1-y^2)^{-\frac{1}{2}}P(y)dy=\frac{\pi}{n}\sum_{i=1}^{n}P(y_i),\quad i=\cos\frac{\pi(2i-1)}{2n}. \tag{A.64}$$

Now $N_1 + N_2 + 2N_3 - 2$ real equations are provided in Eqs (A.55a-b) and (A.63), and considering the single-valuedness of displacements, one can obtain the remaining four equations:

$$\int_{-1}^{+1}\phi_1(\tau)d\tau=0,\quad \int_{-1}^{+1}\phi_2(\tau)d\tau=0,\quad \int_{-1}^{+1}\phi(\tau)d\tau=0\ , \tag{A.65}$$

which can be expressed as:

$$\sum_{k1=1}^{N_1}A_{k1}f_1(\tau_{k1})=0,\quad \sum_{k2=1}^{N_2}A_{k2}f_2(\tau_{k2})=0\qquad c_0=0\ . \tag{A.66}$$

Solving Eqs (A.55), (A.63) and (A.66) determines the $N_1 + N_2 + 2N_3 + 2$ unknowns uniquely.

A.4.3 Numerical solution of singular integral equations with generalized Cauchy kernels

(*a*) *Matrix crack terminating at the interface but without intersecting another crack*: When the inner matrix crack tip is terminated at the interface, k_{22} will exhibit singular behavior. In addition to the procedure discussed above some particular numerical schemes must be used. Although the integral equations with generalized Cauchy kernels were investigated previously [85-87], the effort was only limited to the determination of the power of singularity, with no particular attention being paid to their numerical solution. As commented in [90], the method used in the above studies was not fully justified. The convergence problems were encountered in solving such systems. Detailed

discussions can be found in [90-92] on the proper treatment of the generalized Cauchy kernels. In this study, the author follows the treatment for general Cauchy kernels given in [92, 93].

The dominant part of the singular integral equation (A.47b), in this case, may be expressed as

$$\frac{1}{\pi}\int_{-1}^{+1}\frac{W_2(\tau)g_2(\tau)}{\tau-x}d\tau$$

$$+\frac{1}{\pi}\int_{-1}^{+1}\sqrt{\frac{t}{r}}\left[\frac{c_{20}}{(\tau+x+2)}+\frac{c_{21}(x+1)}{(\tau+x+2)^2}+\frac{c_{22}(x+1)^2}{(\tau+x+2)^3}\right]W_2(\tau)g_2(\tau)d\tau, \qquad \text{(A.67)}$$

where t and r are non-normalized variables, $W_2(\tau)=(1-\tau)^{\alpha_2}(1+\tau)^{\beta_2}$, $\alpha_2=-1/2$, and β_2 is to be determined from Eq. (A.22b).

If the Lobatto-Jacobi quadrature is used to calculate singular integrals given in Eq. (A.67), the following formulas can be readily derived [90, 93, 94]:

$$\int_{-1}^{+1}\frac{W_2(\tau)g_2(\tau)d\tau}{\tau-x}=\sum_{i=1}^{N}\frac{A_i g_2(\tau_i)}{\tau_i-x}-g_2(x)K_N(x), \qquad \text{(A.68a)}$$

$$\int_{-1}^{+1}\frac{W_2(\tau)g_2(\tau)d\tau}{(\tau-x)^2}=\sum_{i=1}^{N}\frac{A_i g_2(\tau_i)}{(\tau_i-x)^2}-\frac{d}{dz}\left(g_2(z)K_N(z)\right)_{z=x}, \qquad \text{(A.68b)}$$

$$\int_{-1}^{+1}\frac{W_2(\tau)g_2(\tau)d\tau}{(\tau-x)^3}=\sum_{i=1}^{N}\frac{A_i g_2(\tau_i)}{(\tau_i-x)^3}-\frac{1}{2}\frac{d^2}{dz^2}\left(g_2(z)K_N(z)\right)_{z=x}, \qquad \text{(A.68c)}$$

where τ_i (i=1, 2, ..., N) are the roots of the polynomial

$$\sigma_N(\tau)=\left(1-\tau^2\right)P_{N-2}^{(\alpha_2+1,\beta_2+1)}(\tau), \qquad \text{(A.69a)}$$

A_i (i = 1, 2, ..., N) are given by

$$A_i = -\frac{q_N(\tau_i)}{\sigma'_N(\tau_i)}, \qquad q_N(\tau) = \int_{-1}^{+1} W_2(t)\frac{\sigma_N(t)}{\tau - t}dt, \tag{A.69b}$$

and

$$K_N(z) = \frac{q_N(z)}{\sigma_N(z)}. \tag{A.69c}$$

The integrals in Eq. (A.67) can now be calculated as

$$\frac{1}{\pi}\sum_{i=1}^{N_2}\frac{A_i g_2(\tau_i)}{\tau_i - x} + \frac{1}{\pi}\sum_{i=1}^{N_2} A_i\sqrt{\frac{t_i}{r}}\left[\frac{c_{20}}{\tau_i + x + 2} + \frac{c_{21}(x+1)}{(\tau_i + x + 2)^2} + \frac{c_{22}(x+1)^2}{(\tau_i + x + 2)^3}\right]g_3(\tau_i)$$

$$-\frac{1}{\pi}g_2(x)K_{N_2}(x) - \frac{1}{\pi\sqrt{r}}\left[c_{20}\sqrt{t}\,g_2(\tau)K_{N_2}(\tau)\right]_{\tau=-(x+2)}$$

$$-\frac{1}{\pi\sqrt{r}}\left[c_{21}(x+1)\left(\sqrt{t}\,g_2(\tau)K_{N_2}(\tau)\right)' + \frac{c_{22}(x+1)^2}{2}\left(\sqrt{t}\,g_2(\tau)K_{N_2}(\tau)\right)''\right]_{\tau=-(x+2)}. \tag{A.70}$$

If the N_2-1 roots of $K_{N_2}(x)$ are chosen as the collocation points, the error term in the Cauchy integral will vanish, but the error from the generalized part does not. This error in general is not negligible. It has been shown in [90] that its value will become considerable when a collocation point is very close to x=—1. Actually, according to the numerical results of [92, 93] and our experience, considering the error from the first collocation point x_1 which is nearest to x=—1 is good enough. Thus, if the approximations are made on $g_3(\tau)$ so that $g_3[-(x_1+2)] \cong g_3(-1)$, $g_3'[-(x_1+2)] \cong g_3'(-1)$ and $g_3''[-(x_1+2)] \cong g_3''(-1)$, the error from the generalized part may be reduced to the calculations of the hypergeometric functions [91] and can be counted in the integrals. The complementary equations (A.65) are still valid for this case.

(b) *A transverse crack intersecting the interface crack (T-shaped crack):* When the matrix crack or fiber crack connects with the interface crack while another transverse crack being away from the interface, the two connecting cracks form a T-shaped crack. As discussed before, the integral equations corresponding to these two cracks have generalized kernels in this case. Particular attention should be paid to the treatment of these integrals. Since the same procedure as discussed in Case (a) can be used for this case except that the singular power at the intersecting tip is zero now, further discussion seems unnecessary.

Also four complementary conditions are required to insure the uniqueness of the solution. For the case of the matrix crack intersecting the interface crack, one of these conditions is given before in Eq. (A.29), and the other three conditions can be obtained by considering the deformation compatibility. The four conditions are:

$$\frac{\lambda(1+k_2)}{2}(c_2-a)^{\alpha_2} g_2(a) + g_3(0)c_3^{\alpha_3} = 0, \tag{A.71a}$$

$$\int_{-c_3}^{+c_3} \varphi_3(t)dt = 0, \tag{A.71b}$$

$$\frac{\lambda(1+\kappa_2)}{2}\int_a^{c_2} \varphi_2(t)dt - \int_0^{c_3} \varphi_3(t)dt = 0, \tag{A.71c}$$

$$\int_{b_1}^{c_1} \varphi_1(t)dt = 0. \tag{A.71d}$$

For the case of the fiber crack intersecting the interface crack, the similar four conditions are:

$$\frac{1+\kappa_1}{2}(a-b_1)^{\beta_1} g_1(a) - g_3(0)c_3^{\alpha_3} = 0. \tag{A.72a}$$

$$\int_{-c_3}^{+c_3}\varphi_3(t)dt = 0, \tag{A.72b}$$

$$\frac{1+\kappa_1}{2}\int_{b_1}^{a}\varphi_1(t)dt - \int_{0}^{c_3}\varphi_4(t)dt = 0\ , \tag{A.72c}$$

$$\int_{b_2}^{c_2}\varphi_2(t)dt = 0. \tag{A.72d}$$

It must be pointed out that, when the interface crack is extended from $-c_1$ to $+c_1$, $g_3(0)$ is equal to zero automatically because of the antisymmetry of φ_3. Therefore, in order for Eq. (A.71a) or Eq. (A.72a) to be satisfied $g_2(a)$ or $g_1(a)$ must be equal to zero too. In general, this may not be the case. However, if the two intersecting cracks are not very short and the behaviors at the remote two crack tips are the main concern, the treatment seems reasonable. In [95] for the convenience of constructing the integral quadrature formula, the author used a singular power of $-1/2$ instead of the real power of zero, and then he had to let the value of the regular part of the dislocation for the connecting transverse crack be zero at the connecting tip. The author's using unrealistic singular power may supply some compensation on the "zero-assumption".

(c) *Intersection of the fiber, matrix and interface cracks at the interface*: In this case each of the singular integral equations has generalized Cauchy kernels, and the integrals containing these kernels can be treated using the numerical schemes discussed above. The procedure for the T-shaped cracks are also applicable to this case.

Two of the four additional conditions are:

$$\int_{b_2}^{c_2} \varphi_2(t)dt = 0 \quad , \tag{A.73a}$$

$$\frac{1+\kappa_1}{2}\int_{b_1}^{a} \varphi_1(t)dt + \frac{\lambda(1+\kappa_2)}{2}\int_{a}^{c_2} \varphi_2(t)dt - \int_{0}^{c_3} \varphi_4(t)dt = 0 \ , \tag{A.73b}$$

and the remaining two are obtained by considering the non-singular behavior at the common crack tip, where no singularity occurs. For the same reason as discussed above, the conditions $g_1(a) = g_2(a) = 0$ can be used instead.

Once the dislocation functions are determined, the stress intensity factors can be evaluated easily, and all displacement and stress components can also be calculated by using the integral formulas described in Section A.2.

Appendix B

Elastic Constants of a Fiber-Reinforced Composite [74-76]

$$E_{31} = E_f V_f + E_m V_m + \frac{4V_f V_m (\nu_f - \nu_m)^2}{\frac{V_m}{k_f} + \frac{V_f}{k_m} + \frac{1}{G_m}},$$

$$E_{32} = \frac{4k_t^* G_t^*}{k_t^* + G_t^* \left(1 + \frac{4k_t^* \nu_{31}^2}{E_{31}}\right)},$$

$$\nu_{31} = \nu_f V_f + \nu_m V_m + \frac{V_f V_m (\nu_f - \nu_m)(\frac{1}{k_m} - \frac{1}{k_f})}{\frac{V_m}{k_f} + \frac{V_f}{k_m} + \frac{1}{G_m}}, \qquad \text{(B.1)}$$

$$G_{32} = G_m \frac{V_m G_m + (1 + V_f) G_f}{(1 + V_f) G_m + V_m G_f},$$

$$\nu_{32} = \frac{E_{22}}{2G_t^*} - 1,$$

where

$$k_f = E_f / 2(1 - \nu_f - \nu_f^2),$$

$$k_m = E_m / 2(1 - \nu_m - \nu_m^2),$$

$$k_t^* = \frac{k_m k_f + (V_f k_f + V_m k_m) G_m}{V_f k_m + V_m k_f + G_m}, \qquad \text{(B.2)}$$

$$G_t^* = G_m \frac{(\alpha + \beta_m V_f)(1 + \rho V_f^3) - 3V_f V_m^2 \beta_m^2}{(\alpha - V_f)(1 + \rho V_f^3) - 3V_f V_m^2 \beta_m^2},$$

$$\alpha = (\gamma + \beta_m)/(\gamma - 1),$$

$$\beta_m = \frac{1}{3-4\nu_m}, \qquad \beta_f = \frac{1}{3-4\nu_f},$$

$$\rho = (\beta_m - \gamma\beta_f)/(1 + \gamma\beta_f), \tag{B.3}$$

$$\gamma = G_f / G_m,$$

where V_f and V_m are volume fractions of the fiber and matrix, respectively, and the subscripts f and m are referred to the fiber and matrix, respectively.

Appendix C

Formulation of the Three-Cylinder Problem with a Single Matrix Crack

C.1 Displacement and stress fields

The displacement and stress fields for the fiber are the same as those derived in Appendix A. For the matrix, from Love's stress function Eq. (3.13) the displacement and stress components can also easily be derived as follows [51]:

$$u_r^2(r,z) = \frac{-1}{2\mu_2}\frac{2}{\pi}\int_0^\infty [f_3(s)I_1(rs) + f_4(s)rsI_0(rs) - f_5(s)K_1(rs)$$

$$-f_6(s)rsK_0(rs)]s^2\cos(zs)ds + \frac{1}{2\mu_2}\int_0^\infty g_0(p)p^3(1-2\nu_2-zp)e^{-zp}J_1(rp)dp, \qquad \text{(C.1a)}$$

$$u_z^2(r,z) = \frac{1}{2\mu_2}\frac{2}{\pi}\int_0^\infty \{f_3(s)I_0(rs) + f_4(s)[4(1-\nu_2)I_0(rs) + rsI_1(rs)]$$

$$+ f_5(s)K_0(rs) + f_6(s)[-4(1-\nu_2)K_0(rs) + rsK_1(rs)]\}s^2\sin(zs)ds$$

$$-\frac{1}{2\mu_2}\int_0^\infty g_0(p)p^3[2(1-\nu_2)+zp)]e^{-zp}J_0(rp)dp, \qquad \text{(C.1b)}$$

$$\sigma_{rr}^2(r,z) = \frac{2}{\pi}\int_0^\infty \{f_3(s)[-I_0(rs) + I_1(rs)/rs] + f_4(s)[(2\nu_2-1)I_0(rs) - rsI_1(rs)]$$

$$-f_5(s)[K_0(rs) + K_1(rs)/rs] + f_6(s)[(1-2\nu_2)K_0(rs) - rsK_1(rs)]\}s^3\cos(zs)ds$$

$$+\int_0^\infty g_0(p)p^4[(1-zp)J_0(rp) - (1-2\nu_2-zp)J_1(rp)/rp]e^{-zp}dp, \qquad \text{(C.1c)}$$

$$\sigma_{zz}^2(r,z)=\frac{2}{\pi}\int_0^\infty\{f_3(s)I_0(rs)+f_4(s)[2(2-\nu_2)I_0(rs)+rsI_1(rs)]$$

$$+f_5(s)K_0(rs)+f_6(s)[-2(2-\nu_2)K_0(rs)+rsK_1(rs)]\}s^3\cos(zs)ds$$

$$+\int_0^\infty g_0(p)p^4(1+zp)J_0(rp)e^{-zp}dp, \qquad \text{(C.1d)}$$

$$\tau_{rz}^2(r,z)=\frac{2}{\pi}\int_0^\infty\{f_3(s)I_1(rs)+f_4(s)[rsI_0(rs)+2(1-\nu_2)I_1(rs)]$$

$$-f_5(s)K_1(rs)+f_6(s)[-rsK_0(rs)+2(1-\nu_2)K_1(rs)]\}s^3\sin(zs)ds$$

$$+\int_0^\infty g_0(p)p^5zJ_1(rp)e^{-zp}dp. \qquad \text{(C.1e)}$$

Using formulas in Eqs (3.14) and (3.16), the displacement and stress fields can also be derived readily from the stress function Eq. (3.21) for the transversely isotropic composite medium. The following four expressions are required in deriving the singular integral equations:

$$u_r^3=\frac{2e}{\pi}\int_0^\infty\left[f_7(s)\frac{s}{s_1}K_1(rs/s_1)+f_8(s)\frac{s}{s_2}K_1(rs/s_2)\right]s\cos(zs)ds, \qquad \text{(C.2a)}$$

$$u_z^3=\frac{2}{\pi}\int_0^\infty\{f_7(s)[a_{44}/s_1^2-(a_{44}+g)]K_0(rs/s_1)$$

$$+f_8(s)[a_{44}/s_2^2-(a_{44}+g)]K_0(rs/s_2)\}s^2\sin(zs)ds, \qquad \text{(C.2b)}$$

$$\sigma_{rr}^3=-\frac{2}{\pi}\int_0^\infty\{[f_7(s)[(s/s_1)^2-a_cs^2]K_0(rs/s_1)+(1-b_c)(s/rs_1)K_1(rs/s_1)]$$

$$+f_8(s)[[(s/s_2)^2-a_cs^2]K_0(rs/s_2)+(1-b_c)(s/rs_2)K_1(rs/s_2)]\}s\cos(zs)ds, \qquad \text{(C.2c)}$$

$$\tau_{rz}^3=\frac{2}{\pi}\int_0^\infty[f_7(s)(a_c/s_1-1/s_1^3)K_1(rs/s_1)$$

$$+f_8(s)(a_c/s_2 - 1/s_2^3)K_1(rs/s_2)\Big]s^3\sin(zs)ds\,. \qquad \text{(C.2d)}$$

C.2 Boundary and continuity conditions

The boundary and continuity conditions at the fiber/matrix interface are:

$$u_r^1(a,z) = u_r^2(a,z), \qquad c_3 < z < \infty, \qquad \text{(C.3a)}$$

$$\sigma_{rr}^1(a,z) = \sigma_{rr}^2(a,z), \qquad 0 \le z < \infty, \qquad \text{(C.3b)}$$

$$\sigma_{rr}^1(a,z) = \sigma_{rr}^2(a,z) = -p_3(z), \qquad 0 \le z < c_3, \qquad \text{(C.3c)}$$

$$u_z^1(a,z) = u_z^2(a,z), \qquad c_3 < z < \infty, \qquad \text{(C.3d)}$$

$$\tau_{rz}^1(a,z) = \tau_{rz}^2(a,z), \qquad 0 \le z < \infty, \qquad \text{(C.3e)}$$

$$\tau_{rz}^1(a,z) = \tau_{rz}^2(a,z) = p_4(z), \qquad 0 \le z < c_3. \qquad \text{(C.3f)}$$

At the matrix/composite interface four conditions are given by:

$$u_r^2(R,z) = u_r^3(R,z), \qquad 0 \le z < \infty, \qquad \text{(C.4a)}$$

$$\sigma_{rr}^2(R,z) = \sigma_{rr}^3(R,z), \qquad 0 \le z < \infty, \qquad \text{(C.4b)}$$

$$\tau_{rz}^2(R,z) = \tau_{rz}^3(R,z) = 0, \qquad 0 \le z < \infty. \qquad \text{(C.4c)}$$

Also at z = 0 plane the boundary and symmetry conditions are:

$$u_z^1(r,0) = 0, \qquad 0 \le r < a, \qquad \text{(C.5a)}$$

$$\tau_{rz}^1(r,0) = 0, \qquad 0 \le r < a, \qquad \text{(C.5b)}$$

$$\tau_{rz}^2(r,0) = 0, \qquad a < r < R, \qquad \text{(C.6a)}$$

$$\sigma_{zz}^2(r,0) = -p_2(r), \qquad a < r < R, \qquad \text{(C.6b)}$$

$$u_z^3(r,0) = 0, \qquad R \le r < \infty, \qquad \text{(C.7)}$$

$$\tau^3_{rz}(r,0) = 0, \qquad R \le r < \infty, \tag{C.8}$$

where p_i (i=2,...,4) are the tractions on crack surfaces.

C.3 Derivation of the singular integral equations

Using the three dislocation functions defined in Eq. (3.22), and following the same procedure used in Appendix A, one can easily show that

$$f_0(p) = 0, \tag{C.9a}$$

$$g_0(p) = \frac{1}{p^3}\int_a^R r\varphi_1(r)J_1(rp)dr, \tag{C.9b}$$

and the remaining eight unknowns f_j (j = 1, ..., 8) can be determined from solving a set of eight algebraic equations:

$$\sum_{j=1}^{8} A_{ij}(s)f_j(s) = R_i(s), \quad (i = 1,...,8) \ . \tag{C.10}$$

The coefficients A_{ij} are can be expressed as:

$$A_{11} = -I_0(as) + I_1(as)/as, \ A_{12} = 2(1-\nu_1)asI_0(as),$$

$$A_{13} = I_0(as) - I_1(as)/as, \ A_{14} = (1-2\nu_2)I_0(as) + asI_1(as),$$

$$A_{15} = K_0(as) + K_1(as)/as, \ A_{16} = -(1-2\nu_2)K_0(as) + asK_1(as),$$

$$A_{17} = 0, \ A_{18} = 0,$$

$$A_{21} = I_1(as), \ A_{22} = 2(1-\nu_1)I_1(as),$$

$$A_{23} = -I_1(as), \ A_{24} = -[2(1-\nu_2)I_1(as) + asI_0(as)],$$

$$A_{25} = K_1(as), \ A_{26} = asK_0(as) - 2(1-\nu_2)K_1(as)],$$

$$A_{27} = 0, \ A_{28} = 0,$$

$$A_{31} = -I_1(as),\ A_{32} = -asI_0(as),$$

$$A_{33} = \lambda I_1(as),\ A_{34} = \lambda asI_0(as),$$

$$A_{35} = -\lambda K_1(as),\ A_{36} = -\lambda asK_0(as),$$

$$A_{37} = 0,\ A_{38} = 0,$$

$$A_{41} = -I_0(as),\ A_{42} = as[I_0^2(as) - I_1^2(as)] - 4(1-\nu_1)I_0(as)I_1(as),$$

$$A_{43} = \lambda I_0(as),\ A_{44} = \lambda[4(1-\nu_2)I_0(as) + asI_1(as)], \qquad \text{(C.11)}$$

$$A_{45} = \lambda K_0(as),\ A_{46} = \lambda[-4(1-\nu_2)K_0(as) + asK_1(as)],$$

$$A_{47} = 0,\ A_{48} = 0,$$

$$A_{51} = 0,\ A_{52} = 0,$$

$$A_{53} = I_1(Rs),\ A_{54} = RsI_0(Rs),$$

$$A_{55} = -\lambda K_1(Rs),\ A_{56} = -RsK_0(Rs),$$

$$A_{57} = 2\mu_2 eK_1(Rs/s_1)/s_1,\ A_{58} = 2\mu_2 eK_1(Rs/s_2)/s_2,$$

$$A_{61} = 0,\ A_{62} = 0,$$

$$A_{63} = I_0(Rs),\ A_{64} = 4(1-\nu_2)I_0(Rs) + RsI_1(Rs),$$

$$A_{65} = K_0(Rs),\ A_{66} = -4(1-\nu_2)K_0(Rs) + RsK_1(Rs),$$

$$A_{67} = m_1 K_0(Rs/s_1),\ A_{68} = m_1 K_0(Rs/s_2),$$

$$A_{71} = 0,\ A_{72} = 0,$$

$$A_{73} = -I_0(Rs) + I_1(Rs)/Rs,\ A_{74} = (2\nu_2 - 1)I_0(Rs) - RsI_1(Rs),$$

$$A_{75} = -[K_0(Rs) + K_1(Rs)/Rs],\ A_{76} = (1-2\nu_2)K_0(Rs) - RsK_1(Rs),$$

$$A_{77} = (1/s_1^2 - a_c)K_0(Rs/s_1) + [(1-b_c)/(s_1 Rs)]K_1(Rs/s_1),$$

$$A_{78} = (1/s_2^2 - a_c)K_0(Rs/s_2) + [(1-b_c)/(s_2 Rs)]K_1(Rs/s_2),$$

$$A_{81} = 0,\ A_{82} = 0,$$

$$A_{83} = I_1(Rs),\ A_{84} = RsI_0(Rs) + 2(1-\nu_2)I_1(Rs),$$

$$A_{85} = -K_1(Rs),\ A_{86} = -RsK_0(Rs) + 2(1-\nu_2)K_1(Rs),$$

$$A_{87} = (1/s_1^3 - a_c/S_1)K_1(Rs/s_1),\ A_{88} = (1/s_2^3 - a_c/S_2)K_1(Rs/s_2),$$

here

$m_1 = 2\mu_2(a_{44} + g - a_{44}/s_1^2)$, and the definitions of the other parameters have been given in Chapter 3. The right hand side terms R_i (i = 1, ..., 8) can be expressed as

$$R_i(s) = \frac{1}{s^3}\int_a^R t\varphi_2(t)h_i dt, \qquad (i=1, 2, 5, ..., 7), \tag{C.12a}$$

$$R_3(s) = \frac{\lambda}{s^3}\int_a^R t\varphi_2(t)h_3(s,t)dt + \frac{1}{s^3}\int_0^{c_3}\varphi_3(t)\sin(st)dt \tag{C.12b}$$

$$R_4(s) = \frac{\lambda}{s^3}\int_a^R t\varphi_2(t)h_4(s,t)dt + \frac{1}{s^3}\int_0^{c_3}\varphi_4(t)\cos(st)dt \tag{C.12c}$$

$$R_8=0, \tag{C.12d}$$

where h_i (i=1,...,7) are given by

$$h_1 = [I_0(as) - I_1(as)/as]ts^2K_0(ts) + \{I_0(as) - [a^2s^2 + 2(1-\nu_2)]I_1(as)/as\}sK_1(ts), \tag{C.13a}$$

$$h_2 = -ts^2I_1(as)K_0(ts) + asI_0(as)sK_1(ts), \tag{C.13b}$$

$$h_3 = ts^2I_1(as)K_0(ts) + [-asI_0(as) + 2(1-\nu_2)I_1(as)]sK_1(ts), \tag{C.13c}$$

$$h_4 = ts^2I_0(as)K_0(ts) - [asI_1(as) + 2(1-\nu_2)I_0(as)]sK_1(ts), \tag{C.13d}$$

$$h_5(s) = -ts^2K_1(Rs)I_0(ts) + [RsK_0(Rs) + 2(1-\nu_2)K_1(Rs)]sI_1(ts), \tag{C.13e}$$

$$h_6(s) = [sK_0(Rs) - K_1(Rs)/R]tsI_0(ts)$$

$$+ \{K_0(Rs) + [Rs + 2(1-\nu_2)/Rs]K_1(Rs)\}sI_1(ts), \quad \text{(C.13f)}$$

$$h_7(s) = -ts^2K_1(Rs)I_0(ts) + RsK_0(Rs)sI_1(ts). \quad \text{(C.13g)}$$

The solution of the system (C.10) can be expressed as:

$$f_i(s) = \frac{1}{D(s)}\sum_{j=1}^{8} C_{ji}(s)R_j(s), \quad (i=1,..,8), \quad \text{(C.14)}$$

where $D(s)$ is the determinant of the coefficient matrix of system (C.10) and $C_{ji}(s)$ $(i, j = 1,...,8)$ are the elements of the adjoint of the matrix.

Now substituting (C.9a-b) and (C.14) for f_i $(i = 0,1,...,8)$ and g_0 in Eqs (A.3c, 3e) and (C.1d), and considering the stress boundary conditions along the cracks, one can obtain the system of singular integral equations, Eqs (3.23a-c). Introducing

$$F_{2j}(r,s) = C_{j3}(s)I_0(rs) + C_{j4}(s)[2(2-\nu_2)I_0(rs) + rsI_1(rs)]$$

$$+ C_{j5}(s)K_0(rs) + C_{j6}(s)[-2(2-\nu_2)K_0(rs) + rsK_1(rs)], \quad (j = 1,...,7), \quad \text{(C.15a)}$$

$$F_{3j}(s) = C_{j1}(s)(-I_0(as) + I_1(as)/as)$$

$$+ C_{j2}(s)[(2\nu_1 - 1)I_0(as) - asI_1(as)], \quad (j = 1, ..., 7), \quad \text{(C.15b)}$$

$$F_{4j}(s) = C_{j1}(s)I_1(as) + C_{j2}(s)[(asI_0(as) + 2(1-\nu_1)I_1(as)], \quad (j = 1, ..., 7), \quad \text{(C.15c)}$$

we have the following expressions for the kernels:

$$k_{22}(t,r) = t\int_0^{\infty}\left[\sum_{i=1}^{2,5,..7} F_{2i}(r,s)h_i(t,s) + \lambda(F_{23}(r,s)h_3(t,s) + F_{24}(r,s)h_4(t,s))\right]\frac{ds}{D(s)}$$

$$+\frac{1}{2}\begin{cases}\dfrac{E(r/t)}{t+r}+\dfrac{E(r/t)-1}{(t-r)}, & r<t\\[2ex] \dfrac{E(t/r)-1}{t-r}-\dfrac{E(t/r)}{t+r}+\dfrac{2K(t/r)}{r}, & t<r\end{cases}, \tag{C.16a}$$

$$k_{23}(t,r)=\int_0^{\infty}F_{23}(r,s)\sin(ts)/D(s)ds, \tag{C.16b}$$

$$k_{24}(t,r)=\int_0^{\infty}F_{24}(r,s)\cos(ts)/D(s)ds, \tag{C.16c}$$

$$k_{32}(t,z)=t\int_0^{\infty}\Big[\sum_{i=1}^{2,5,\ldots 7}F_{3i}(s)h_i(t,s)+\lambda(F_{33}(s)h_3(t,s)$$

$$+F_{34}(s)h_4(t,s))\Big]\cos(zs)/D(s)ds\,, \tag{C.17a}$$

$$k_{33}(t,z)=\int_0^{\infty}\left(F_{33}(s)/D(s)-\gamma_{11}\right)\sin(ts)\cos(zs)ds\,, \tag{C.17b}$$

$$k_{34}(t,z)=\int_0^{\infty}\left(F_{34}(s)/D(s)-\gamma_{12}\right)\cos(ts)\cos(zs)ds\,, \tag{C.17c}$$

$$k_{42}(t,z)=t\int_0^{\infty}\Big[\sum_{i=1}^{2,5,\ldots 7}F_{4i}(s)h_i(t,s)+\lambda(F_{43}(s)h_3(t,s)$$

$$+F_{44}(s)h_4(t,s))\Big]\sin(zs)/D(s)ds \tag{C.18a}$$

$$k_{43}(t,z)=\int_0^{\infty}\left(F_{43}(s)/D(s)+\gamma_{12}\right)\sin(ts)\sin(zs)ds\,, \tag{C.18b}$$

$$k_{44}(t,z) = \int_0^\infty (F_{44}(s)/D(s) + \gamma_{11})\cos(ts)\sin(zs)ds\,, \qquad \text{(C.18c)}$$

where the functions $E(\,)$ and $K(\,)$ are complete elliptic integrals of the first and second kind, respectively.

The kernels $k_{2j}(t, r)$ (j=2, 3, 4), $k_{ij}(t,z)$ (i=3, 4, j=2, 3, 4), are Fredholm kernels. Here because the two matrix crack tips are terminated at two interfaces and also the interfacial crack is connected to the matrix crack, $k_{22}(t, r)$ has strong singularities when both t and r approach the fiber/matrix interface or matrix/composite interface simultaneously. $K_{23}(t,r)$, $k_{24}(t, r)$, $k_{32}(t, z)$, and $k_{42}(t, z)$ all have strong singularities when their two arguments approach the intersection point of the matrix crack and the interfacial crack simultaneously. The detailed technique for handling such singularities has been presented in Appendix A.

Appendix D

Solution of the Three-Cylinder Problem with Multiple Matrix Cracks

D.1 Solution of the problem under the action of uniform strain alone

For the problem shown in Fig. 3.9(a), using the principle of superposition results in the following expressions:

$$k_1 = p_{21}\overline{k_1} - k_{12} = C_{m1}\varepsilon_0\overline{k_1} - k_{12}, \tag{D.1a}$$

$$k_2 = p_{21}\overline{k_2} - k_{22} = C_{m1}\varepsilon_0\overline{k_2} - k_{22}, \tag{D.1b}$$

$$\overline{\sigma_{f1}} = p_{21}\frac{V_m}{V_f} - \overline{\sigma_{f2}} = C_{m1}\varepsilon_0\frac{V_m}{V_f} - \overline{\sigma_{f2}}, \tag{D.1c}$$

$$u_{z1} = \overline{u_z}p_{21} = C_{m1}\varepsilon_0\overline{u_z}, \tag{D.1d}$$

where p_{21} is the pressure exerted on the matrix crack surfaces and is given by Eq (3.25b), k_1, k_2 are stress intensity factors of mode I and II, respectively, for the interfacial crack tip, $\overline{\sigma_{f1}}$ is the average fiber stress at the matrix crack section, u_{z1} is the magnitude of the axial displacement at two cross sections a distance L away from the matrix crack section for the problem shown in Fig 3.9 (b), k_{12}, k_{22} and $\overline{\sigma_{f1}}$ are the two stress intensity factors and the average fiber stress for the problem shown in Fig. 3.9 (c).

The problem depicted in Fig. 3.9 (c) can be solved using the principle of superposition again, as shown in Fig. D.1. Using Eqs (3.26a-b) the fiber stress and the matrix stress of the uncracked problem (Fig. D.1(b)) can be expressed as

$$\sigma_{f2} = C_{f2}\frac{u_{z2}}{L} = \frac{C_{f2}C_{m1}}{C_{m2}}\left(\frac{C_{m2}\overline{u_z}}{L}\right)\varepsilon_0, \tag{D.2a}$$

$$p_{22} = C_{m2}\frac{u_{z2}}{L} = C_{m1}\left(\frac{C_{m2}\overline{u_z}}{L}\right)\varepsilon_0. \tag{D.2b}$$

Following the same procedure as used for the derivation of Eqs (D.1a-d), one can get the similar expressions for the problem depicted in Fig D.1(c):

$$k_{12} = p_{22}\overline{k_1} - k_{13} = C_{m1}\left(\frac{C_{m2}\overline{u_z}}{L}\right)\varepsilon_0\overline{k_1} - k_{13}, \tag{D.3a}$$

$$k_{22} = p_{22}\overline{k_2} - k_{23} = C_{m1}\left(\frac{C_{m2}\overline{u_z}}{L}\right)\varepsilon_0\overline{k_2} - k_{23}, \tag{D.3b}$$

$$\overline{\sigma_{f2}} = p_{22}\frac{V_m}{V_f} - \overline{\sigma_{f3}} = C_{m1}\frac{V_m}{V_f}\left(\frac{C_{m2}\overline{u_z}}{L}\right)\varepsilon_0 - \overline{\sigma_{f3}}, \tag{D.3c}$$

$$u_{z2} = \overline{u_z}p_{22} = C_{m1}\left(\frac{C_{m2}\overline{u_z}}{L}\right)\varepsilon_0\overline{u_z}. \tag{D.3d}$$

Repeating the iteration process to step j, one has

$$\sigma_{fj} = C_{f2}\frac{u_{zj}}{L} = \frac{C_{f2}C_{m1}}{C_{m2}}\left(\frac{C_{m2}\overline{u_z}}{L}\right)^{j-1}\varepsilon_0, \tag{D.4a}$$

$$p_{2j} = C_{m2}\frac{u_{zj}}{L} = C_{m1}\left(\frac{C_{m2}\overline{u_z}}{L}\right)^{j-1}\varepsilon_0, \tag{D.4b}$$

$$k_{1j} = p_{2j}\overline{k_1} - k_{1j+1} = C_{m1}\left(\frac{C_{m2}\overline{u_z}}{L}\right)^{j-1}\varepsilon_0\overline{k_1} - k_{1j+1}, \tag{D.4c}$$

$$k_{2j} = p_{2j}\overline{k_2} - k_{2j+1} = C_{m1}\left(\frac{C_{m2}\overline{u_z}}{L}\right)^{j-1} \varepsilon_0 \overline{k_2} - k_{2j+1}\ , \tag{D.4d}$$

$$\overline{\sigma_{jj}} = p_{2j}\frac{V_m}{V_f} - \overline{\sigma_{jj+1}} = C_{m1}\frac{V_m}{V_f}\left(\frac{C_{m2}\overline{u_z}}{L}\right)^{j-1} \varepsilon_0 - \overline{\sigma_{jj+1}}\ , \tag{D.4e}$$

$$u_{zj} = \overline{u_z} p_{2j} = C_{m1}\left(\frac{C_{m2}\overline{u_z}}{L}\right)^{j-1} \varepsilon_0 \overline{u_z}\ . \tag{D.4f}$$

The solution of the problem shown in Fig. 3.9(a) can now be summed up as

$$k_1 = \varepsilon_0 C_{m1}\overline{k_1}(1 - r + r^2 - r^3 + \ldots), \tag{D.5a}$$

$$k_2 = \varepsilon_0 C_{m1}\overline{k_2}(1 - r + r^2 - r^3 + \ldots), \tag{D.5b}$$

$$\overline{\sigma_f} = \varepsilon_0\left[-\frac{C_{m1}C_{f2}}{C_{m2}} + \left(\frac{V_m C_{m1}}{V_f} + \frac{C_{m1}C_{f2}}{C_{m2}}\right)(1 - r + r^2 - r^3 + \ldots)\right], \tag{D.5c}$$

where $r = C_{m2}\overline{u_z} / L$.

D.2 Solution of the problem under the action of interfacial friction alone

If an interfacial frictional force exists, we can analyze its effects separately. For the configuration shown in Fig. 3.9 (a) loaded by an interfacial frictional stress τ_s alone, the solution can be expressed as the solution of the problem depicted in Fig. 3.9 (b) subtracted by that to the problem shown in Fig. 3.9 (c). Since the latter problem is loaded by uniform strain alone, the solution has actually been derived in section D.1. Consider the configuration shown in Fig. 3.9 (b) exerted on the interfacial crack surfaces by a unit shearing stress. Let us denote the stress intensity factors and the magnitude of the displacements at the two cross sections by $\overline{k_{1s}}$, $\overline{k_{2s}}$ and $\overline{u_{zs}}$, respectively. The stress

intensity factors and the average fiber stress for the crack configuration shown in Fig. 3.9 (a) can be expressed as

$$k_1 = \tau_s \left[\overline{k_{1s}} - \frac{\overline{u_{zs}} C_{m2} \overline{k_1}}{L} (1 - r + r^2 - r^3 + \ldots) \right], \tag{D.6a}$$

$$k_2 = \tau_s \left[\overline{k_{2s}} - \frac{\overline{u_{zs}} C_{m2} \overline{k_2}}{L} (1 - r + r^2 - r^3 + \ldots) \right], \tag{D.6b}$$

$$\overline{\sigma_f} = -\frac{\tau_s \overline{u_{zs}}}{L} \left(C_{f2} + \frac{V_m C_{m2}}{V_f} \right) (1 - r + r^2 - r^3 + \ldots). \tag{D.6c}$$

Under the action of both applied strain and the friction force, the response of the representative volume shown in Fig. 3.9 (a) can be obtained by combining each equation in Eqs (D.5a-c) with the related one in Eqs (D.6a-c).

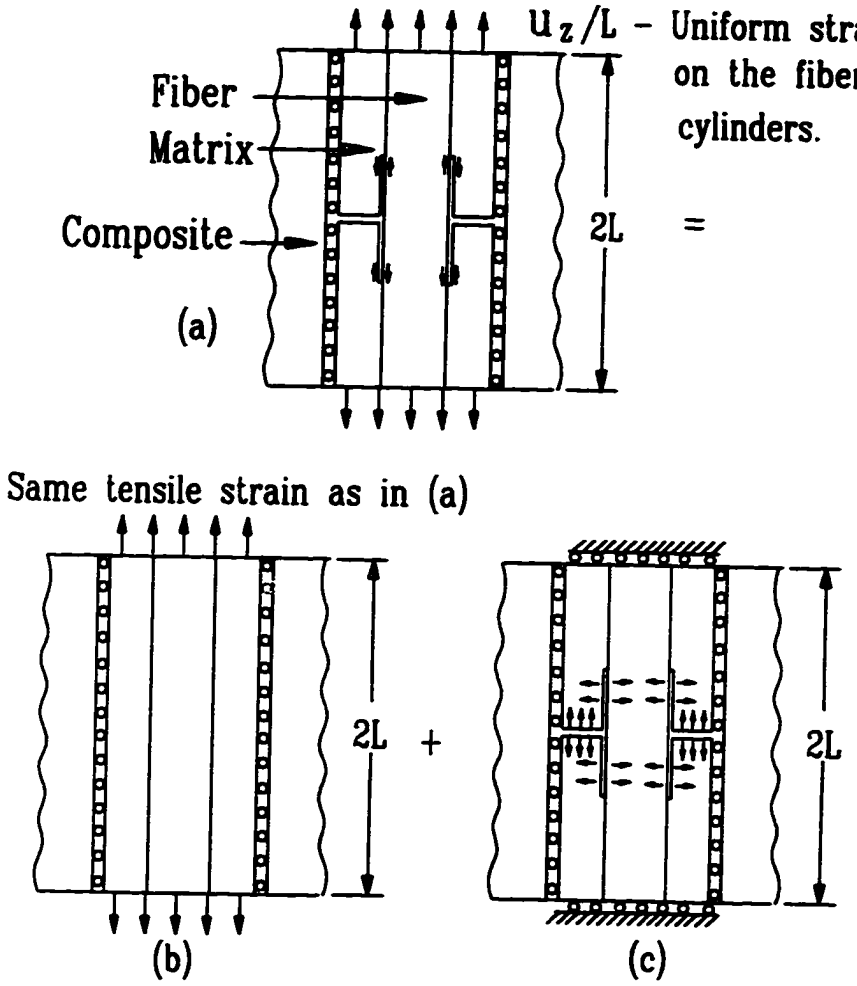

Fig. D.1 Schematic showing the procedure for solving the problems shown in Figs. 3.9 (c) and 3.10 (c).

Bibliography

[1] R. A. J. Sambell, A. Briggs, D. C. Phillips and D. H. Bowen, Carbon fiber composites with ceramic and glass matrices, Part 2 — Continuous fibers. *J. Mater. Sci.*, 7 [6] 676-81 (1972).

[2] D. C. Phillips, The fracture energy of carbon-fiber reinforced glass. *J. Mater. Sci.*, 7 [11] 1175-91 (1972).

[3] D. C. Phillips, Interfacial bonding and toughness of carbon fiber reinforced glass and glass-ceramics. *J. Mater. Sci.*, **9** [11] 1847-54 (1974).

[4] K. M. Prewo and J. J. Brennan, High strength silicon carbide fiber reinforced glass matrix composites, *J. Mater. Sci.*, **15** [2] 463-68 (1980).

[5] K. M. Prewo and J. J. Brennan, Silicon carbide yarn reinforced glass matrix composites, *J. Mater. Sci.*, **17** [4] 1201-1206 (1982).

[6] J. J. Brennan and K. M. Prewo, Silicon carbide fiber reinforced glass-ceramic matrix composites exhibiting high strength and toughness, *J. Mater. Sci.*, **17** [8] 2371-2383 (1982).

[7] T. Mah, M.G. Mendiratta, A. P. Katz, R. Ruh and K.S. Mazdiyasni, Room-temperature mechanical behavior of fiber-reinforced ceramic-matrix composites. *J. Am. Ceram. Soc.*, **68** [1] c-27-30 (1985).

[8] D. B. Marshall and A. G. Evans, Failure mechanisms in ceramic-fiber/ceramic-matrix composites. *J. Am. Ceram. Soc.*, **68** [5] 225-31 (1985).

[9] F. Delale, B. M. Liaw, S. J. Zhang and H. Q. Zhang, Tensile behavior of ceramic matrix composites at room and elevated temperatures, Ceramic matrix composites and other systems, ICCM/9. *Proceeding of the Ninth International Conference on Composite Materials,* A. Miravete, ed., Madrid, Spain, Vol. II, 55-62, 1993.

[10] S. Zhang, An investigation of tensile behavior of CMC's at room and elevated temperatures, Ph.D. Dissertation, The City University of New York, 1995.

[11] J. Aveston, G. A. Cooper and A. Kelly, Single and multiple fracture. *Proceedings of National Physical Laboratory.* Guilford: IPC Science and Technology Press, pp. 15-26 (1971).

[12] J. Aveston and A. Kelly, Theory of multiple fracture of fibrous composites. *J. Mater. Sci.* **8**, 352-362 (1973).

[13] B. Budiansky, J. W. Hutchinson and A. G. Evans, Matrix fracture in fiber-reinforced ceramics. *J. Mech. Phys. Solids* **34**, No. 2, 167-189 (1986).

[14] D. B. Marshall, B. N. Cox and A. G. Evans, The mechanics of matrix cracking in brittle-matrix fiber composites. *Acta Metall.* **33**, No. 11, 2013-2021 (1985).

[15] L. N. McCartney, Mechanics of matrix cracking in brittle-matrix fiber-reinforced composites. *Proc. R. Soc. Lond.* A **409**, 329-350 (1987).

[16] M. W. Barsoum, P. Kangutkar and A. S. D. Wang, Matrix crack initiation in ceramic matrix composites Part I: Experiments and test results. *Composites Science and Technology*, **44** 257-269 (1992).

[17] A. S. D. Wang, X. G. Huang and M. W. Barsoum, Matrix crack initiation in ceramic matrix composites Part II: Models and simulation results. *Composites Science and Technology*, **44** 271-282 (1992).

[18] W. S, Kou and T. W. Chou, Predictions of the critical strain for matrix cracking of ceramic matrix composites. In *Proceedings of IUTAM symposium: Inelastic Deformation of Composite Materials,* ed. G. J. Dvorak. Springer-Verlag, 639-50, 1990.

[19] Y. Weitsman and H. Zhu, Multi-fracture of ceramic composites. *J. Mech. Phsy. Solids* **41** (2), 351-388 (1993).

[20] W. S. Kou and T. W. Chou, Multiple cracking of unidirectional and cross-ply ceramic matrix composites. *J. Am. Ceram. Soc.* **78**[3], 745-55, 1995.

[21] J. W. Lee and I. M. Daniel, Deformation and failure of longitudinally loaded brittle-matrix composites. In *Proceedings of the Tenth Symposium on Composite Materials: Testing and Design,* ed. G. C. Grimes. ASTM, 204-21, 1992.

[22] J. P. Solti, S. Mall and D. D. Robertson, Modeling damage in unidirectional ceramic-matrix composites. *Composites Science and Technology,* **54**, 55-66, 1995.

[23] L. B. Greszczuk, Interface in composites. ASTM STP 452 (American Society for Testing and Materials, Philadelphia, 1969) p. 42.

[24] P. Lawrence, Some theoretical considerations of fiber pull-out from an elastic matrix. *J. Mater. Sci.*, **7**, 1-6 (1972).

[25] A. Takaku and R. G. C. Arridge, The effect of interfacial radial and shear stress on fiber pull-out in composite materials. *J. Phys. D: Appl. Phys.*, **6**, 2038-47 (1973).

[26] H. Stang and S. P. Shah, Failure of fiber-reinforced composites by pull-out fracture. *J. Mater. Sci.*, **21**, 935-957 (1986).

[27] J. K. Wells and P. W. R. Beaumont, Debonding and pull-out processes in fibrous composites. *J. Mater. Sci.*, **20**, 1275-1284 (1985).

[28] J. K. Wells and P. W. R. Beaumont, Crack-tip energy absorption processes in fiber composites. *J. Mater. Sci.*, **20**, 2735-2749 (1985).

[29] Y. C. Gao, Y. W. Mai and B. Cotterell, Fracture of fiber-reinforced materials. *J. Appl. Math. & phsy. (ZAMP)*, **39**, 550-572 (1988).

[30] J. W. Hutchinson and H. M. Jensen, Models of fiber debonding and pullout in brittle composites with friction. *Mech. Mater.* **9**, 139-163 (1990).

[31] P. G. Charalambides and A. G. Evans, Debonding properties of residually stressed brittle-matrix composites. *J. Am. Ceram. Soc.*, **72** [5] 746-53 (1989).

[32] L. N. McCartney, New theoretical model of stress transfer between fiber and matrix in a uniaxially fiber-reinforced composite. *Proc. R. Soc. Lond.* A **425**, 215-244 (1989).

[33] D. B. Marshall and W. C. Oliver, Measurement of interfacial mechanical properties in fiber-reinforced ceramic composites. *J. Am. Ceram. Soc.*, **70** [8] 542-48 (1987).

[34] D. K. Shetty, Shear-lag analysis of fiber push-out (indentation) tests for estimating interfacial friction stress in ceramic-matrix composites. *J. Am. Ceram. Soc.*, **71** [2] C107-C109 (1988).

[35] J. D. Bright, D. K. Shetty, C. W. Griffin and S. Y. Limaye, Interfacial bonding and friction in silicon carbide (filament)-reinforced ceramic- and glass-matrix composites. *J. Am. Ceram. Soc.*, **72** [10] 1891-98 (1989).

[36] D. B. Marshall, M. C. Shaw and W. L. Morris, Measurement of interfacial debonding and sliding resistance in fiber reinforced intermetallics. *Acta Metall. Mater.* **40** (3), 443-454 (1992).

[37] B. N. Cox, Interfacial sliding near a free surface in a fibrous or layered composite during thermal cycling. *Acta Metall. Mater.* **38** (12), 2411-2424 (1990).

[38] B. N. Cox, M. S. Dadkhah, M. R. James, D. B. Marshall, W. L. Morris and M. Shaw, On determining temperature dependent interfacial shear properties and bulk residual stresses in fibrous composites. *Acta Metall. Mater.* **38** (12), 2425-2433 (1990).

[39] D. B. Marshall, Analysis of fiber debonding and sliding experiments in brittle matrix composites. *Acta Metall. Mater.* **40** (3), 427-441 (1992).

[40] G. Y. Lu and Y. M. Mai, a theoretical model for the evaluation of interfacial properties of fiber-reinforced ceramics with slice compression test. *Composite Science and Technology,* **51**, 565-574 (1994).

[41] B. Budiansky, A. G. Evans and J. W. Hutchinson, Fiber-matrix debonding effects on cracking in aligned fiber ceramic composites. *Int. J. Solids Structures,* **32** (3/4), 315-328 (1995).

[42] D. B. Marshall and B. N. Cox, Tensile fracture of brittle matrix composites: Influence of fiber strength. *Acta Metall.,* **35** (11), 2607-2619 (1987).

[43] B. Budiansky and Y. L. Cui, On the tensile strength of a fiber-reinforced ceramic composite containing a crack-like flaw. *J. Mech. Phys. Solids,* **42** (1), 1-19 (1994).

[44] G. Bao and Z. Suo, Remarks on crack-bridging concepts. *Appl. Mech. Rev.,* **45** (8), 355-366 (1992).

[45] G. Bao and Y. Song, Crack bridging models for fiber composites with slip-dependent interfaces. *J. Mech. Phys. Solids,* **41** (9), 1425-1444 (1993).

[46] Z. C. Xia, J. W. Hutchison, A. G. Evans and B. Budiansky, On large scale sliding in fiber-reinforced composites. *J. Mech. Phsy. Solids,* **42** (7) 1139-1158 (1994).

[47] G. Meda and P. S. Steif, Adetailed analysis of cracks bridged by fibers-I. Limiting cases of short and long cracks. *J. Mech. Phsy. Solids,* **42** (8) 1293-1321 (1994).

[48] G. Meda and P. S. Steif, A detailed analysis of cracks bridged by fibers-II. Cracks of intermediate size. *J. Mech. Phsy. Solids,* **42** (8) 1323-1341 (1994).

[49] F. Erdogan and T. Ozbek, Stresses in fiber-reinforced composites with imperfect bonding. *J. Appl. Mech. Trans. ASME* 865-869, Dec. (1969).

[50] A. C. Wijeyewickrema, L. M. Keer, K. Hirashima and T. Mura, The annular crack surrounding an elastic fiber in a tension field. *Int. J. Solids Structures* **27**, No. 3, 315-328 (1991).

[51] A. C. Wijeyewickrema and L. M. Keer, Matrix fracture in brittle matrix fiber-reinforced composites. *Int. J. Solids Structures* **28**, No. 1, 43-65 (1991).

[52] A. C. Wijeyewickrema and L. M. Keer, Matrix crack interaction in a fiber-reinforced brittle matrix composite. *Int. J. Solids Structures* **29**, No. 5, 559-570 (1992).

[53] A. C. Wijeyewickrema and L. M. Keer, Matrix cracking in a fiber-reinforced composite with slip at the fiber-matrix interface. *Int. J. Solids Structures* **30**, No. 1, 91-113 (1993).

[54] A. K. Kaw and N. J. Pagano, Axisymmetric thermoelastic response of a composite cylinder containing an annular matrix crack. *J. Comp. Mater.* **27** No. 6, 540-571 (1993).

[55] H. Q. Zhang, F. Delale and B. M. Liaw, Interface and matrix fracture in brittle fiber-reinforced composites. *Engng Fracture Mech.* **55** 249-273, 1996.

[56] M. L. Williams, The stress around a fault or crack in dissimilar media. *Bulletin of the Seismological Society of America*, **49**, 199-204 (1959).

[57] F. Erdogan, Stress distribution in a nonhomogeneous elastic plane with cracks. *J. Appl. Mech.*, **30**, *TRANS. ASME*, **85**, 232-237 (1963).

[58] A. H. England, A crack between dissimilar media. *ASME J. Appl. Mech.*, **32**, 400-402 (1965).

[59] J. R. Rice, Elastic fracture mechanics concepts for interfacial cracks. *ASME J. Appl. Mech.*, **55**, 98-103 (1988).

[60] J. M. Hedgepeth, Stress concentrations in filamentary structures. *NASA TN* D-882, 1961, Langley Research Center.

[61] J. M. Hedgepeth, and P. Van Dyke, Local stress concentrations in imperfect filamentary composite materials. *J. Comp. Matls.* **1**, 294-309, 1967.

[62] E. D. Jr, Reedy, Analysis of center-notched monolayer with application to boron/aluminum composites. *J. Mech. Phys. Solids.* **28**, 265-286, 1980.

[63] Reedy, E. D., Jr, Fiber stresses in a cracked monolayer: comparison of shear-lag and 3-D finite element predictions. *J. Composite Materials.* **18**, 595-607, 1984.

[64] J. G. Goree and R. S. Gross, Stresses in three-dimensional unidirectional composite containing broken fibers. *Engng Fracture Mech.* **13** 395-405, 1980.

[65] J. N. Rossettos, and M. Shishesaz, Stress concentration in fiber composite sheets including matrix extension. *J. Appl. Mech.* **54**, 723-724, 1987.

[66] R. Muki and E. Sternberg, Load-absorption by a discontinuous filament in a fiber-reinforced composite. *Z. Angew. Math. Phys.* **22**, 809-824, 1971.

[67] E. F. Ford, Stress analysis of a broken fiber imbedded in an elastic medium. Technical Report No. 1, NSF Grant GH-33576, Division of Applied Sciences, Harvard University, 1973.

[68] A. Dollar and P. S. Steif, Load transfer in composites with Coulomb friction interface. *Int. J. Solids Structures* **24**, 789-803, 1988.

[69] H. R. Schwietert and P. S. Steif, Analysis of a broken fiber in a weakly bonded composite. *Int. J. Solids Structures* **28**, 283-297, 1991.

[70] B. Aksel, C. Y. Hui and D. C. Lagoudas, Effects of a frictional interface on the load diffusion from a broken filament embedded in an elastic medium. *Int. J. Solids Structures* **27**, 833-847, 1991.

[71] H. Q. Zhang, B. M. Liaw and F. Delale, Analysis of fiber break in a brittle composite. Submitted to *Composites Engineering* for publication.

[72] B. M. Malyshev and R. L. Salganik, The strength of adhesive joints using the theory of fracture. *Int. J. Fracture Mech.* **1**, 114-128 (1965).

[73] S. G. Lekhnitskii, *Theory of Elasticity of an Anisotropic Elastic Body*, Holden-Day, San Francisco (1963).

[74] Z. Hashin and B. W. Rosen, The Elastic moduli of fiber-reinforced materials. *J. Appl. Mech.* **31**, 233 (1964); Errata **32**, 219 (1965).

[75] B. W. Rosen, Thermomechanical properties of fibrous composites. *Proc. R. Soc. Lond. (A)* **319**, 79 (1970).

[76] B. W. Rosen, Stiffness of fiber composite materials. *Composites*, **4**, 16-25 (1973).

[77] *IMSL FORTRAN Subroutines for Mathematical Applications, Version 1.0.* IMSL, Math/Library.

[78] D. L. Clements and W. T. Ang, Stress intensity factors for the circular annulus crack. *Int. J. Engng Sci.* **26**, 325-329 (1988).

[79] A. P. S. Selvadurai and B. M. Singh, The annular crack problem for an isotropic elastic solid. *Quart. Appl. Math.* **38**, 233-243 (1985).

[80] H. F. Nied, Circumferencially cracked cylinders under extension or bending, Ph.D. Dissertation, Lehigh University (1981).

[81] E. Vagaggini, J. M. Domergue and A. G. Evans, Relationships between hysteresis measurements and the constituent properties of ceramic matrix composites: I, Theory. *J Am. Ceram. Soc.* **78** [10], 2709-20 (1995).

[82] E. Vagaggini, J. M. Domergue and A. G. Evans, Relationships between hysteresis measurements and the constituent properties of ceramic matrix composites: II, Experimental studies on unidirectional materials. *J Am. Ceram. Soc.* **78** [10], 2721-31 (1995).

[83] A. E. H. Love, *A Treatise on the Mathematical Theory of Elasticity*, Dover, New York (1944).

[84] R. W. Little, *Elasticity*, Prentice-Hall, Inc., Englewood Cliffs, New Jersey (1973).

[85] M. C. Lu and F. Erdogan, Stress intensity factors in two bonded elastic layers containing cracks perpendicular to and on the interface—I. Analysis. *Engng. Fracture Mech.* **18,** 491-506 (1983).

[86] M. C. Lu and F. Erdogan, Stress intensity factors in two bonded elastic layers containing cracks perpendicular to and on the interface—II. Solution and results. *Engng. Fracture Mech.* **18,** 507-528 (1983).

[87] F. Erdogan, G. D. Gupta and T. S. Cook, Numerical solution of singular integral equations, in *Mechanics of Fracture* 1: *Methods of Analysis and Solutions of Crack Problems* (Edited by G. C. Sih), 368-425, Noordhoff Leyden (1973).

[88] N. I. Muskhelishvili, *Singular Integral Equations*, Noordhoff, Groningen, Holland (1953).

[89] P. S. Theocaris and N. I. Ioakimidis, Numerical integration methods for the solution of singular integral equations. *Quart. Appl. Math.* **35,** 173-183 (1977).

[90] P. S. Theocaris and N. I. Ioakimidis, On the selection of collocation points for the numerical solution of singular integral equations with generalized kernels appearing in elasticity problems. *Computers & Structures* **11,** 289-295 (1979).

[91] P. S. Theocaris and N. I. Ioakimidis, Stress intensity factors at the tips of an antiplane shear crack terminating at a bimaterial interface. *Int. J. Fracture* **13,** 549-552 (1977).

[92] P. S. Theocaris and N. I. Ioakimidis, A method of numerical solution of Cauchy-type singular integral equations with generalized kernels and arbitrary complex singularities. *J. Computational Phys.* **30**, 309-323 (1979).

[93] P. S. Theocaris and N. I. Ioakimidis, The numerical evaluation of a class of generalized stress intensity factors by use of the Lobatto-Jacobi numerical integration rule. *Int. J. Fracture* **14**, No. 5, 469-484 (1978).

[94] M. M. Chawla and T. R. Ramakrishnan, Modified Gauss-Jacobi Quadrature formulas for the numerical evaluation of Cauchy type singular integrals. *BIT* **14**, 14-21 (1974).

[95] M. C. Lu, A composite of two bonded strips containing perpendicular cracks and an interface crack. Ph.D. Dissertation, Lehigh University (October 1978).